

UNIVERSITE LIBRE DE BRUXELLES
Microgravity Research Center
Service de Chimie Physique E.P.
Professor Jean-Claude Legros



FINAL REPORT :

**INVESTIGATION OF THE ENHANCEMENT OF HEAT TRANSFER
THROUGH LIQUID/GAS INTERFACES DUE TO THE
THERMOCAPILLARY CONVECTIVE INSTABILITY**

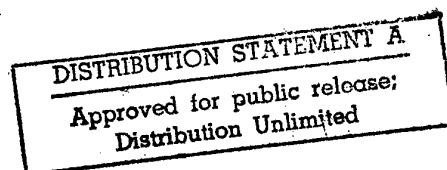
DTIC QUALITY INSPECTED 2

19980312 073

EUROPEAN OFFICE OF
AEROSPACE RESEARCH
AND DEVELOPMENT

PRINCIPAL INVESTIGATOR
Prof. Jean-Claude Legros
Dr Pierre Colinet

Special contract SPC-94-4031



REPORT DOCUMENTATION PAGE			Form Approved OMB No. 0704-0188	
Public reporting burden for this collection of information is estimated to average 1 hour per response, including the time for reviewing instructions, searching existing data sources, gathering and maintaining the data needed, and completing and reviewing the collection of information. Send comments regarding this burden estimate or any other aspect of this collection of information, including suggestions for reducing this burden to Washington Headquarters Services, Directorate for Information Operations and Reports, 1215 Jefferson Davis Highway, Suite 1204, Arlington, VA 22202-4302, and to the Office of Management and Budget, Paperwork Reduction Project (0704-0188), Washington, DC 20503.				
1. AGENCY USE ONLY (Leave blank)		2. REPORT DATE 1994		3. REPORT TYPE AND DATES COVERED Final Report
4. TITLE AND SUBTITLE Investigation of the Enhancement of Heat Transfer Through Liquid/Gas Interfaces Due to the Thermocapillary Convective Instability			5. FUNDING NUMBERS F6170894W0336	
6. AUTHOR(S) Prof. Jean Claude Legros				
7. PERFORMING ORGANIZATION NAME(S) AND ADDRESS(ES) Universite Libre de Bruxelles Head of MRC Av.F.D. Roosevelt 50 B-1050 Bruxelles CP165 Belgium			8. PERFORMING ORGANIZATION REPORT NUMBER N/A	
9. SPONSORING/MONITORING AGENCY NAME(S) AND ADDRESS(ES) EOARD PSC 802 BOX 14 FPO 09499-0200			10. SPONSORING/MONITORING AGENCY REPORT NUMBER SPC 94-4031	
11. SUPPLEMENTARY NOTES				
12a. DISTRIBUTION/AVAILABILITY STATEMENT Approved for public release; distribution is unlimited.			12b. DISTRIBUTION CODE A	
13. ABSTRACT (Maximum 200 words) This report results from a contract tasking Universite Libre de Bruxelles as follows: Investigate the enhancement of heat transfer in liquids due to thermocapillary convection.				
14. SUBJECT TERMS Nil			15. NUMBER OF PAGES 91	
			16. PRICE CODE N/A	
17. SECURITY CLASSIFICATION OF REPORT UNCLASSIFIED	18. SECURITY CLASSIFICATION OF THIS PAGE UNCLASSIFIED	19. SECURITY CLASSIFICATION OF ABSTRACT UNCLASSIFIED	20. LIMITATION OF ABSTRACT UL	

CONTENTS

I. GENERAL INTRODUCTION	3
II. STATEMENT OF THE PROBLEM - LINEAR STABILITY ANALYSIS	6
II.1. Rate of evaporation in the presence of surface deformation	6
II.2. Calculation of the rate of evaporation in the basic state	8
II.3. Stability of the reference solution versus hydrodynamic fluctuations	13
i) Model equations	14
ii) Dimensionless equations	16
II.4. Normal modes analysis	20
II.5. Importance of a nonlinear analysis	23
II.6. Conclusions of section II	28
II.7. References of section II	29
III. FINITE AMPLITUDE REGIMES OF THE SHORT-WAVE INSTABILITY	30
III.1. Introduction	30
III.2. Problem formulation - weakly nonlinear results	32
i) Derivation of amplitude equations	34
ii) Weakly nonlinear results	35
III.3. Numerical results and physical interpretation	37
III.4. Analysis of steady states	43
i) Bifurcation of rolls	43
ii) Competition between hexagons and rolls	44
iii) Asymptotic behaviours for $Ma \rightarrow \infty$	49
III.5. Conclusions of section III	52
Appendix 1 : Derivation of amplitude equations	53
Appendix 2 : Solution of the linear problem	54
Appendix 3 : Calculation of the mean temperature profile	56
III.6. References of section III	57
IV. NUMERICAL RESULTS	59
IV.1. Description of the method	59
IV.2. Finite-amplitude regimes of convection - behaviour at large Ma	60
IV.3. Comparison of numerical with analytical results	85
IV.4. Conclusions of section IV	88
IV.5. References of section IV	89
V. GENERAL CONCLUSIONS	90

I. GENERAL INTRODUCTION

The Marangoni phenomenon refers to the fluid motions induced in the vicinity of a surface of separation between two different fluids. At this surface, the thermodynamic properties (such as density, pressure, composition, ...) undergo rapid variations on a very small scale (the interfacial phase thickness). The experimentation on such interfaces in equilibrium configurations shows that the result of these rapid variations can be characterised by an internal energy per unit area, that is commonly referred to interfacial tension (for liquid/gas interfaces, the name surface tension is generally preferred). This allows to consider the fluid/fluid interfaces as discontinuities in the above-mentioned variables. Since the interfacial tension is in turn a function of intensive thermodynamic variables, interfacial tension variations along the surface can be present, provided that gradients of temperature/composition exist. These surface tension gradients (tangential stresses) may then create motions at the interface, that, due to viscosity, generally extend relatively far into the bulk of the adjacent liquids.

This phenomenon, also called thermocapillary convection (when the driving gradient is thermal), or solutocapillary convection (when it is compositional) may result in extremely different forms of convective motions, such as stationary motions, oscillations (waves), or even turbulent behaviours (interfacial turbulence). These different kinds of motions are generally divided into two broad classes, according to the direction of the gradients with respect to the interface.

The first case, called Marangoni convection, occurs when the gradients are parallel to interface. Since a stress is created along the interface, at that no counteracting force is present when the fluid is at rest, motions set in whatever the intensity of the gradient. A steady state is generally reached when the hydrodynamic pressure gradients created by fluid motions are able to balance the imposed surface tension stresses. An example of this phenomenon occurs when a cylindrical bridge of liquid is confined between two rigid disks maintained at different temperatures (this is the half-zone configuration often used in the studies of other more complicated techniques directed to the processing of crystals). A convective axisymmetric toroidal motion is generally observed (the motion is from hot to cold at the surface, provided that the surface tension is decreasing with temperature). For higher temperature gradient, other kinds of more complicated (non-axisymmetric) oscillating motions can be obtained, and are responsible for poor properties (surface state, composition homogeneity, ...) of crystals grown by these techniques. Other technological processes stimulating the need for an understanding of Marangoni motions occur in the drying technology (where Marangoni motions may at the contrary have a positive role), in the coating industry, in the laser processing of compact disks, in heat pipes technology, in boiling, ...

A second situation, called Marangoni-Bénard convection, occurs when the driving gradients are perpendicular, rather than parallel, to the interface. In this case, no tangential stress is created (because the interface is at constant temperature/ composition), and the mechanism responsible for convection is intimately associated with the presence of fluctuations (thermodynamic, or of external origin) of the intensive properties, coupled with the hydrodynamic effects (transport of heat, or of mass). For example, consider a fluid layer lying on a heated rigid plate, and open to air. When a small fluctuation of temperature (say

an increase) occurs at a point on the free surface (it may also originate in the liquid and diffuse to the surface), the surface tension is slightly lower at that point. This creates surface tension gradients along the surface, producing motions driving fluid away from the point. Continuity of the fluid then requires fluid coming from the bulk phase below the point, to the interface. Now, since a gradient of temperature is imposed by the heating, the fluid arriving at the surface is slightly hotter, and this lowers the surface tension again, thus amplifying the motions. This may also result in stationary convective structures, that create a tessellation of the layer in an almost periodic way (see fig. 1). An important difference exists between Marangoni convection and Marangoni-Bénard convection. For the former, motions exist whatever low is the value of the gradient imposed along the interface. At the contrary, for the latter, a critical value of the imposed gradient must be exceeded before motions occurs. This is associated with the presence of both thermal diffusivity and viscosity, the first of which damps the thermal fluctuations, and the second of which damps the fluid motions created by surface tension fluctuations. The competition between both these stabilising effects and the destabilising effect of surface tension variations is typically expressed through the dimensionless Marangoni number

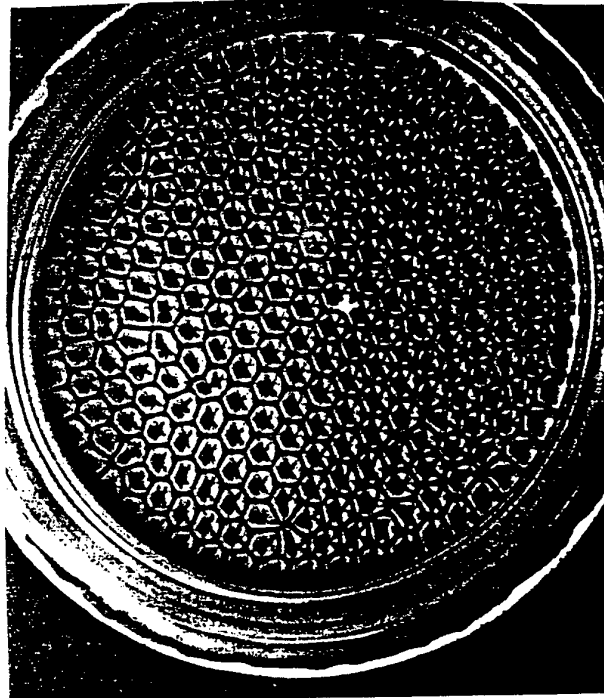


Figure 1.1: Hexagonal convective structure created by heating a thin liquid layer heated from below. The fluid moves upwards at the centre of an hexagon, and downwards at its peripheral.

$$Ma = \frac{-\sigma_T \Delta T h}{\mu \kappa} \quad (1.1)$$

where

σ_T	:	surface tension variation with temperature
h	:	thickness of the layer
μ	:	dynamic viscosity
κ	:	thermal diffusivity
ΔT	:	temperature difference between the rigid conducting plate and the free surface in the absence of convection ($\Delta T = \beta h$, where β is the imposed gradient).

A theoretical linear stability analysis, such as the one presented in this report, leads to the result that convective motions develop in the fluid provided that $Ma > Ma_c \approx 80$ (when the free surface Biot number is zero, meaning that the heat flux crossing it stays constant). The linear stability analysis also provides the horizontal length scale of the periodic structures

(size of the hexagonal cells at the threshold) as approximately equal to 3.14 h.

Thus, the fluid behaviour undergoes a drastic qualitative change when the Marangoni number exceeds the critical value, a phenomenon which is called a bifurcation, in the frame of nonlinear stability theories. The theoretical interest of the Marangoni-Bénard instability relies in the fact that it provides a relatively simple and well-controlled example of an hydrodynamic instability, that can be studied both theoretically and experimentally. Note that in some situations, it is very similar (on the point of view of theoretical techniques used near the instability threshold) to the more classical Rayleigh-Bénard convection (that occurs in the same experimental design, but when the destabilising effect is the density variation with temperature, i.e. the buoyancy force). However, important differences exist in other conditions (f.ex. when the imposed gradient is increased, and that secondary instabilities and transitions to more complex time-dependent situations occur), which justify the analysis of Marangoni-Bénard convection as an hydrodynamic instability capable of displaying phenomena such as pattern formation, defect generation (see the distorted hexagons, pentagon-heptagon pairs, ... of fig.1) and motion, wavelength adjustment mechanisms, effects of lateral walls (and other experimental imperfections), influence of symmetries, resonance effects, transient phenomena, secondary instabilities and transitions to turbulence.

An important practical feature of the Bénard instabilities is the drastic enhancement of heat transfer which is created by convection. This is generally measured by the Nusselt number, representing the dimensionless ratio of the total (convective and conductive) heat flux to the conductive heat flux : its value is thus always superior or equal to one, and is expected to increase with the distance to the threshold (generally measured by $\epsilon = (Ma - Ma_c)/Ma_c$). The dependency of the Nusselt number on the heating conditions (thus on ϵ) is not well-known for high values of the heat flux, and its knowledge is of fundamental importance in all domains where thermal energy has to be transported from one place to another through liquid phases. In this respect, it has been recognised that Marangoni convection might be a determinant factor in the amount of boiling heat transfer under reduced gravity conditions. The understanding of this heat transfer mechanism is also of tremendous importance to optimise evaporators which are used in large satellites, as capillary pumps (heat pipes) to transfer thermal energy from the place where it is dissipated (electronic boxes) towards radiators.

In some problems, the Nusselt number may have to be replaced by other quantities, which provide a better measure of the enhancement of heat transfer created by convection. The heat flux may for example be fixed as the external parameter, and we will be interested in calculating the cooling of the heat dissipating component by convection. This latter approach will be adopted in this report, as explained in section III, where a nonlinear analysis of the convection problem is presented, leading to estimates of the so-called bulk temperature decrease. Other results are obtained concerning the important problem of the selection of the wavelength of the steady convective structure at given Marangoni number. In section II, we begin by defining the important characteristics of the Marangoni-Bénard instability (the dimensionless parameters entering the problem), and investigate about the modelling of the effect of evaporation and surface deformation. Some classical results will also be recalled, and the limits of applications of our model will be determined. Finally, numerical simulations (Galerkin method) and comparison with analytical results of section III will be presented in section IV.

II. STATEMENT OF THE PROBLEM - LINEAR STABILITY ANALYSIS

II.1. Rate of evaporation in the presence of surface deformation

Consider a layer of a pure liquid, lying on a heated rigid plate ($z=0$) and in contact with its own vapour at a free interface whose shape is given by $z=h(x,t)$, in which x is the horizontal coordinate and t is time. At this interface, evaporation may occur, such that a mass flux $J = \vec{J} \cdot \vec{n}$ is allowed ($\vec{n} = (-h', 1)/N$ is the free surface normal pointing to the vapour, $N = (1 + h'^2)^{1/2}$ is the normalisation factor, and a prime denotes a derivative with respect to x). In many studies of evaporating liquid layers, the mass flux J is assumed to obey the well-known Hertz-Knudsen equation, derived from the kinetic theory of perfect gases. This is valid for a flat interface along which the equality of liquid and vapour temperatures is assumed, and reads

$$J = \beta \sqrt{\frac{M}{2\pi RT}} [p_s(T) - p_0(T)] \quad (2.1)$$

where β is the constant accommodation coefficient, M is the molecular weight of vapour, $p_s(T)$ is the saturation pressure at surface temperature T , $p_0(T)$ is the vapour pressure just beyond the interface, and R is the universal gas constant.

In this work, in order to start from a more general form of the nonequilibrium mass flux equation which should in particular be valid for a moving interface of arbitrary shape (and for any form of the vapour state equation), we suggest to use the macroscopic approach, as was proposed in [1]. First, note that the Clausius-Clapeyron equation can be derived from the equality condition $\mu_v(p_v, T_v) = \mu_l(p_l, T_l)$ between vapour and liquid chemical potentials. Developing this formula by the use of classical thermodynamics relations, the Clausius-Clapeyron equation gives the slope of the coexistence curve :

$$\frac{\partial p}{\partial T} = \frac{\rho_v \rho_l L}{(\rho_l - \rho_v) T} \quad (2.2)$$

obtained assuming thermal equilibrium $T_v = T_l (=T)$, and mechanical equilibrium $p_v = p_l (=p)$. In this relation, ρ_v and ρ_l are respectively the vapour and the liquid volumic masses, and L is the latent heat of evaporation. Since this mechanical equilibrium condition is not valid in general, the equality of chemical potentials does not hold anymore. The difference of chemical potentials is a generalised thermodynamic force giving rise to a nonequilibrium mass flux across the interface. This obviously suggests the use of the thermodynamics of irreversible processes [2], through the phenomenological law :

$$J = K[\mu_l(p_l, T) - \mu_v(p_v, T)] \quad (2.3)$$

where K is the positive phenomenological coefficient. Note that the hydrodynamic definition of the mass flux J is

$$J = \rho_l(\vec{v}_l - \vec{v}_z) \cdot \vec{n} = \rho_v(\vec{v}_v - \vec{v}_z) \cdot \vec{n} \quad (2.4)$$

where \vec{v}_v , \vec{v}_l and \vec{v}_z are respectively the vapour, liquid and interface velocities.

Note that if the temperature jump is not neglected, then other phenomenological coefficients appear, since there exist also a "thermal force" $\Delta T = T_l - T_v$. We discard this case in the

presented analysis.

Let $p_s(T)$ be a function defining the equilibrium (saturation) pressure at a given temperature T (for example the Clausius-Clapeyron coexistence curve, or any fitting of experimental points). Assume that the liquid and vapour state equations are respectively

$$\rho_l = \rho_l^0(p, T), \quad \rho_v = \rho_v^0(p, T)$$

and that the inequalities

$$\frac{|p_l - p_s(T)|}{p_s(T)} \ll 1, \quad \frac{|p_v - p_s(T)|}{p_s(T)} \ll 1$$

are valid everywhere along the liquid-vapour interface. Then, using Taylor expansion around the point $(p_s(T), T)$, at which chemical potentials are equal (by definition of $p_s(T)$), we get a linearised form of eq. (3) as

$$J = K(T) \left[\frac{p_s(T) - p_v}{\rho_v(T)} - \frac{p_s(T) - p_l}{\rho_l(T)} \right] \quad (2.5)$$

where $\rho_v(T)$, $\rho_l(T)$ and $K(T)$ stand for $\rho_v^0(p_s(T), T)$, $\rho_l^0(p_s(T), T)$ and $K(p_s(T), T)$ respectively.

Note that if $p_v \sim p_l$ in eq. (5), we get a form $J = K(p_s(T) - p_v)/\rho_v(T)$, presenting a formal analogy with the Hertz-Knudsen equation (although obtained independently), and leading to a rough estimate of the phenomenological coefficient $K = \beta \rho_v(T) (M/2\pi RT)^{1/2}$. Of course, only experimental measurements of K can lead to satisfactory values.

However, the approximation $p_v \sim p_l$ is only valid for weakly curved interfaces, and when dynamical effects can be neglected in the momentum balance at the interface. A more general form of equation (5) can be obtained by considering the Laplace pressure difference $p_v - p_l = \sigma H$ (H is the mean curvature of the interface) in eq. (5), thus leading to the equation

$$J = \frac{\rho_l(T) - \rho_v(T)}{\rho_l(T)\rho_v(T)} K(T) \left[p_s(T) - p_v - \sigma \frac{\rho_v(T)}{\rho_l(T) - \rho_v(T)} H \right] \quad (2.6)$$

incorporating the effect of surface tension on the rate of phase change.

Note that eq. (6) is only valid provided $|p_v - p_s(T)| \ll |\sigma H| \ll p_s(T)$. In pure weightlessness, every isothermal liquid-vapour system with an interface of constant curvature $H = H_0$ is in a state of mechanical equilibrium. Since no mass flux occurs across the interface, eq. 6 converts into

$$p_v = p_s(\theta) - \sigma \frac{\rho_v(\theta)}{\rho_l(\theta) - \rho_v(\theta)} H_0$$

where θ is the constant temperature of the isothermal system. this equation defines a connection between the saturation vapour pressure $p_s(\theta)$ at a plane phase interface and the vapour pressure p_v at an equilibrium interface of curvature H_0 . In the case of spherical interfaces, this is known as the Thomson equation.

II.2. Calculation of the rate of evaporation in the basic state

In this section, we compute the rate of evaporation of a liquid layer of depth h lying on a heated rigid plate maintained at a constant temperature T_b . The system is assumed as unidimensional (all the variables only depend on the vertical coordinate z , and the only non-zero component of the velocity in both liquid and gas phases is the vertical one, that will be noted w). The vapour phase is infinitely deep. The solution of the hydrodynamic equations that will be obtained will be called the basic solution (or the reference solution), and its stability against hydrodynamic two-dimensional fluctuations will be studied in section II.3 (Marangoni problem).

In the presence of evaporation, the relation (4) indicates that if the liquid is at rest ($w_l=0$), the interface moves with a vertical velocity $w_e = -J/\rho_l$. The second relation (4) then indicates that the vertical velocity of the vapour is $w_v = J (1/\rho_v - 1/\rho_l) \approx J/\rho_v$. This means that the liquid depth will decrease, and that it may finally completely evaporate. In order to obtain a steady reference solution (and a steady mass flux J), we will assume in the following that fresh liquid is injected at the bottom plate $z=0$, at a rate that exactly matches the rate of liquid which is evaporated at the free surface $z=h$. This is attempted in order to mimic the steady regime solution which is obtained in heat exchanging devices such as heat pipes, where liquid condensed at the condensor is continuously brought back to the evaporator, such that a steady regime may be obtained. The rigid bottom boundary may thus be considered as a porous material, through which a velocity $w_b = J/\rho_l$ is injected. Now, the whole liquid layer thus possesses the velocity $w_l = w_b = J/\rho_l$ (because the fluid is incompressible, such that $dw/dz=0$), and the relation (4) indicates that $w_e=0$. The interface is thus fixed in space at the location $z=h$.

The effective rate of evaporation J is given by the relation (5), which is seen to depend on the vapour and liquid pressures p_v and p_l on each side of the interface, and on the interfacial temperature T . Their value may only be obtained by solving the hydrodynamic equations in both liquid and gas phases, with suitable boundary conditions.

In both phases (indices v and l are omitted for simplicity), the full Navier-Stokes (conservation of momentum) equations for Newtonian fluids read

$$\rho \left(\frac{\partial \bar{v}}{\partial t} + (\bar{v} \cdot \bar{\nabla}) \bar{v} \right) = \mu \Delta \bar{v} - \bar{\nabla} p + \rho \bar{g} \quad (2.7)$$

where μ is the dynamic viscosity (assumed to be independent of temperature), and $\bar{g} = -g \bar{1}_z$ is the gravity vector ($\bar{1}_z$ is the unit vector along the vertical z -direction). As the system is unidimensional and the velocities are independent of z and t (steady problem) in both phases (the gas is also assumed to be incompressible, which is realistic for the range of velocities involved), the equations (7) reduce to an equation for the hydrodynamic pressure

$$\frac{dp}{dz} = -\rho g \quad (2.8)$$

Now, we have to consider the equation governing the temperature distribution in both phases. The energy equation reads

$$\rho C_p \left(\frac{\partial T}{\partial t} + (\vec{v} \cdot \vec{\nabla}) T \right) = \lambda \Delta T \quad (2.9)$$

where C_p is the specific heat at constant pressure, and λ is the thermal conductivity, both assumed to be constant in the range of temperatures involved. For unidimensional steady transport, the equation (9) reduces to

$$w \frac{dT}{dz} = \kappa \frac{d^2 T}{dz^2} \quad (2.10)$$

where $\kappa = \lambda / \rho C_p$ is the fluid thermal diffusivity.

Equations (8) and (10) may be directly integrated, to give the distribution of pressure and of temperature in both phases. We obtain

$$p_v = -\rho_v g z + c_1 \quad (2.11)$$

$$p_l = -\rho_l g z + c_2 \quad (2.12)$$

$$T_v = c_3 \exp[w_v z / \kappa_v] + c_4 \quad (2.13)$$

$$T_l = c_5 \exp[w_l z / \kappa_l] + c_6 \quad (2.14)$$

as a function of the 6 integration constants c_i to be determined from boundary conditions.

First of all, for $z \rightarrow \infty$ the temperature in the vapour phase must not diverge, which implies $c_3 = 0$. Thus the temperature is constant in the gas ($T_v = c_4 = T_i$ i.e. the temperature at the interface), and all the thermal energy is propagated by the convective transport of the latent heat with velocity w_v . Furthermore, we will neglect the barometric pressure variation in the gas phase (this is consistent with the assumption of incompressibility of the gas, and is justified because ρ_l is small). Thus $p_v = c_1 = p_g$, and the pressure is constant in the gas phase.

The boundary condition at the rigid conducting plate ($z=0$) is $T = T_b$, implying $c_5 + c_6 = T_b$. At the interface $z=h$, there is no temperature jump, such that $T_l(z=h) = c_5 \exp[w_l h / \kappa_l] + c_6 = T_i$. From these two relations, we obtain

$$c_5 = \frac{T_i - T_b}{\exp[w_l h / \kappa_l] - 1} \quad , \quad c_6 = T_b - c_5 \quad (2.15)$$

The constant c_2 may be obtained by considering the interfacial balance of normal momentum (see f.ex. [3]), which reads

$$p_v - p_l + J^2/\rho_v = 0 \quad (2.16)$$

where the last term accounts for the vapour recoil effect, i.e. the fact that there is a difference of velocity (and of normal momentum) between molecules of liquid arriving at the interface, and molecules of vapour leaving it. The general form of this momentum balance will be given in the section II.3.

The relation (16) thus gives $c_2 = p_g + J^2/\rho_v + \rho_l g h$.

Assuming that the gas pressure is given (as it is the case in variable conductance heat pipes), we are thus left with two unknowns T_i (the interfacial temperature) and J (the mass flux). Note that the fluid velocity w_l appearing in eq. 15 is linked to the mass flux J by the relation $w_l = J/\rho_l$.

The conservation of energy at the interface, the full form of which is given in the next section, expresses that the jump of normal heat fluxes is equal to the heat used for evaporation (latent heat L), plus the heat transformed into kinetic energy of the leaving vapour molecules [3] (note that the comparatively small kinetic energy of arriving liquid molecules is neglected) :

$$\lambda_v \frac{dT_v}{dz} - \lambda_l \frac{dT_l}{dz} = J(L + \frac{1}{2} w_v^2) = J(L + \frac{1}{2} (\frac{J}{\rho_v})^2) \quad (2.17)$$

This relation allows to compute the interfacial temperature T_i as a function of the mass flux, by the use of eqs (13) to (15) with $c_3=0$. We obtain

$$T_i = T_b - \frac{L + \frac{1}{2} (\frac{J}{\rho_v})^2}{C_{pl}} (1 - \exp[-w_l h / \kappa_l]) \quad (2.18)$$

The last boundary condition, providing a second relation between the mass flux and the interfacial temperature, is the phenomenological relation (5). With the help of eq. (16), this may be rewritten

$$J = \frac{K}{\rho_v} \left[p_s(T_i) - p_g + \frac{J^2}{\rho_l} \right] \quad (2.19)$$

where $1/\rho_l$ has been neglected with respect to $1/\rho_v$.

Relations (18) and (19) allow us in principle to compute T_i and J , provided we know the function $p_s(T)$, i.e. the relation between the equilibrium pressure and the interfacial temperature. We may for example use the Clausius-Clapeyron relation [4]

$$p_s(T) = p_0 \exp\left[-\frac{L}{R}\left(\frac{1}{T} - \frac{1}{T_0}\right)\right] \quad (2.20)$$

where (p_0, T_0) is a couple of values lying on the saturation curve (for example $T_0 = 100^\circ\text{C}$ and $p_0 = 1$ atm for pure water). For simplicity, we assume that the difference $T - T_0$ is small, and we use the linearised form of eq.(20)

$$p_s(T) \approx p_0 + p_T(T - T_0) \quad (2.21)$$

where $p_T = Lp_0/RT_0^2$ (≈ 0.036 atm/ $^\circ\text{K}$ for pure water).

We may now proceed to the resolution of the system of equations (18), (19) and (21). We first replace (18) in (21)

$$p_s(T_i) = p_b + p_T \frac{\left(L + \frac{1}{2}\left(\frac{J}{\rho_v}\right)^2\right)}{C_{pl}} \left(\exp\left[-\frac{Jh}{\rho_l \kappa_l}\right] - 1\right) \quad (2.22)$$

where p_b stands for $p_0 + p_T(T_b - T_0)$, i.e. the saturation pressure for the temperature of the bottom plate.

In the general case, the analytical resolution of equations (19) and (22) with respect to J and T_i appears to be impossible. In order to attempt a graphical resolution, we first solve (19) with respect to $p_s(T_i)$:

$$p_s(T_i) = p_g + \frac{\rho_v J}{K} - \frac{J^2}{\rho_l} \quad (2.23)$$

and both values of $p_s(T_i)$, given by eqs (22) and (23), are represented as a function of J in the same diagram (fig.2). The solution for J is at the intersection of both curves.

Now, we may obtain an analytical result for J , provided that its value is not too large. First of all, order of magnitude estimates show that it is legitimate to neglect the term $(J/\rho_v)^2$ with respect to L in eq. (22). This amounts to neglect the amount of kinetic energy imparted to the molecules of gas leaving the interface, compared to the energy used for evaporation. Another simplification is to neglect the effect of vapour recoil, i.e. J^2/ρ_l compared to other terms in (23). This is valid for the range of values of J considered in this analysis.

A more restrictive approximation concerns the exponential term in eq. (22). This term may be linearised provided that

$$Pe = \frac{Jh}{\rho_l \kappa_l} = \frac{w_l h}{\kappa_l} \ll 1 \quad (2.24)$$

where Pe is the thermal Peclet number, representing the ratio of the velocity of the fluid (associated with the rate of phase change) to the characteristic thermal velocity. It may also be defined as the ratio of the thermal relaxation time h^2/κ_l to the convective time h/w_l . Thus, its value will be small provided that the rate of phase change is not too high. More precisely, for a water layer of depth $h=1$ mm, this approximation is valid if J is at most of the order 10^{-3} g/cm²s, representing a heat transport of $J.L=2.3$ W/cm².

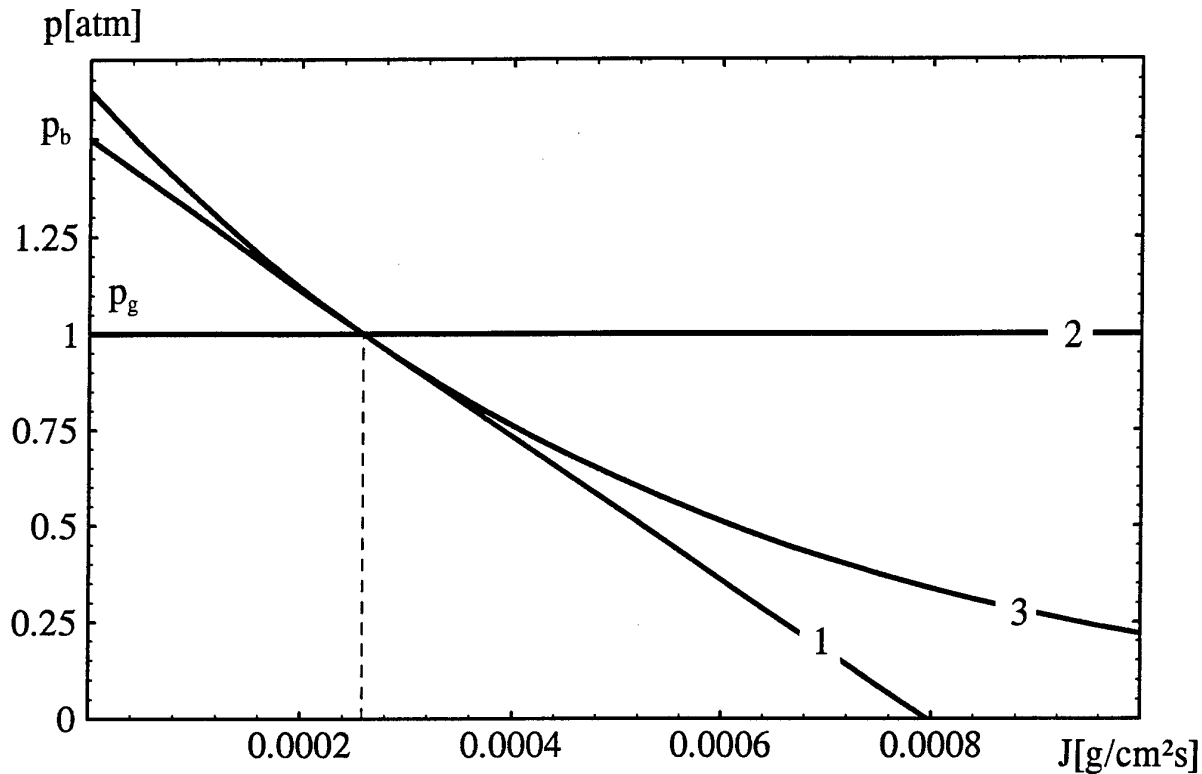


Figure 2.2: Graphical determination of J . $p_g=1$ atm is the vapour pressure, $p_b=1.5$ atm is the saturation pressure at the rigid plate temperature $T_b=487$ K (eq. 21). Curves 1 and 2 are given by equations (22) and (23), curve 3 is the Clausius-Clapeyron curve (eq.20) in which the temperature of the interface is evaluated by eq. 18. All the parameters are those of water ($T_0=473$ K, $p_0=1$ atm), with a depth $h=1$ mm, and an accommodation coefficient $\beta=0.1$. The supersaturation is $T_b-T_0=14^\circ$. It is found that $J \approx 2.6 \cdot 10^{-4}$ g/cm²s ($J.L \approx 0.6$ W/cm²).

With these approximations, eq. (22) may be written

$$p_s(T_i) \approx p_b + \frac{p_T L}{C_{pl}} \left(-\frac{Jh}{\rho_l \kappa_l} \right) = p_b - \frac{p_T L J h}{\lambda_l} \quad (2.25)$$

and eq. (23) reads

$$p_s(T_i) = p_g + \frac{\rho_v J}{K} \quad (2.26)$$

Equalisation of these two relations leads to the mass flux

$$J = \frac{p_b - p_g}{\frac{\rho_v}{K} + \frac{p_T L h}{\lambda_l}} \quad (2.27)$$

This relation involves only measurable quantities, at the exception of the phenomenological coefficient K . However, as mentioned earlier, K can be roughly estimated by the formula $K = \beta \rho_v(T) (M/2\pi RT)^{1/2}$. For water, this gives $K \approx 6 \cdot 10^{-10}$ gs/cm⁴ (with a value 0.1 of the accommodation coefficient β). Then, since $p_T L h / \lambda_l \approx 8 \cdot 10^8$ cm/s $\gg \rho_v / K \approx 10^6$ cm/s, the first term in the denominator of (27) is negligible compared to the second one (quasi-equilibrium case), and we get the relation

$$J = \frac{\lambda_l (p_b - p_g)}{p_T L h} \quad (2.28)$$

However, in the following, we will adopt the expression (27) of the reference mass flux J , in part because the actual values of K could be quite different from those estimated with the help of the Hertz-Knudsen relation. Moreover, the value of the accommodation coefficient β is generally found to be significantly reduced by the presence of impurities on the interface, such that it could not be legitimate to neglect non-equilibrium effects (finite K).

We now turn to a stability analysis of the reference state investigated in this section.

II.3. Stability of the reference solution versus hydrodynamic fluctuations

We now have to return to a more general formulation of the problem, which in particular allows for two-dimensional fluctuations of velocities, of pressure and of temperature, and involves surface tension effects. As explained in the introduction, surface tension gradients (caused by gradients of temperature) might be able to destabilise the above-calculated solution, provided that the temperature gradient perpendicular to the interface (created by evaporation) exceeds a critical value.

In this section, we define the linear stability problem to be studied. The system of equations and boundary conditions will be written under a dimensionless form, and a particular model of the problem will be introduced. This is known in the literature as the one-sided model [3], for which the dynamics of the gas phase can be decoupled from the dynamics in the liquid phase. We may thus solve the problem (with suitable boundary conditions) in the liquid phase only. This model requires the assumption that the ratios of volumic masses ρ_v / ρ_l , of thermal conductivities λ_v / λ_l and of dynamic viscosities μ_v / μ_l are small compared to unity, which is verified for most liquids in contact with their vapour, far enough from the critical point. It will be demonstrated that the effect of evaporation can be modeled (in a first approximation)

by introducing a free surface dimensionless Biot number Bi (for which a value is derived in this section).

In section II.4, the linear stability problem is solved, and thresholds for the Marangoni-Bénard instability are provided. The obtained solutions are valid as long as the amplitudes of perturbations around the reference solution are small. In section III, the full nonlinear Marangoni-Bénard problem will be investigated (finite-amplitude solutions) for short waves (perturbations located near the interface), after having simplified the problem by considering the case of an infinite Prandtl number fluid (which leads to results applicable to the case of normal liquids, including water for which $Pr=7$).

i) Model equations

The method used to study the stability of the reference solution (computed in the previous section) is general, and proceeds from the definition of stability, i.e. the resistance of the basic solution to infinitesimal hydrodynamic fluctuations. The equations governing the evolution of infinitesimal perturbations \vec{v}' , p' and T' of velocity, pressure and temperature around their reference state values \vec{v}_{ref} , p_{ref} and T_{ref} are obtained by inserting $\vec{v} = \vec{v}_{ref} + \vec{v}'$, $p = p_{ref} + p'$ and $T = T_{ref} + T'$ in the incompressibility relation $\vec{\nabla} \cdot \vec{v} = 0$ and in eqs (7) and (9), and by remarking that the reference solution satisfies these equations. We then obtain

$$\vec{\nabla} \cdot \vec{v} = 0 \quad (2.29)$$

$$\rho \frac{\partial w}{\partial t} + \rho w_{ref} D w = \mu \Delta w - D p \quad (2.30)$$

$$\rho \frac{\partial u}{\partial t} + \rho w_{ref} D u = \mu \Delta u - \frac{\partial p}{\partial x} \quad (2.31)$$

$$\frac{\partial T}{\partial t} + w_{ref} D T + w D T_{ref} = \kappa \Delta T \quad (2.32)$$

where the primes have been omitted for simplicity, all second-order terms involving products of perturbations have been neglected, both components of the Navier-Stokes equation (7) have been separated ($\vec{v} = u \vec{1}_x + w \vec{1}_z$), D denotes the z -derivative, and $\kappa = \lambda / \rho C_p$ is the thermal diffusivity. Note that in the following, subscripts v and l will be omitted when referring to a liquid quantity.

On the rigid conducting bottom plate $z=0$, The boundary conditions for the perturbations are

$$u = w = T = 0$$

because the total temperature is maintained constant at T_b (no perturbation) and the total velocity is kept at its reference value $\vec{V} = w_{ref} \vec{1}_z = \vec{1}_z J_{ref} / \rho_l$ (J_{ref} is the reference value of the

mass flux, given by eq. 27).

At the interface $z=h+\xi(x,t)$, the linearisation of the mass conservation relation (4) leads to

$$J = J_{ref} + J' = \rho_l w_{ref} + \rho_l (w_l(z=h) - w_\Sigma)$$

As $J_{ref} = \rho_l w_{ref}$, the perturbed mass flux J' is given by

$$J' = \rho_l (w_l(z=h) - w_\Sigma) \quad (2.33a)$$

and will be denoted by J in the following. Note that an equivalent treatment of the second equality in (4) gives

$$J' = \rho_v (w_v(z=h) - w_\Sigma) \quad (2.33b)$$

The general form of the momentum balance at the interface reads [1]

$$[[\rho((\vec{v} - \vec{v}_\Sigma) \cdot \vec{n}) \vec{v} + p \vec{n} + \vec{\tau} \cdot \vec{n}]] = \frac{\sigma \partial \vec{t} / \partial x + \vec{t} \partial \sigma / \partial x}{N} \quad (2.34)$$

where $[[x]]$ stands for the discontinuity $x_v - x_l$ (v and l denote respectively the vapour and the liquid), $\vec{n} = (-\xi' \vec{1}_x + \vec{1}_z)/N$ and $\vec{t} = (\vec{1}_x + \xi' \vec{1}_z)/N$ are respectively the free surface normal and tangential unit vectors ($N = (1 + \xi'^2)^{1/2}$ is the normalisation factor), σ is the surface tension, $\vec{\tau}$ is the viscous stress tensor with components $\tau_{ij} = -\mu(\partial v_i / \partial x_j + \partial v_j / \partial x_i)$.

Applying the one-sided model approximation ($\rho_v / \rho_l \rightarrow 0$, $\mu_v / \mu_l \rightarrow 0$), substituting $p \rightarrow p_{ref} + p$, $w \rightarrow w_{ref} + w$, and linearising, the projection of (34) on the surface normal reads

$$(p_v)_{ref} - (p_l)_{ref} + p_v - p_l = (\vec{\tau}_l \cdot \vec{n}) \cdot \vec{n} - \frac{J_{ref}^2}{\rho_v} - 2 \frac{J_{ref} J}{\rho_v} + \sigma \frac{\partial^2 \xi}{\partial x^2} \quad (2.35)$$

where the relation (33) has been used. This relation must be expressed at $z=h+\xi(x,t)$. Since $\xi(x,t) \ll 1$, the Taylor series around $z=h$ can be limited to linear terms in ξ . Using (16) at $z=h$, we obtain

$$p_v - p_l = -\rho_l g \xi - 2\mu_l D w_l - 2 \frac{J_{ref} J}{\rho_v} + \sigma \frac{\partial^2 \xi}{\partial x^2} \quad (2.36)$$

We must also project the relation (34) on the surface unit tangent \vec{t} . This gives, after linearisation,

$$\mu_l \left(\frac{\partial u_l}{\partial z} + \frac{\partial w_l}{\partial x} \right) = \sigma_T \frac{\partial T}{\partial x} \quad (2.37)$$

where σ_T is the surface tension variation with temperature. We may use the continuity

relation (29) to rewrite (37) under the form (expressed at $z=h$)

$$\mu_l \left(\frac{\partial^2 w}{\partial x^2} - \frac{\partial^2 w}{\partial z^2} \right) = \sigma_T \frac{\partial^2 T}{\partial x^2} \quad (2.38)$$

Note that in deriving eq. (37), we used the no-slip condition

$$\overline{v_l} \cdot \overline{t} = \overline{v_v} \cdot \overline{t} \quad (2.39)$$

whose perturbed and linearised form is

$$u_l = u_v + \frac{\partial \xi}{\partial x} \frac{J_{ref}}{\rho_v} \quad (2.40)$$

Now, perturbing eq. 15, and applying the one-sided model approximations, we get the perturbed mass flux as

$$J = K \left[\frac{p_T}{\rho_v} (T + \xi D T_{ref}) + \frac{p_l}{\rho_l} - \frac{p_v}{\rho_v} \right] \quad (2.41)$$

We may eliminate p_v between eqs (36) and (39), and get the following relation for J :

$$J = \frac{K}{1 - \frac{2KJ_{ref}}{\rho_v^2}} \left[\frac{p_T}{\rho_v} (T + \xi D T_{ref}) - \frac{p_l}{\rho_v} + \frac{\rho_l g}{\rho_v} \xi + 2 \frac{\mu_l}{\rho_v} D w_l - \frac{\sigma}{\rho_v} \frac{\partial^2 \xi}{\partial x^2} \right] \quad (2.42)$$

Having expressed the conservation of mass and of momentum at the interface, we still have to write the general conservation equation for the energy at the interface, which reads (in the one-sided model) as [3]

$$J \left(L + \frac{1}{2} \left(\frac{J}{\rho_v} \right)^2 \right) = -\lambda_l \overline{n} \cdot \overline{\nabla} T_l \quad (2.43)$$

The perturbed and linearised form is derived in the usual way. We obtain

$$-\lambda_l D T_l - \lambda_l \xi D^2 T_{ref} = J \left(L + \frac{3}{2} \left(\frac{J_{ref}}{\rho_v} \right)^2 \right) \quad (2.44)$$

ii) Dimensionless equations

The equations and boundary conditions can be put under dimensionless form by using h (the unperturbed liquid depth) as unit length, h^2/κ as unit time, κ/h as unit velocity, and $\mu\kappa/h^2$ as

unit pressure (fluid quantities without indices are those of the liquid phase). The temperature unit θ is based on the amplitude of the thermal gradient at the interface in the basic state (found from eq. 14,15,18 and 24) :

$$\theta = h |DT_{ref}(z=h)| = \frac{hJ_{ref}(L + \frac{1}{2}(\frac{J}{\rho_v})^2)}{\lambda_l}$$

The dimensionless equations valid in the liquid phase thus read (the same notations are kept for dimensionless velocity, temperature and pressure) :

$$\vec{\nabla} \cdot \vec{v} = 0 \quad (2.45)$$

$$Pr(\Delta w - Dp) = \frac{\partial w}{\partial t} + Pe Dw \quad (2.46)$$

$$Pr(\Delta u - \frac{\partial p}{\partial x}) = \frac{\partial u}{\partial t} + Pe Du \quad (2.47)$$

$$\Delta T + w \exp[Pe(z-1)] = \frac{\partial T}{\partial t} + Pe DT \quad (2.49)$$

where $Pr = \mu/\rho\kappa$ is the Prandtl number of the liquid, and the Peclet number $Pe = w_{ref}h/\kappa$ has been defined earlier (eq. 24).

The boundary conditions are :

- At the bottom plate ($z=0$) :

$$u = w = T = 0 \quad (2.50)$$

- At the interface ($z=1$) :

The mass conservation relation - definition of mass flux (eqs. 33a and 42) :

$$J = Pr^{-1}(w - w_{\Sigma}) = Pr^{-1}PeBi \left[(T - \xi) - \Pi_1(p - 2Dw) + \Pi_2\xi - \Pi_3\frac{\partial^2\xi}{\partial x^2} \right] \quad (2.51)$$

In this relation, the Biot number Bi has been defined by

$$Bi = \frac{p_T h L}{\rho_v \lambda_l} \frac{K}{1 - 2K \frac{J_{ref}}{\rho_v^2}} \quad (2.52)$$

where $(J_{ref}/\rho_v)^2$ has been neglected with respect to L in the expression of θ (as for eqs 25-28).

Other dimensionless groups appearing in eq. 51 are :

$$\Pi_1 = \frac{\mu_l \lambda_l \kappa_l}{J_{ref} h^3 p_T L}$$

$$\Pi_2 = \frac{\rho_l g \lambda_l}{J_{ref} p_T L}$$

$$\Pi_3 = \frac{\sigma \lambda_l}{J_{ref} h^2 p_T L}$$

Another boundary condition at $z=1$ is the normal momentum balance (eq. 36)

$$p_v - p_l + 2Dw_l = Cr^{-1} \frac{\partial^2 \xi}{\partial x^2} - Ga \xi - \frac{Pe}{\rho^* Pr} (w - w_\Sigma) \quad (2.53)$$

where we introduced the density ratio $\rho^* = \rho_v / \rho_l$, the Crispation number

$$Cr = \frac{\mu_l \kappa_l}{\sigma h}$$

which can be viewed as a measure of the free surface deformability, and the Galileo number

$$Ga = \frac{g h^3}{\nu_l \kappa_l}$$

characterising the influence of gravity on surface deformations.

We also have the tangential stress condition (eq. 38)

$$D^2 w - \frac{\partial^2 w}{\partial x^2} = Ma \frac{\partial^2 T}{\partial x^2} \quad (2.54)$$

where the Marangoni number, characterising the destabilising influence of the thermocapillary effect, is defined by

$$Ma = \frac{-\sigma_T \theta h}{\mu \kappa} = \frac{-\sigma_T \beta h^2}{\mu \kappa}$$

where $\beta = |DT_{ref}(z=h)|$ is the temperature gradient amplitude at the interface.

The no-slip condition (eq. 40) reads

$$u_i = u_v + \frac{Pe}{\rho^*} \frac{\partial \xi}{\partial x} \quad (2.55)$$

The thermal boundary condition is obtained from eq. 44, by remarking that $D^2 T_{ref} = -Pe\theta/h^2$. Using (42) and the definitions of Bi and Π_i , $i=1,2,3$, we get

$$DT - Pe\xi = Bi \left[-(T - \xi) + \Pi_1(p - 2Dw) - \Pi_2\xi + \Pi_3 \frac{\partial^2 \xi}{\partial x^2} \right] \quad (2.56)$$

and the last boundary condition is the kinematic condition, whose dimensionless linearised form reads

$$w_\xi = \frac{\partial \xi}{\partial t} \quad (2.57)$$

The system of equations and boundary conditions (45)-(57) is still not closed, since some quantities referring to the vapour phase still appear in boundary conditions (53) and (55). However, an important limiting case occurs when the Crispation number is very small (for a water layer of depth $h=1\text{mm}$, $Cr=1.4 \cdot 10^{-6}$), such that $\xi \rightarrow 0$ according to the boundary condition (53). It will be shown in the next section that this approximation is valid for perturbations with sufficiently small wavelengths, for which surface tension strongly damps surface deformations. Note that for large wavelengths, gravity is expected to play an equivalent stabilising role (the Galileo number $Ga \approx 10^5$ for 1mm water). Order of magnitude estimates also show that $\Pi_1 \approx 10^{-5}-10^{-4}$ for the range of mass fluxes considered, such that the pressure term may be neglected in eqs. 51 and 56, provided $|p-2Dw|/|T|$ is not larger than 10^{-3} (this will be verified a posteriori).

With these approximations, the system of equations (45) to (49) is unchanged, while the free surface boundary conditions 51-57 reduce to :

$$w = Pe Bi T \quad (2.58)$$

$$D^2 w - \frac{\partial^2 w}{\partial x^2} = Ma \frac{\partial^2 T}{\partial x^2} \quad (2.59)$$

$$DT + Bi T = 0 \quad (2.60)$$

and the system is closed in this limit, since no quantities linked to the gas phase appear in these boundary conditions.

It was also assumed in the last section (eq. 24) that the liquid Peclet number Pe is small compared to unity. In the limit $Pe \rightarrow 0$, the full problem just derived reduces to the problem

linearly treated by Pearson [5] (see next section). However, in Pearson's analysis, the value of the Biot number Bi is not related to evaporation parameters (because the heat transfer at the free surface is described by a classical Newton's cooling law, with a phenomenological coefficient whose estimation may be expected to depend on experimental peculiarities, such as the gas depth, thermal conductivity, gas convection, ...). In our analysis, the relation (52) will be used to evaluate the Biot number. In spite of the fact that this relation also contains a phenomenological coefficient K (defined by eq. 5), it can be expected that a satisfactory order of magnitude for K can be obtained from the kinetic theory of gases (for water with $h=1\text{mm}$, and an accommodation coefficient $\beta=0.1$, we find $Bi \approx 10^3$, but this value could be significantly reduced by impurities leading to much lower values of the accommodation coefficient $\beta=0.01$ or even $\beta=0.001$), and that this value will be less dependent on convection in the gas phase than it is for the Newton's heat transfer coefficient. Furthermore, the Biot number computed from eq. 52 will prove to be useful for investigating the influence of non-equilibrium effects (finite K).

II.4. Normal modes analysis

In the limit $Pe \rightarrow 0$, which can be considered as a good approximation for reasonable mass fluxes and small liquid depths, the system of eqs (45) to (49) reduces to

$$\nabla \cdot \vec{v} = 0 \quad (2.61)$$

$$\Delta w - Dp = Pr^{-1} \frac{\partial w}{\partial t} \quad (2.62)$$

$$\Delta u - \frac{\partial p}{\partial x} = Pr^{-1} \frac{\partial u}{\partial t} \quad (2.63)$$

$$\Delta T + w = \frac{\partial T}{\partial t} \quad (2.64)$$

with the boundary conditions $u=w=T=0$ at $z=0$. At the interface $z=h$, from eqs 58-60,

$$w = 0 \quad (2.65)$$

$$D^2 w = Ma \frac{\partial^2 T}{\partial x^2} \quad (2.66)$$

$$DT + BiT = 0 \quad (2.67)$$

This problem has been solved by Pearson [5] in the neutral stability case ($\partial/\partial t=0$), and the general resolution will now be presented.

It is possible to reduce the problem (61)-(67) to a problem for w and T only. This is done by deriving eq. 63 with respect to x , and adding the result to the z -derivative of eq. 62. Using eq. 61, we obtain $\Delta p=0$. Now, applying the Laplacian operator Δ to eq. 62, we

obtain a fourth order equation for w :

$$\Delta^2 w = Pr^{-1} \frac{\partial}{\partial t} \Delta w \quad (2.68)$$

Thus, we only need to solve eqs 68 with eq. 64, and apply the boundary conditions $w=Dw=T=0$ at $z=0$ (the condition $Dw=0$ comes from $u=0$ at $z=0$ and eq. 61), and interfacial conditions 65-67.

Separation of variables shows that the general solution of the linear problem is the superposition of Fourier modes that may be written

$$\begin{bmatrix} w_k(z,t) \\ T_k(z,t) \end{bmatrix} = \exp[\sigma_k t + i k x] \begin{bmatrix} w_k(z) \\ T_k(z) \end{bmatrix} \quad (2.69)$$

where the parameter k is the wavenumber of the disturbance (the wavelength is $2\pi/k$).

By introducing eq. 69 in the above problem, it is seen that each Fourier component (normal mode) must satisfy the eigenvalue problem

$$(D^2 - k^2)^2 w_k(z) = Pr^{-1} \sigma_k (D^2 - k^2) w_k(z) \quad (2.70)$$

$$(D^2 - k^2) T_k(z) + w_k(z) = \sigma_k T_k(z) \quad (2.71)$$

with boundary conditions

$$w_k(0) = Dw_k(0) = T_k(0) = 0 \quad (2.72)$$

$$w_k(1) = D^2 w_k(1) + k^2 Ma T_k(1) = DT_k(1) + Bi T_k(1) = 0 \quad (2.73)$$

It is possible (although calculations are not reproduced here for simplicity) to write the general solution of the ordinary differential equations 70-71, which depends on 6 constants to be determined from the boundary conditions 72-73. This provides a system of 6 homogeneous equations for the 6 unknown coefficients, which admits a non-trivial solution if and only if a compatibility condition (cancelation of the determinant of the matrix of the system) is satisfied. This characteristic relation may be written

$$\Delta(\sigma_k, k, Pr, Bi, Ma) = 0 \quad (2.74)$$

and allows to compute the growth constants σ_k for given k , Bi and Ma . Then, the reference state will be stable provided all growth constants σ_k have negative real part for all k . At the contrary, it will be unstable if there exist some values of k for which at least one eigenvalue σ_k has a positive real part (from eq. 69, it is seen that it will grow exponentially in time). In practice, we determine the threshold of the instability by substituting $\sigma_k \rightarrow 0$ (the possibility

of oscillatory onset $\sigma=i\omega$ can be rejected, as shown in [6]) in eq. 74. After simplifying the so-called neutral stability relation, we obtain

$$Ma = \frac{16k(k \cosh(k) + Bi \sinh(k))(\sinh(2k) - 2k)}{\sinh(3k) - 3 \sinh(k) - 4k^3 \cosh(k)} \quad (2.75)$$

which is the Pearson's result [5]. Note that this result does not depend on the Prandtl number Pr (when $\sigma_k=0$, the problem 70-73 does not depend on Pr anymore). This relation is represented on fig. 3 for several values of the Biot number Bi . For given Ma and Bi , it can be verified that the reference state (computed in section II.2) is stable against a disturbance with wavenumber k , provided the point (k, Ma) lies below the curve for the given Biot number Bi .

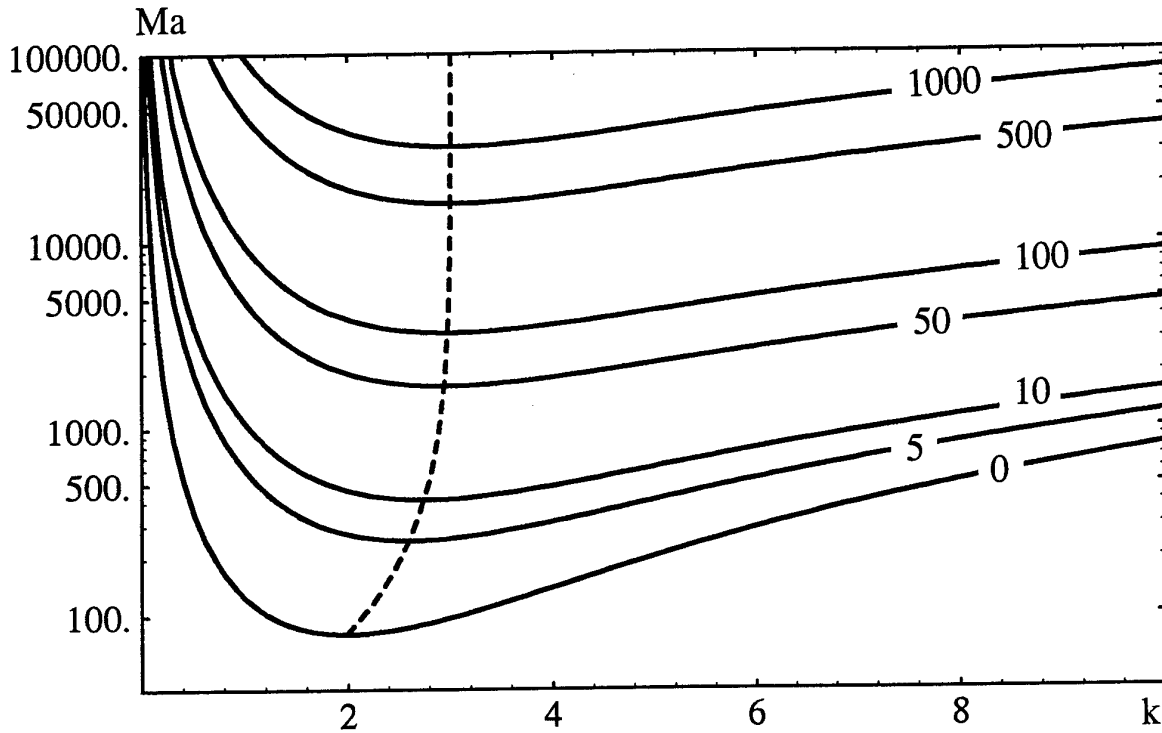


Figure 2.3 : Neutral stability curves for various Biot numbers (indicated for each curve), as given by eq. 75. The critical Marangoni number is given by the minimum these curves as a function of the wavenumber k (dashed line).

The general solution of the stability problem may be written as the superposition

$$\begin{bmatrix} w(x,z,t) \\ T(x,z,t) \end{bmatrix} = \int dk a_k \exp[\sigma_k t + i k x] \begin{bmatrix} w_k(z) \\ T_k(z) \end{bmatrix} \quad (2.76)$$

with arbitrary Fourier coefficients a_k . Then, the critical Marangoni number Ma_c above which

convection sets in is determined by the minimum of the neutral stability curve eq. 75. For $Bi=0$ for example, it is found that $Ma_c=79.6$ for $k_c=1.993$. This value is increasing with the Biot number, as seen on figs 3 and 4.

Just above the critical point $Ma=Ma_c$, disturbances with wavenumbers lying in a very narrow range centred around $k=k_c$ will be amplified, while disturbances with wavenumbers outside this range will be damped. Thus, after some time, the liquid layer is in a convection regime, with a structure that looks like the critical mode with a unique wavenumber k_c . Figure 5 represents this convection structure, obtained by multiplying the critical mode

$$\begin{bmatrix} w_{k_c}(z,t) \\ T_{k_c}(z,t) \end{bmatrix} = \exp[ik_c x] \begin{bmatrix} w_{k_c}(z) \\ T_{k_c}(z) \end{bmatrix} + c.c.$$

by a reasonable amplitude a_{k_c} . In reality, the choice of this amplitude is for the moment arbitrary, because the linear analysis just performed does not allow its calculation.

Note that the basic temperature profile ($-z$ in dimensionless form) has been added to the temperature disturbance in representing the isotherms of fig. 5.

II.5. Importance of a nonlinear analysis

The linear analysis just performed does not allow to determine the amplitudes a_k in the Fourier decomposition 76. In fact, this is not the only limitation of linear analyses. For example, it is seen from eq. 76 that once the threshold of instability is exceeded, some modes with positive growth rate will grow exponentially in time, such that their amplitude can be expected to grow indefinitely. This unrealistic result is due to the fact that the perturbations have been assumed infinitesimal, such that nonlinearities of the basic equations have been neglected (see section II.3, eqs 30-32). When $Ma > Ma_c$, some perturbations grow and may no longer be assumed infinitesimal, such that convective nonlinearities have to be reincorporated in the balance equations (see eqs 7 and 9). This will be done in the next section, and it will be seen that the amplitudes $a_k(t)$ will saturate to some finite-amplitude values.

These nonlinear terms will also lead to couplings between the Fourier modes with different wavenumbers k , which are decoupled at the linear stage. More generally, the linear problem might have been solved in three dimensions (one vertical direction z , and two horizontal directions x and y), and we would have obtained the same equations 64 and 68, with boundary conditions 65 to 67 where $\partial^2/\partial x^2$ has to be replaced by the horizontal Laplacian operator $\Delta_r = \partial^2/\partial x^2 + \partial^2/\partial y^2$. Then, the Fourier integral 76 would have been replaced by

$$\begin{bmatrix} w(x,z,t) \\ T(x,z,t) \end{bmatrix} = \int \int dk_x dk_y a_{\vec{k}} \exp[\sigma_k t + i(k_x x + k_y y)] \begin{bmatrix} w_{\vec{k}}(z) \\ T_{\vec{k}}(z) \end{bmatrix} \quad (2.77)$$

However, due to the isotropy in the horizontal directions, we would have obtained the same spectral problem 70-73, with the wavenumber $k=(k_x^2+k_y^2)^{1/2}$. Then, the linear problem leads

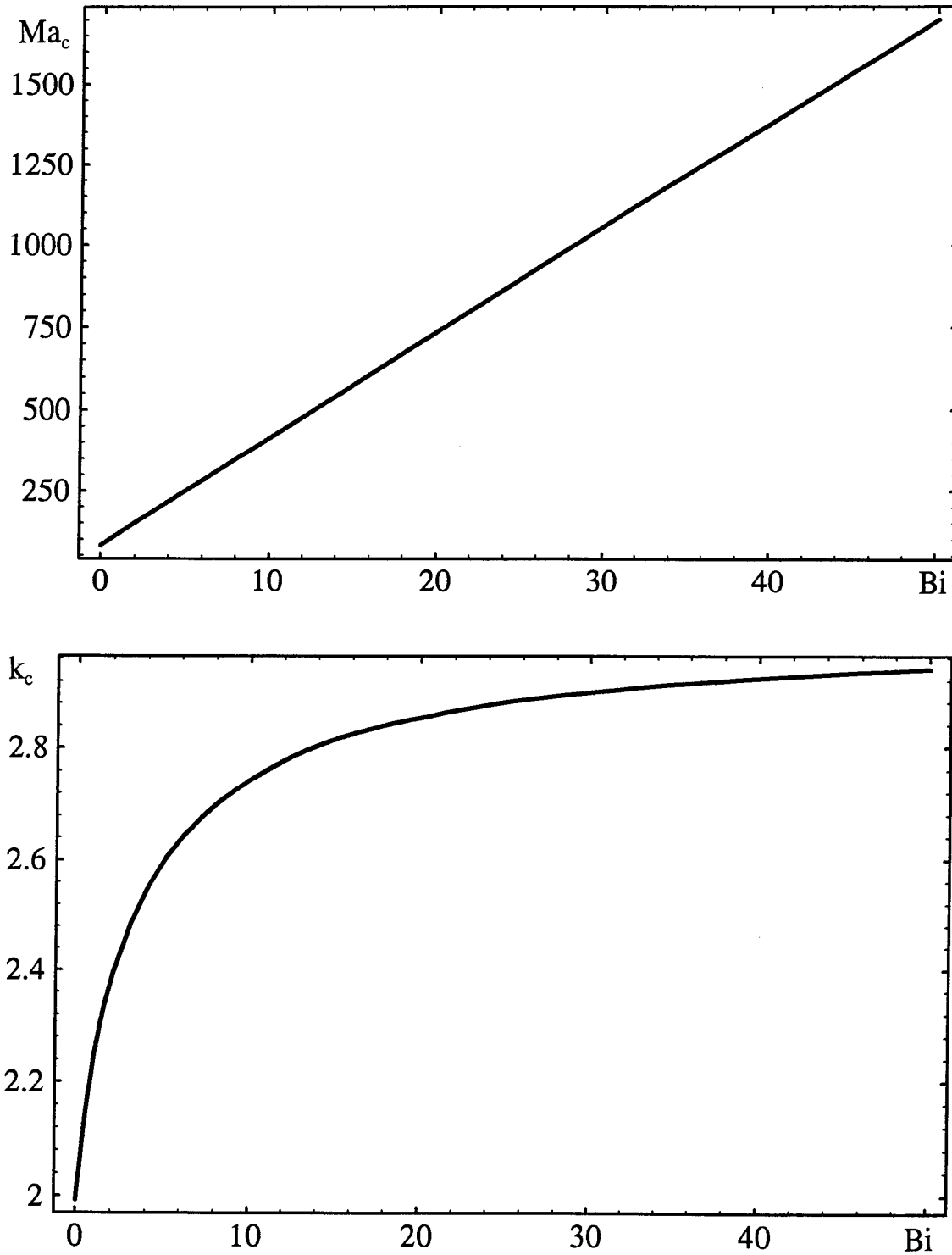


Figure 2.4 : Critical Marangoni number Ma_c (top) and critical wavenumber k_c (bottom) as a function of the Biot number Bi . For $Bi \rightarrow \infty$, $Ma_c \approx 32.1 Bi$ and $k_c \approx 3.01$.

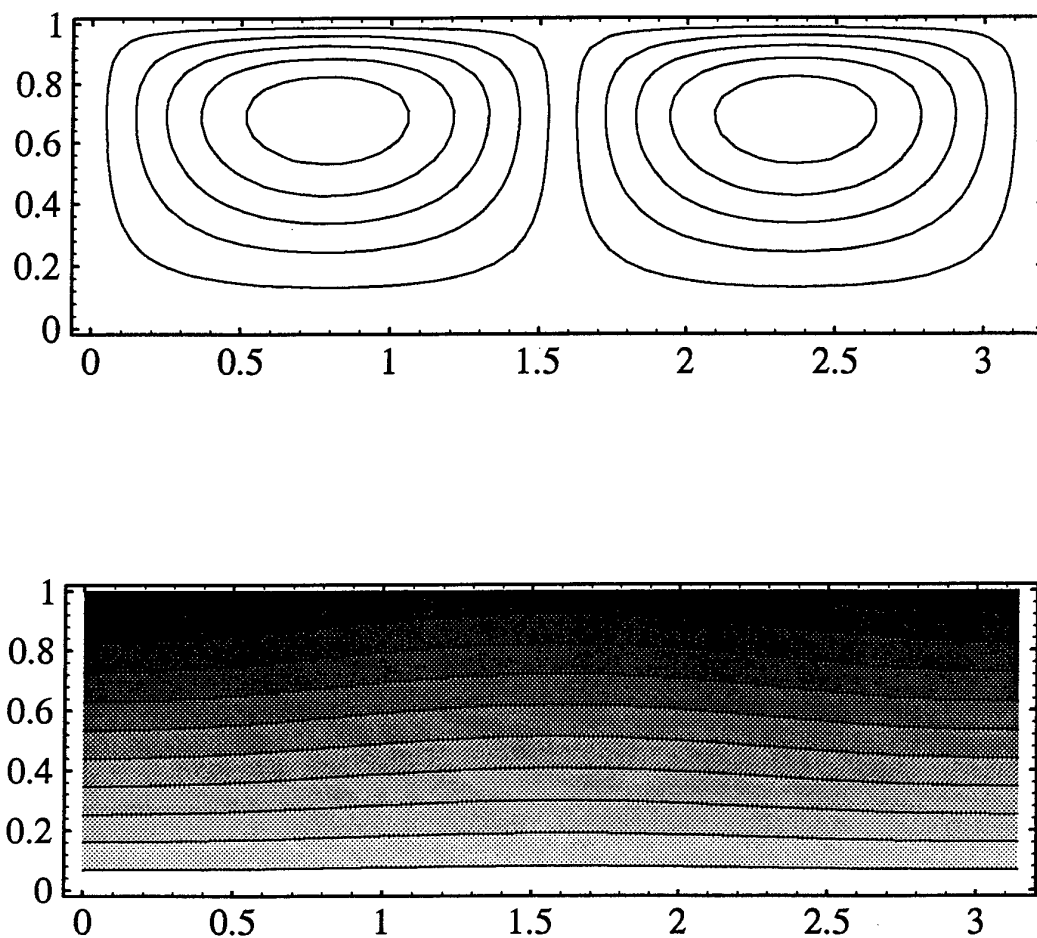


Figure 2.5: Critical perturbations (above : streamlines, below: isotherms). $Bi=0$ ($k_c \approx 2$, leading to periodic convection with wavelength $\lambda = 2\pi/k_c \approx 3.14$ in units of the layer depth).

to the same characteristic relation, and at the critical point, not only one but all the modes lying on the critical circle $k_x^2 + k_y^2 = k_c^2$ are critical (the problem is thus infinitely degenerated). The evolution of the amplitudes $a(k_x, k_y)$ of these modes is decoupled at the linear stage (all grow in time with the same growth constant), but as soon as they leave the

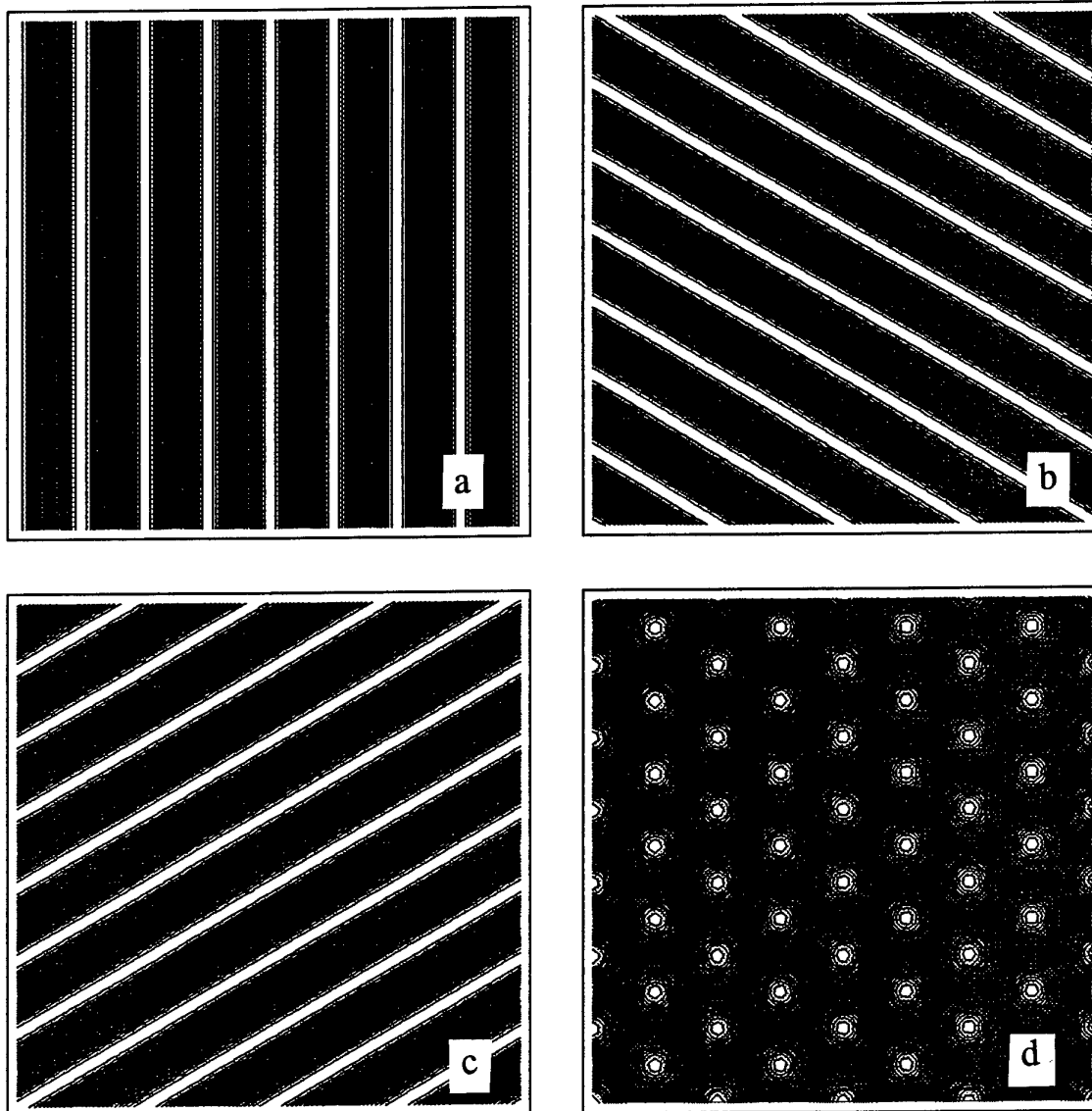


Figure 2.6 : Top view of the free surface isotherms, for 3 roll patterns (a,b,c) with orientations differing by 60° . Their superposition with equal amplitudes leads to hexagons (d). Black regions : cold, white regions : hot.

linear domain, nonlinear interactions between them will provide couplings (and competition) of Fourier modes (convection rolls with axes perpendicular to the wavevector $\vec{k} = k_x \vec{1}_x + k_y \vec{1}_y$) with different orientations. In section III, the competition between 3 roll patterns with wavevectors lying on the critical circle and forming angles of 60° with each other will be investigated, as it is known that this leads to the experimentally observed hexagonal structures (see fig. 6).

In addition to this orientational degeneracy of the linear problem, there exist another "bandwidth" degeneracy, linked to the fact that at a given supercritical Marangoni number Ma , a band of disturbances is amplified (all the wavenumbers lying above the neutral stability curve). In this band, there exist a wavenumber possessing the maximal growth rate. Thus, at the linear stage, this mode will be amplified more quickly, and will dominate other perturbations. Here again, nonlinear couplings between modes with different k will occur, and some disturbances will develop at the expense of others, and determine the wavelength of the final convective structure, which may then not be determined from the linear analysis. This wavelength selection problem will now be examined for two-dimensional perturbations, and assuming that the layer of liquid is sufficiently deep (short-wavelength perturbations).

II.6. Conclusions of section II

In this section, we developed a model describing evaporation of a liquid layer in contact with its vapour, and lying on a heated plate maintained at constant temperature. For a given pressure p_g of the gas phase, evaporation occurs if the temperature of the bottom plate is superior to the saturation temperature corresponding to the pressure p_g (obtained from the classical Clausius-Clapeyron equation). If the temperature of the bottom plate is inferior to this temperature, then condensation occurs. In order for the system to reach a steady (reference) state, we assume that fresh liquid is injected at the bottom plate, at a rate which exactly matches the rate of evaporation (or condensation) at the free surface. This is done in order to mimic steady states reached in evaporating devices such as heat pipes. A graphical determination of the steady mass flux is proposed, together with an analytical result based on a linear approximation valid for mass fluxes that are not too large (more rigorously, the Peclet number of the liquid needs to be small compared to unity).

Our model of evaporation includes the possibility of non-equilibrium effects, i.e. the interface is not assumed to be in a thermodynamic equilibrium state, for which chemical potentials on each side of the interface are equal (the temperature of the interface would then be equal to the saturation temperature computed from the Clausius-Clapeyron equation). Instead, the difference of these chemical potentials is considered as a generalised force (in the sense of irreversible thermodynamics) that generates a mass flux J proportional to it (in the linear approximation). The proportionality coefficient K is a phenomenological coefficient similar to a diffusion coefficient, or a thermal conductivity, and its value is not presently well known. By comparing the expression we obtain for J with the classical Hertz-Knudsen equation, rough estimations are obtained for K , which however depend on the value of the accommodation coefficient β , for which large discrepancies exist between theory and experiment. We thus considered the coefficient K as a free parameter, the limit $K \rightarrow \infty$ defining the state of thermodynamic equilibrium of the interface, and the limit $K = 0$ describing the case of an "impermeable" interface ($J = 0$).

In a second stage, the analysis of the hydrodynamic stability of the computed reference state was performed, taking into account surface tension variation with temperature. A system of equations and boundary conditions describing a one-sided model of convection (the dynamics of the liquid layer is decoupled from the dynamics of the gas) was developed and put under dimensionless form. Order of magnitudes estimates of the dimensionless numbers entering the problem shows that some effects can be neglected. These are the surface deformation (the capillary number Cr is vanishingly small), and the nonlinearity of the basic temperature profile created by evaporation (the Peclet number is small compared to unity, especially for small liquid depth). It is finally shown that the problem of stability reduces to the case of a motionless liquid layer in contact with an inert gas phase at an undeformable interface whose surface tension varies with temperature, the basic temperature profile in the layer being linear (Pearson's problem). Evaporation is incorporated via the presence of a free surface heat transfer coefficient (a Biot number), for which we have obtained a useful formula depending on the characteristics of the liquid (latent heat, Clausius-Clapeyron slope, thermal conductivity and density) and on the phenomenological coefficient K . As the critical Marangoni number (defining the critical value of the thermal gradient, or equivalently of the evaporation mass flux) increases with the Biot number (which increases with K), it can be concluded that evaporation stabilises the layer with respect to Marangoni convection.

II.7. References of section II

1. L.G. Badratinova, P. Colinet, M. Hennenberg and J.C. Legros.
"On thermocapillary and non-equilibrium effects on boiling",
submitted to Microgravity Science and Technology
2. R. Haase, "Thermodynamics of irreversible processes", Dover, New York, 1990.
3. J.P. Burelbach, S.G. Bankoff and S.H. Davis, "Nonlinear stability of
evaporating/condensing liquid films", J. Fluid Mech. 195; pp. 463-494, 1988.
4. I. Prigogine and R. Defay, "Chemical Thermodynamics", Longman, London, 1973.
5. J. R. A. Pearson, "On convection cells induced by surface tension",
J. Fluid Mech. 4, 1958, pp 489-500.

III. FINITE AMPLITUDE REGIMES OF THE SHORT-WAVE INSTABILITY

In this section, a model of the pure thermocapillary instability in layers of infinite depth is developed in the framework of the amplitude equations formalism. We make use of the eigenfunctions at a given Marangoni number Ma (as determined in the previous section) as a basis for the nonlinear problem, rather than the neutral stability functions (as it is often done for weakly nonlinear analyses). It will be shown that third order equations may visibly be extrapolated rather far above the threshold. In particular, results will be obtained about the wavelength selection problem between fastest growing modes (wavenumbers around $k_{max} \sim Ma^{1/2}$ for a zero free surface Biot number) and critical modes ($k_c \rightarrow 0$ and $Ma_c \rightarrow 0$ when the layer depth is infinite). Transient numerical integration of the equations reveals an unbounded growth of the mean wavelength, thus indicating the absence of an intrinsic wavelength for this physical system. This is explained in terms of the mean (horizontally averaged) temperature profile distortion by convection. The final steady state of this evolution (imposed wavelength) is then approximated analytically. Earlier results about the competition between rolls and hexagonal patterns are qualitatively recovered. These solutions are then investigated in the limit $Ma \rightarrow \infty$, where power law relationships are derived for main convective quantities. In particular, a saturation behaviour is obtained for a quantity (the bulk temperature decrease), which can be considered as a measure of the heat transport increase due to convection.

The contents of this section form the subject of one publication entitled "Finite-amplitude regimes of the short-wave Marangoni-Bénard convective instability", P. Colinet, J.C. Legros, Y. Kamotani, P.C. Dauby, and G. Lebon, to appear in Phys. Rev. E, August 95.

III.1. Introduction

When the threshold of the Marangoni-Bénard instability is exceeded, various dissipative structures are experimentally observed, some of them localised near the interface, in the form of small cells eventually embedded in larger convective structures [5], soliton-like propagating waves [6], or interfacial turbulence [7]. In other conditions, Marangoni-Bénard convection is rather similar to the classical buoyancy induced Rayleigh-Bénard convection [8-11], with patterns extending far into the bulk of surrounding liquids, and actually reaching (and influenced by) the boundaries of the experimental vessel. Note that these apparently different forms of convection generally result in substantial increases of heat/mass transfer through the interface.

Figure 1 reproduces the neutral stability results of Pearson [13], as well as results obtained by Scanlon and Segel [14] in the case of a layer of infinite depth (the length d appearing in $Ma = -\sigma_T \beta d^2 / \mu \kappa$ then represents an arbitrary length). At a given Ma , perturbations with wavenumbers in the range lying above the neutral stability curve possess a positive amplification rate. There also exists a particular wavenumber k_{max} in this range which possesses the maximal amplification rate. In slightly supercritical conditions ($Ma \approx Ma_c$), k_{max} is close to the critical wavenumber k_c , and does indeed predict the size of convective (hexagonal) cells observed experimentally. When Ma is increased, k_{max} is seen to increase, and the prediction of the selected wavelength becomes quite complicated, since it involves non-linear competition between modes in the unstable range. Progress has recently been

is not the case for the Marangoni-Bénard instability (the critical wavenumber in a finite layer of depth h scales as $1/h$, such as for the Rayleigh-Bénard instability). However, we may conjecture that this does not rule out the possibility of an intrinsic wavelength, linked to the presence of fastest growing modes (as it seems to be the case for the Rayleigh-Taylor instability [19]). Note that the finite wavenumber of the fastest growing mode generally depends on the driving force amplitude (the thermal gradient in our case). Attempts to answer to the question of the preference of such modes at a given supercritical driving force obviously have to incorporate nonlinear effects in the analysis.

After having described the model in section III.2, in which the derivation of weakly nonlinear results is also described, we discuss this wavenumber selection problem for a two-dimensional geometry (rolls), and in the case where the Prandtl number can be considered infinite (the possibility of boundary-layer instabilities [20], although not observed in our analysis, is also briefly discussed). This is done in section III.3. Buoyancy effects will be neglected, in order to concentrate on the effects of thermocapillarity. Calculations are achieved for a semi-infinite system [14] (i.e. ignoring the presence of a rigid lower boundary, and thus focusing on interfacial short-wave effects). This simplification allows us to obtain approximate analytical results (section III.4) about the convective heat transfer far from the threshold, and about other relevant quantities such as interfacial velocities and surface temperature variations. We end this section by extending some of these results to three-dimensional disturbances, and reconsidering the problem of the competition between rolls and hexagonal convective structures.

III.2. Problem formulation - weakly nonlinear results

We consider a semi-infinite viscous Boussinesquian incompressible fluid in contact with an inert gas phase. The interface is located at the $z=0$ coordinate plane of a cartesian reference frame with unit vectors $\vec{1}_i$ ($i=x,y,z$), and is assumed undeformable (this will allow obtention of analytical results, and is justified since interfacial deformation is known to primarily affect long-wave modes [21,22]). The fluid is located in the domain $z < 0$, and a constant heat flux is injected in the system (a constant temperature gradient $-\beta$ is maintained at $z \rightarrow -\infty$). All equations and boundary conditions are scaled by d (an arbitrary length) for length, d^2/κ for time, βd for temperature and $\mu\kappa/d^2$ for pressure. The Marangoni number $Ma = -\sigma_T\beta d^2/\mu\kappa$ is defined with respect to the length d , instead of the fluid thickness h ($h/d \rightarrow \infty$). Let $\vec{V} = \vec{V}_r + W\vec{1}_z$ be the fluid velocity (\vec{V}_r is the horizontal velocity), T the temperature and p the pressure perturbations with respect to the purely conductive (zero velocity) reference solution. A solution vector U will then be defined by

$$U(\vec{r} = x\vec{1}_x + y\vec{1}_y, z, t) = \begin{bmatrix} \vec{V}_r \\ W \\ p \\ T \end{bmatrix} \quad (3.1)$$

which is assumed to belong to a certain set, say E , of sufficiently derivable functions

satisfying the boundary conditions of the problem : these are

$$\bar{V}_r, W, DT, p \rightarrow 0 \quad \text{for } z \rightarrow -\infty \quad (3.2)$$

$$W = DT + Bi T = 0 \quad \text{for } z = 0 \quad (3.3)$$

where D is the dimensionless z -derivative and Bi is the free surface Biot number $Bi = \alpha d / \lambda$ (α is the free surface heat transfer coefficient and λ the thermal conductivity of the fluid).

The system of partial differential equations for the solution vector U can be written under the general operational form (see eqs 2.7-2.9)

$$\mathcal{L}(U) = Ma M(U) + \Theta\left(\frac{\partial U}{\partial t}\right) + N(U, U) \quad (3.4)$$

where the linear part $\mathcal{L}(U)$ is given by

$$\mathcal{L}(U) = \begin{bmatrix} \Delta \bar{V}_r - \bar{\nabla}_r p \\ \Delta W - Dp \\ DW + \bar{\nabla}_r \cdot \bar{V}_r \\ \Delta T + W \\ [D \bar{V}_r]_{z=0} \end{bmatrix} \quad (3.5)$$

the "evolution part" is defined as

$$\Theta(U) = \begin{bmatrix} 0 \\ 0 \\ 0 \\ T \\ 0 \end{bmatrix} \quad (3.6)$$

and the "constraint part" by

$$M(U) = \begin{bmatrix} 0 \\ 0 \\ 0 \\ 0 \\ -[\bar{\nabla}_r T]_{z=0} \end{bmatrix} \quad (3.7)$$

Finally, the bilinear form N is expressed as

$$N(U_1, U_2) = \begin{bmatrix} 0 \\ 0 \\ 0 \\ \bar{V}_1 \cdot \bar{\nabla} T_2 = \bar{V}_{1r} \cdot \bar{\nabla}_r T_2 + W_1 D T_2 \\ 0 \end{bmatrix} \quad (3.8)$$

In the above relations, $\bar{\nabla}_r = \bar{1}_x \frac{\partial}{\partial x} + \bar{1}_y \frac{\partial}{\partial y}$ is the horizontal gradient, $\bar{\nabla} = \bar{\nabla}_r + \bar{1}_z D$ is the total gradient, and $\Delta = \bar{\nabla}^2$ is the Laplacian operator.

Apart from the fact that pressure is not directly eliminated from the equations, the set (4) of equations together with boundary conditions (2-3) is equivalent to the problem formulation of Scanlon and Segel [14]. Note also that we have included the Marangoni condition as the last component of (4), which has already been shown to simplify the process of deriving amplitude equations [14,23-26].

i) Derivation of amplitude equations

We first decompose U into Fourier modes

$$U(\bar{r}, z, t) = \int U_{\bar{k}}(z, t) \exp(i \bar{k} \cdot \bar{r}) d\bar{k} \quad (3.9)$$

so that horizontal Fourier components $U_{\bar{k}}$ all belong to E (i.e. fulfil boundary conditions (2-3)) and satisfy

$$\mathcal{L}_{\bar{k}}(U_{\bar{k}}) = Ma M_{\bar{k}}(U_{\bar{k}}) + \Theta_{\bar{k}}\left(\frac{\partial U_{\bar{k}}}{\partial t}\right) + \int N_{\bar{k}', \bar{k}-\bar{k}'}(U_{\bar{k}'}, U_{\bar{k}-\bar{k}'}) d\bar{k}' \quad (3.10)$$

which is obtained by projecting (4) on $\exp(-i \bar{k} \cdot \bar{r})$ and by replacing $\bar{\nabla}_r$ by $i \bar{k}$ in linear operators (this is the meaning of the index \bar{k}). The bilinear form N is defined in a similar way. Each Fourier mode is further decomposed as

$$U_{\bar{k}}(z, t) = A_{\bar{k}}(t) U_{\bar{k}}^g(z) + U_{\bar{k}}^D(z, t) \quad (3.11)$$

where $U_{\bar{k}}^g(z)$ is an eigenvector with eigenvalue σ_k ($k = |\bar{k}|$) of the linear spectral problem

$$\mathcal{L}_{\bar{k}}(U_{\bar{k}}^g) - Ma M_{\bar{k}}(U_{\bar{k}}^g) = \sigma_k \Theta_{\bar{k}}(U_{\bar{k}}^g) \quad (3.12)$$

The resolution of (12), detailed in appendix 2, shows that for any $Ma > 0$, $0 < k < Ma/2 Bi$, an isolated eigenvalue σ_k exists (and is such that $\sigma_k + k^2 > 0$). This eigenvalue is the growth rate of the corresponding eigenmode $U_{\bar{k}}^g(z)$, appearing in eq. (11). For every value of Ma and k , there also exists a continuum of solutions of (12) that are bounded for $z \rightarrow -\infty$ (and which correspond to eigenvalues $\sigma < -k^2$). This infinite set of solutions could eventually be used to develop the remainder term $U_{\bar{k}}^D(z, t)$ (the superscript D stands for "damped"), but it turns out to be simpler to compute $U_{\bar{k}}^D$ directly, by a method explained in appendix 1. As exchange of stability holds in our problem [27], eigenvalues σ_k are real and satisfy

$$Ma = \frac{2}{k} \left(-2k\sigma^{-2} + \frac{\sigma^{-1} + 2k^2\sigma^{-2} + 2kBi\sigma^{-2}}{Bi + \sqrt{\sigma + k^2}} \right)^{-1} \quad (3.13)$$

The neutral stability condition is found by the limit of equation (13) for $\sigma \rightarrow 0$:

$$Ma_k = 8k(k + Bi) \quad (3.14)$$

which is the asymptotic form ($k \rightarrow \infty$) of the neutral stability condition of Pearson [13], as

seen on fig.1. A relation between the maximal eigenvalue σ_{\max} , k_{\max} and Ma may be found by differentiating (13) at constant Ma , setting $\partial\sigma/\partial k=0$. This gives, for $Bi=0$ for example:

$$\sigma_{\max} = 2(1+\sqrt{2})k_{\max}^2 = \alpha Ma \quad \text{with } \alpha \approx 0.086 \quad (Bi = 0) \quad (3.15)$$

Although analytical results can also be obtained for $Bi \neq 0$, they are not reproduced here for conciseness. As remarked by Scanlon and Segel [14], the minimum (critical) value of Ma for which instability occurs is zero, due to the absence of stabilisation by a rigid lower boundary of the modes with increasingly large wavelength. However, due to their large inertia, the growth rate of these modes is vanishingly small for all Marangoni numbers. This is depicted in fig.2 : it is seen that modes with wavenumbers between 0 and $k^* = (Ma/8)^{1/2}$ (for $Bi=0$) are unstable, so that their amplitude $A_{\bar{k}}(t)$ in the decomposition (11) should grow exponentially in time, as long as nonlinear effects can be neglected. In fact, it is shown in appendix 1 that the amplitudes $A_{\bar{k}}(t)$ obey evolution equations of the form

$$\frac{\partial A_{\bar{k}}}{\partial t} = \sigma_k A_{\bar{k}} + \int Z_{\bar{k}'\bar{k}} A_{\bar{k}'} A_{\bar{k}-\bar{k}'} d\bar{k}' + \int \int Z_{\bar{k}'\bar{k}''} A_{\bar{k}'} A_{\bar{k}''} A_{\bar{k}-\bar{k}'-\bar{k}''} d\bar{k}' d\bar{k}'' \quad (3.16)$$

These equations are strictly valid near threshold. When the Marangoni number is increased, higher order terms should be included. Equations (16) may then be considered as resulting from a truncated modified Galerkin scheme [15,25]. Another hypothesis underlying the derivation of (16) is that the dynamics of damped modes (i.e. of $U_{\bar{k}}^D$) is determined by the evolution of the "primary" modes $A_{\bar{k}}(t) U_{\bar{k}}^0$ (this amounts to neglect time derivatives of damped modes). This slaving principle [25,26,28], strictly valid near the threshold, is here assumed to be qualitatively valid in the strongly non-linear regime. This can be partly justified by the fact that damped modes cannot bifurcate ($\sigma < -k^2$), whatever high the value of Ma (see also [33]).

Despite these assumptions, our model is expected to reflect physical reality even far from threshold, provided that the eigenmodes $U_{\bar{k}}^0$ are used for the Galerkin basis, rather than the neutral stability functions $U_{\bar{k}}^0$. In order to illustrate the differences between these different approaches, we now turn to the derivation of weakly nonlinear results [14, 23-26], for which the latter option is sufficient.

ii) Weakly nonlinear results

Making use of $U_{\bar{k}}(z,t) = A_{\bar{k}}(t) U_{\bar{k}}^0(z) + U_{\bar{k}}^D(z,t)$, instead of eq.11, and following a procedure similar to that described in appendix 1, we are left with amplitude equations identical to eq. (16), although with different coefficients. It is obvious that coefficients of the quadratic and cubic terms do not depend on Ma . It can also be shown that the coefficient of the linear term is the first term of a Taylor expansion of $\sigma_k(Ma)$ around $Ma=Ma_k$, i.e.

$$\sigma_k^0 = \frac{k(Ma - Ma_k)}{4(2k + Bi)} \quad (3.17)$$

where a superscript 0 will denote a value of a coefficient computed by using neutral stability functions.

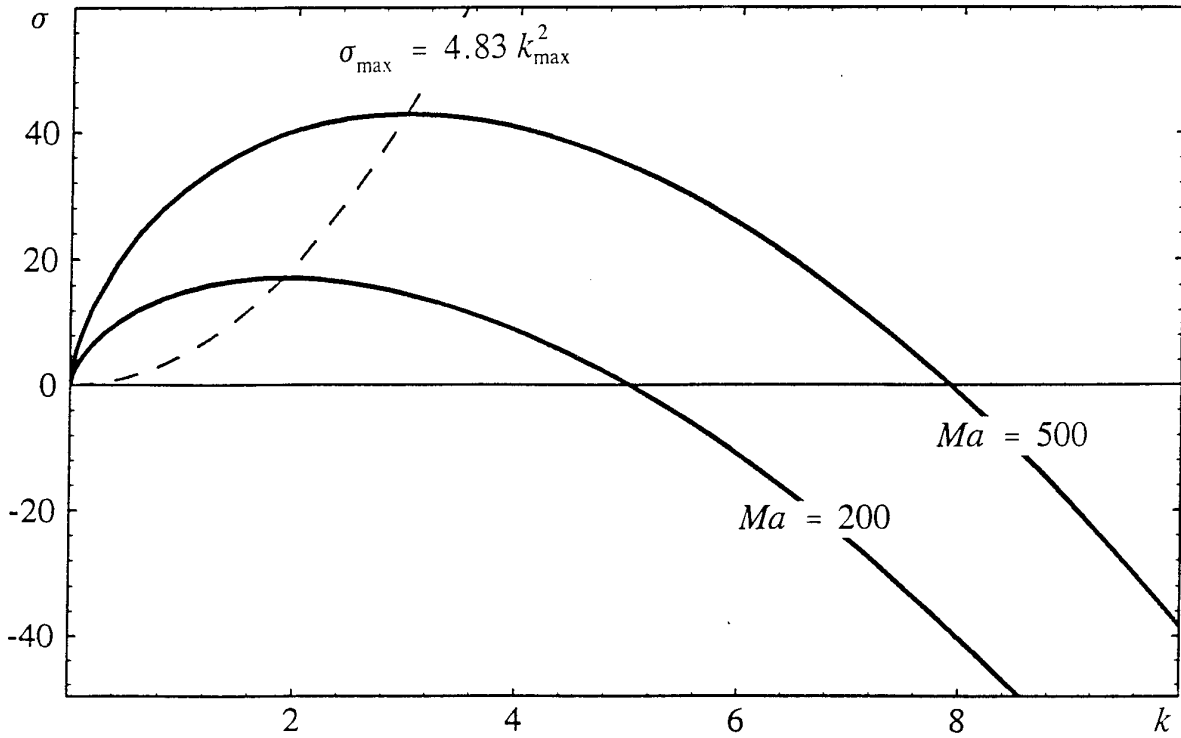


Figure 3.2 : The growth rate σ as a function of the wavenumber k for different Marangoni numbers Ma , and for $Bi=0$. The dotted line represents the locus of the fastest growing perturbations, given by eq. (15).

Note that eq. (17) is an insufficient approximation for low Biot numbers. As an indication, the mode $k=0$ is found to be amplified for $Bi=0$ and $Ma>0$ (which differs from the exact behaviour of the growth constant, as seen in fig.2).

From equations (9) and (11), it is seen that a roll mode with wavevector \bar{k}_0 is described by $A_{\bar{k}} = a_1(t) \delta(\bar{k} - \bar{k}_0) + \bar{a}_1(t) \delta(\bar{k} + \bar{k}_0)$, where δ is the Dirac-delta function, and an overbar denotes the complex conjugate. Substituting into (16) leads to the Ginzburg-Landau equation

$$\frac{\partial a_1}{\partial t} = \sigma_{k_0}^0 a_1 + (2Z_{111}^0 + Z_{-111}^0) a_1 |a_1|^2 \quad (3.18)$$

where Z_{111}^0 and Z_{-111}^0 stand for $Z_{\bar{k}_0 \bar{k}_0 \bar{k}_0}^0$ and $Z_{-\bar{k}_0 \bar{k}_0 \bar{k}_0}^0$ respectively.

Defining a reduced distance to the threshold by

$$\epsilon = (Ma - Ma_{k_0}) / Ma_{k_0} \quad (3.19)$$

it is seen that at $\epsilon=0$, the rest state $a_1=0$ undergoes a pitchfork bifurcation to the steady

amplitude

$$|a_{1s}| = \left[\frac{32(Bi + 3k_0)}{(Bi + k_0)(39Bi^2 + 248Bi k_0 + 353k_0^2)} \epsilon \right]^{\frac{1}{2}} \quad (3.20)$$

obtained after evaluation of the cubic coefficients (see details in appendix 3).

Although strictly valid near the threshold, the limitations of this weakly nonlinear model for large ϵ are well known. Consider for example the temperature perturbation averaged in the horizontal direction (i.e. its $k=0$ Fourier component) :

$$\langle T \rangle = T_{\vec{k}=0}^D(z) = 2 |a_1|^2 T_{01}^D(z) = O(\epsilon) \quad (3.21)$$

where $T_{01}^D(z)$ is the only non-zero component of $U_{01}^D(z)$ (appendix 3). The total averaged temperature profile is obtained by adding the reference profile $-z$ to (21), and is represented in fig. 3, for several values of ϵ . It is seen that in a region of depth $O(1/k_0)$ below the interface, the temperature profile is distorted (and somewhat homogenised) by Marangoni convection. It is also seen that unrealistic temperature distributions (strongly negative values of the mean temperature, leading to large unrealistic cold spots in steady regimes) are obtained for ϵ superior to about 1.5. Defining Δ as the bulk temperature decrease with respect to its value in the conductive rest state, we may compute that

$$\Delta^0 = -2 |a_{1s}|^2 \lim_{z \rightarrow -\infty} T_{01}^D(z) = \frac{32(Bi + 3k_0)(5Bi + 7k_0)}{k_0(39Bi^2 + 248k_0Bi + 353k_0^2)} \epsilon \quad (3.22)$$

where the superscript 0 again denotes the weakly nonlinear result. The result (22) of course diverges for $\epsilon \rightarrow \infty$.

The importance of obtaining a better approximation of the bulk temperature decrease Δ is justified by the fact that it can be considered as equivalent to the classical Nusselt number Nu (more exactly to $Nu-1$, which is also quadratic in the amplitudes). Indeed, for systems in which the temperature difference is kept constant (such as Rayleigh-Bénard convection between conducting boundaries), Nu is defined as the dimensionless ratio of the total to the conductive heat flux, and therefore is a measure of the increase of the heat flux due to convection. For systems where the heat flux is kept constant (as in the present work), the decrease of the temperature difference between bulk and interface may also be perceived as an increase of the apparent thermal conductivity of the system, due to Marangoni-Bénard convection. In the next sections, it is shown that by using eigenvectors (12) instead of neutral stability functions, a more realistic description of convective fields for large Ma can be obtained, together with interesting power laws for the variation of convective quantities in the limit $Ma \rightarrow \infty$.

III.3. Numerical results and physical interpretation

In this section, we present results obtained by direct numerical integration of the set (16), for a two-dimensional domain of lateral length $L=2\pi/k_0$ with periodic boundary conditions.

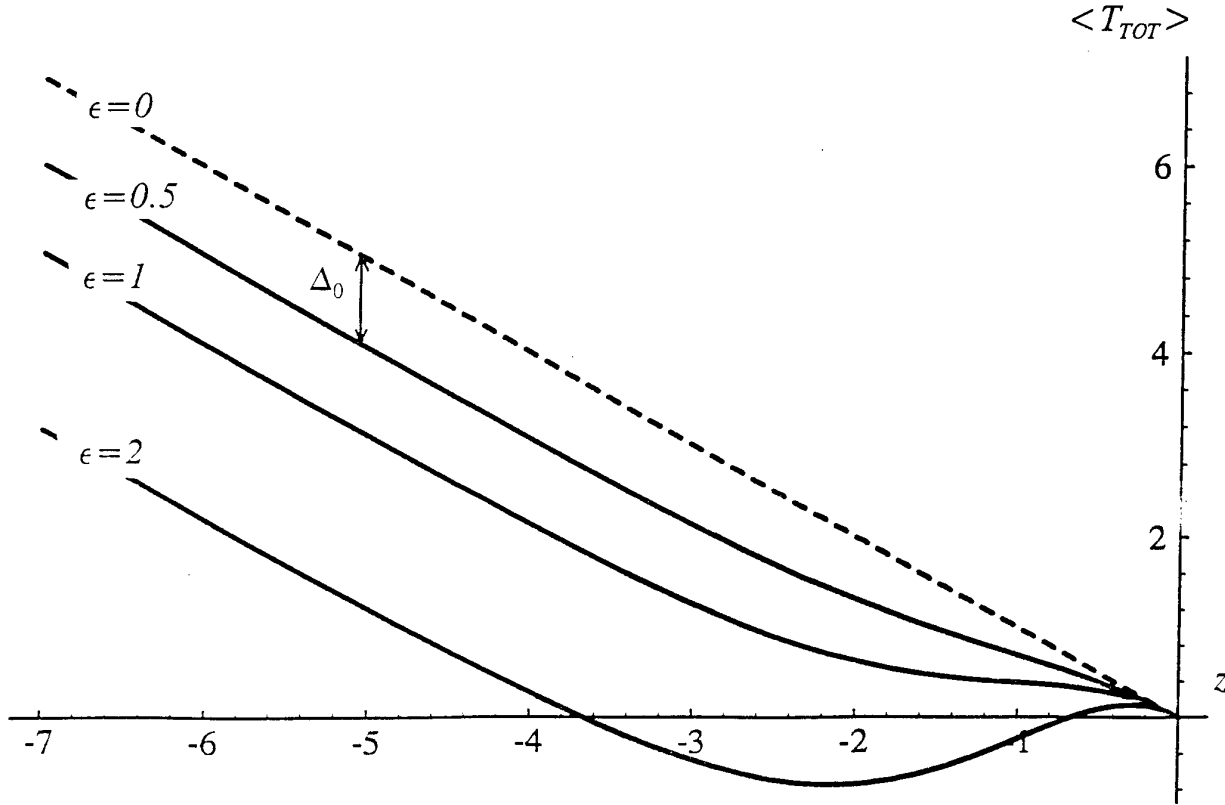


Figure 3.3 : The total temperature $\langle T_{TOT} \rangle$ averaged in the horizontal plane as a function of the vertical coordinate z , as computed from weakly non-linear results, and for different values of $\epsilon = (Ma - Ma_c)/Ma_c$. The Biot number is $Bi=0$, and the basic wavenumber is $k_0=1$. The distortion of the averaged temperature profile in the convective region near the interface $z=0$ creates a decrease Δ_0 of the bulk temperature with respect to the purely conductive value (dotted line, $\epsilon=0$). Δ_0 is here defined for $\epsilon=0.5$.

The amplitude of the Fourier modes is given by

$$A_{\bar{k}}(t) = \sum_{n=-N, n \neq 0}^{+N} a_n(t) \delta(\bar{k} - n\bar{k}_0) \quad (3.23)$$

with $\bar{a}_n(t) = a_{-n}(t)$, and N sufficiently large to ensure numerical convergence. Substituting (23) in relation (16) leads to

$$\frac{\partial a_m}{\partial t} = \sigma_m a_m + \sum_p Z_{p,m} a_p a_{m-p} + \sum_{p,q} Z_{p,q,m} a_p a_q a_{m-p-q} \quad (3.24)$$

where σ_m stands for σ_{mk_0} , $Z_{p,m}$ for $Z_{p\bar{k}_0, m\bar{k}_0}$ and $Z_{p,q,m}$ for $Z_{p\bar{k}_0, q\bar{k}_0, m\bar{k}_0}$, which are calculated as a function of the Marangoni number Ma .

In the following, we will take advantage of the fact that the length scale d of the problem is still arbitrary. We may thus choose $k_0=1$, which means that the dimensional length of the

periodic box is $2\pi d$. From eq. (14), the critical Marangoni number is given by $Ma_c = Ma_{k=1} = 8(1 + Bi)$.

The system of equations (24) has been integrated for a wide range of Marangoni and Biot numbers. Despite the large number of unstable modes in some cases (increasing with Ma), and the presence of resonant quadratic terms (which are generally responsible for complicated phase coupling effects [29,30]), the long-term behaviour appears to be surprisingly simple: a steady state is always reached, which is strongly dominated by the fundamental mode $n=1$. Since the number of modes N needed to ensure convergence is increasing with Ma (see fig.2), computer resources limited our investigations to Marangoni numbers of about $Ma=500$ (for $Bi=0$, and $N=20$).

We have also considered a simplified version of the system (24), which allows us to simulate the evolution of a larger number of amplitudes. This model is obtained by setting all cubic coefficients $Z_{p,q,m}$ with $p \neq m$ equal to zero. We then obtain

$$\frac{\partial a_m}{\partial t} = [\sigma_m - \sum_{q=1}^N S_{m,q} |a_q|^2] a_m + \sum_p Z_{p,m} a_p a_{m-p} \quad (3.25)$$

with $S_{m,q} = -2 Z_{m,q,m}$. From eq. (25), this quantity is seen to represent the strength with which the presence of the mode q lowers the effective growth rate of the mode m . The physical mechanism responsible for this stabilising effect consists in the distortion of the mean temperature profile by convection (see fig.3), which lowers the destabilising temperature gradient. A comparison of the time evolution and of the steady state values predicted by the full system (24) and the reduced set (25) reveals that the results differ only slightly (by less than 10% on the value of typical convective quantities at steady state, as shown in fig. 6). In view of this rather good concordance, the mean temperature profile distortion by convection may be considered as a dominating effect in the nonlinear competition between unstable modes. Implications for wavelength selection between fastest growing and critical modes are discussed later on in this section.

Since it is legitimate to admit that the simplified system (25), that can be considered as a "mean-field" [32] version of the problem, is useful for simulating the interactions of a larger number of modes (up to $N=75$), larger Marangoni number values can also be investigated. Again, even for Marangoni numbers as large as 4000 (for $Bi=0$, i.e. $\epsilon \approx 500$), the long-term behaviour is not modified, independently of the initial conditions (here selected as a numerical "white noise", i.e. randomly chosen complex amplitudes of magnitude 10^{-8} to 10^{-3}): the final state is still steady and dominated by the fundamental mode.

A sequence of a typical transient simulation is represented on fig.4. For sufficiently small initial perturbations, a convective structure dominated by the fastest linearly growing mode (the mode closest to k_{max}) is observed after a relatively short time. This is the case as long as non-linear effects can be neglected. At higher time intervals, this k_{max} -structure is progressively replaced by larger and larger wavelength structures, via a complex process of coalescence of neighbouring convective cells. This evolution finally tends to the steady state with 2 convective cells (1 period) occupying the entire domain, as expected (fundamental mode). The properties of this steady state will be investigated in the next section.

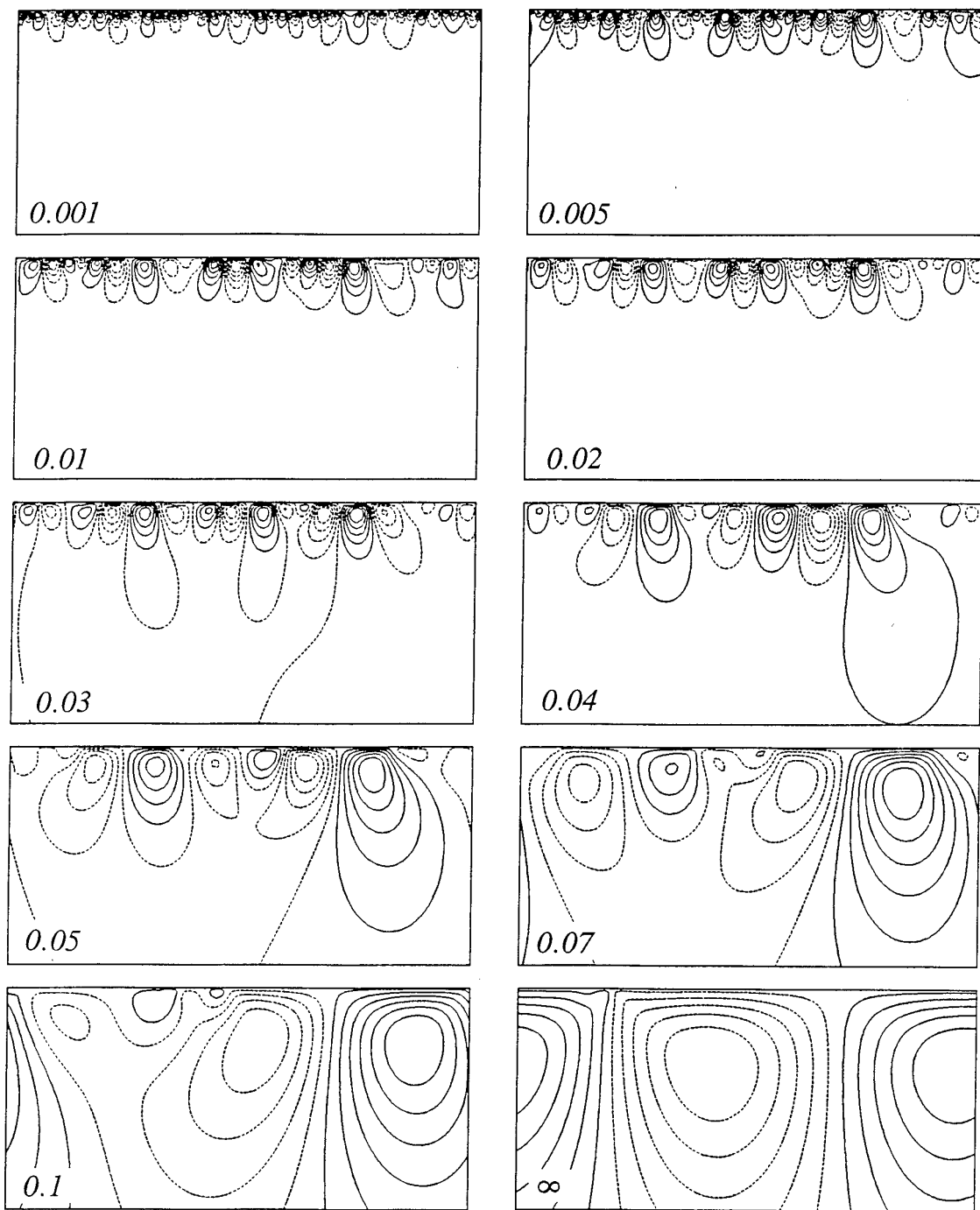


Figure 3.4 : The evolution of the streamfunction pattern for $Ma=3000$ ($\epsilon=374$), $Bi=0$, $N=75$. Solid closed curves correspond to clockwise motion. The initial condition was selected as a random noise of amplitude 10^{-5} . The streamfunction is rescaled at each snapshot (the reduced time is indicated). The fastest growing perturbation is dominating for times $t < 0.03$. A continuous growth of the mean wavelength of the pattern is observed, the later stages of which tend to a steady state with two convective cells (1 period) in the simulation domain, after a time of order unity (in units $L^2/4\pi^2\kappa$, where L is the horizontal period).

It is interesting to compare fig.4 with the experimental observations made by Lindé [5], in mass transfer systems. Note that these systems actually correspond to high values of Bi , since the diffusion coefficients are generally much larger in the gas than in the liquid phase. However, our simulations were not found strongly dependent on Bi for large Ma . Lindé interpreted the observed growth of the mean wavelength of the convective pattern as an effect due to the non-stationary mass transfer occurring in his experiments. Indeed, after that the experiment is started by putting in contact a gas phase containing a surface active solute with the liquid phase, the diffusion of this solute through the interface creates a growing diffusive boundary layer, which induces convective motions in the liquid, with a wavelength that scales with the thickness of this boundary layer.

Since a natural length scale such as this boundary layer thickness is absent in our formulation, the wavelength selection observed in fig.4 has to be intrinsically related to the non-linear mechanism of heat (or mass) convective transport. This effect was indeed shown (see fig.3) to create an homogenisation of the temperature (or concentration) profile in a convective region located below the interface. This is also apparent in fig.5, which represents the temperature profile averaged along the horizontal direction corresponding to the evolution depicted in fig.4. It is seen that the temperature uniformisation due to convection is more important at large times, when the penetration depth is large. The growth mechanism can be explained by the following considerations : suppose that at one particular instant, the convective structure has a given mean wavelength λ . Since the convective cells have to preserve a certain height/width ratio, temperature is practically homogenised in a region of depth λ below the interface. Modes with wavelengths smaller than λ may be considered as

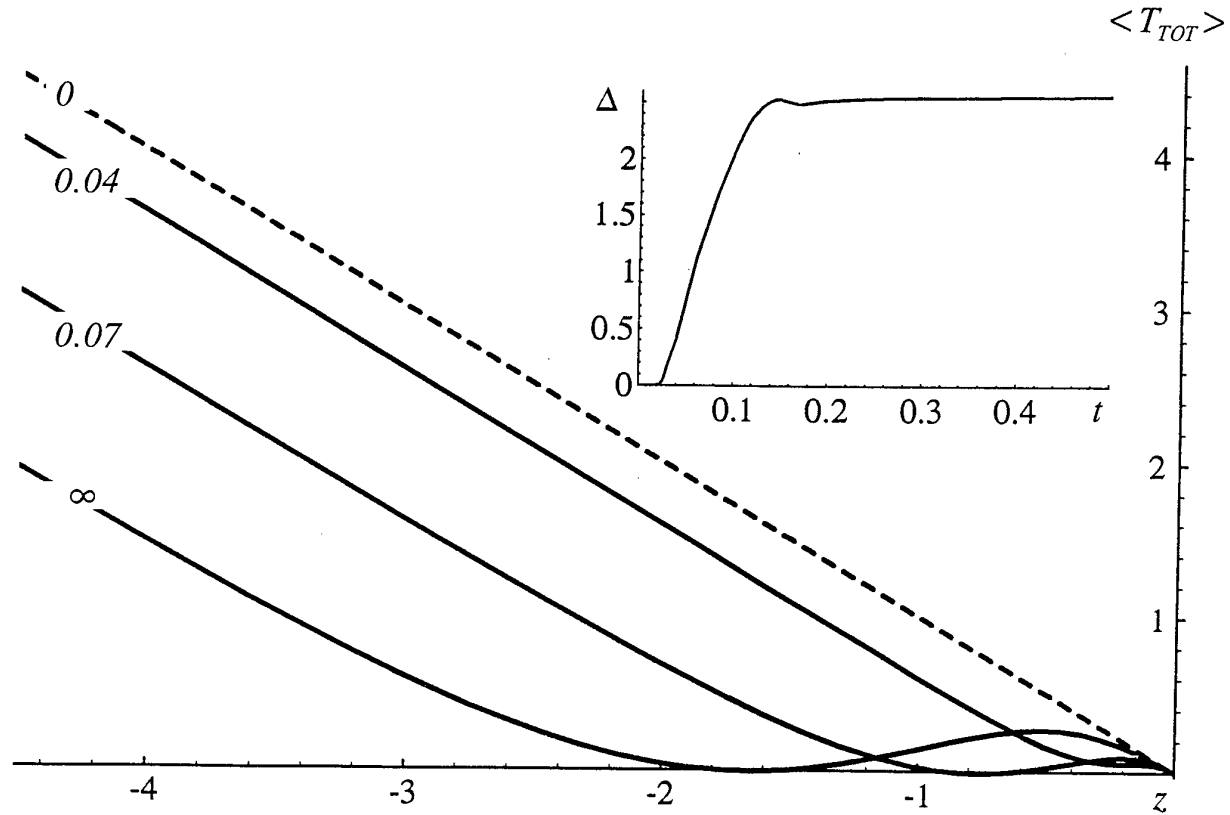


Figure 3.5 : The evolution of the total temperature $\langle T_{TOT} \rangle$ averaged in the horizontal plane as a function of the vertical coordinate z . The Biot number is $Bi=0$. Several times are considered, which correspond to the simulation depicted in fig.4. An homogenisation of the temperature in a domain whose depth is growing with time occurs, which results in a growth of the bulk temperature decrease Δ with time (see insert).

stable, since they see a nearly isothermal environment. At the contrary, modes with wavelengths larger than λ can penetrate deeply enough into the bulk of the liquid and bring hot fluid from the still conductive zone, to the interface. The effective growth rate of these modes remains nearly unchanged by the convective structure, so that these modes continue to grow (but slower and slower due to their growing inertia), and tend to replace smaller wavelength structures. The pattern wavelength λ may thus be expected to grow indefinitely, at least in an infinite system. In real experiments, the final wavelength will probably be determined by the actual depth of the experimental container (thus near the critical wavelength), indicating that an intrinsic wavelength is likely to be inexistent for the pure Marangoni-Bénard problem. Note that on the point of view of wavelength selection, the evolution described above presents some similarities with coarsening processes observed during spinodal decomposition phenomena in binary mixtures [36].

A last remark about fig.5 concerns the temperature profile near the interface. Since the vertical velocity is vanishing at the interface, some kind of thermal boundary layer is created

there, in which the temperature gradient quickly recovers its bulk value. In Rayleigh-Bénard convection, boundary layer effects are known to play a decisive role in the mechanisms of transition to turbulence (especially for high Prandtl number fluids [20]). However, despite the very high values of the Marangoni number, boundary layer instabilities have not been observed in our simulations, probably due to the different nature of these boundary layers (in particular the absence of no-slip condition for Marangoni-Bénard problems). Furthermore, it cannot be rejected that this kind of phenomena could appear for larger driving forces than those investigated in this work (up to $Ma=4000$). Finally, let us mention that a direct comparison of the results obtained from the present model (amplitude equations limited to third order) with a finite difference resolution of the governing equations is in progress, and will be reported elsewhere. Preliminary results exhibit a satisfactory agreement concerning the qualitative evolution of the system (i.e. the growth of the mean wavelength up to the final steady state with the largest wavelength). This confirms that the most important ingredient responsible for this process is indeed the mean temperature profile distortion by convection. This in turn indicates that mean-field approximations [32], neglecting all nonlinear effects except the change of the mean temperature profile owing to the convective heat transport, can lead to satisfactory approximations of highly supercritical behaviours.

III.4. Analysis of steady states

i) Bifurcation of rolls

Since the steady state reached by both full (24) and reduced (25) models is strongly dominated by the fundamental mode $n=1$, we seek for an approximate solution by setting to zero all harmonics a_n with $n > 1$. The set (25) then reduces to the single equation

$$\frac{\partial a_1}{\partial t} = [\sigma - S_{11} |a_1|^2] a_1 \quad (3.26)$$

describing a pitchfork bifurcation similar to eq. (18) but where the coefficients are now computed from the eigenfunctions U_k^σ , and thus depend on Ma . After computation of these coefficients, the steady convective solution of (26) is finally found as

$$|a_1|^2 = \frac{\sigma}{S_{11}} = \frac{(Ma - Ma_c) \sigma^2 (3 + \sqrt{1 + \sigma})^3}{(1 + Bi)^2 (512 (Ma + \sigma^2) + Ma (3\sigma - 8) (3 + \sqrt{1 + \sigma})^3)} \quad (3.27)$$

where the growth rate σ is solution of the dispersion relation (13), and thus also depends on Ma . According to eq. (26), the solution (27) is stable provided $\sigma > 0$, which is equivalent to $Ma > Ma_c = 8(1 + Bi)$ (we have set $k_0 = 1$).

The decrease Δ of the bulk temperature due to Marangoni convection, as represented in figs 3 and 5, is expressed by

$$\Delta = \frac{8(Ma - Ma_c)(3 + \sqrt{1 + \sigma})^3 (\sigma - 2 + \frac{8(Ma + \sigma^2)}{Ma(1 + \sqrt{1 + \sigma})^2})}{512(Ma + \sigma^2) + Ma(3\sigma - 8)(3 + \sqrt{1 + \sigma})^3} \quad (3.28)$$

This expression is represented in fig.6, together with results obtained from the integration of the full system (24) and of the reduced system (25). Another result found in fig.6 is the

expression (22), which reduces to $\Delta^0 = 672\epsilon/353$ for $Bi=0$ and $k_0=1$. Clearly, this result is only valid near the threshold. At the contrary, the expression (28) for Δ leads to the result $\Delta = 14/5 \epsilon$ near the threshold (which is overestimated, due to the negligence of the stabilising coefficient Z_{III} , see eq.18). Nevertheless, eq. (28) appears to be a better approximation of the bulk temperature decrease for large Marangoni numbers (because Z_{III} becomes negligible compared to Z_{II}). The corresponding mean temperature profile can also be shown to be more realistic, since it does not exhibit cold spots as those appearing in fig.3, but is rather close to fig.5. The behaviour at an infinite Marangoni number is given at the end of this section.

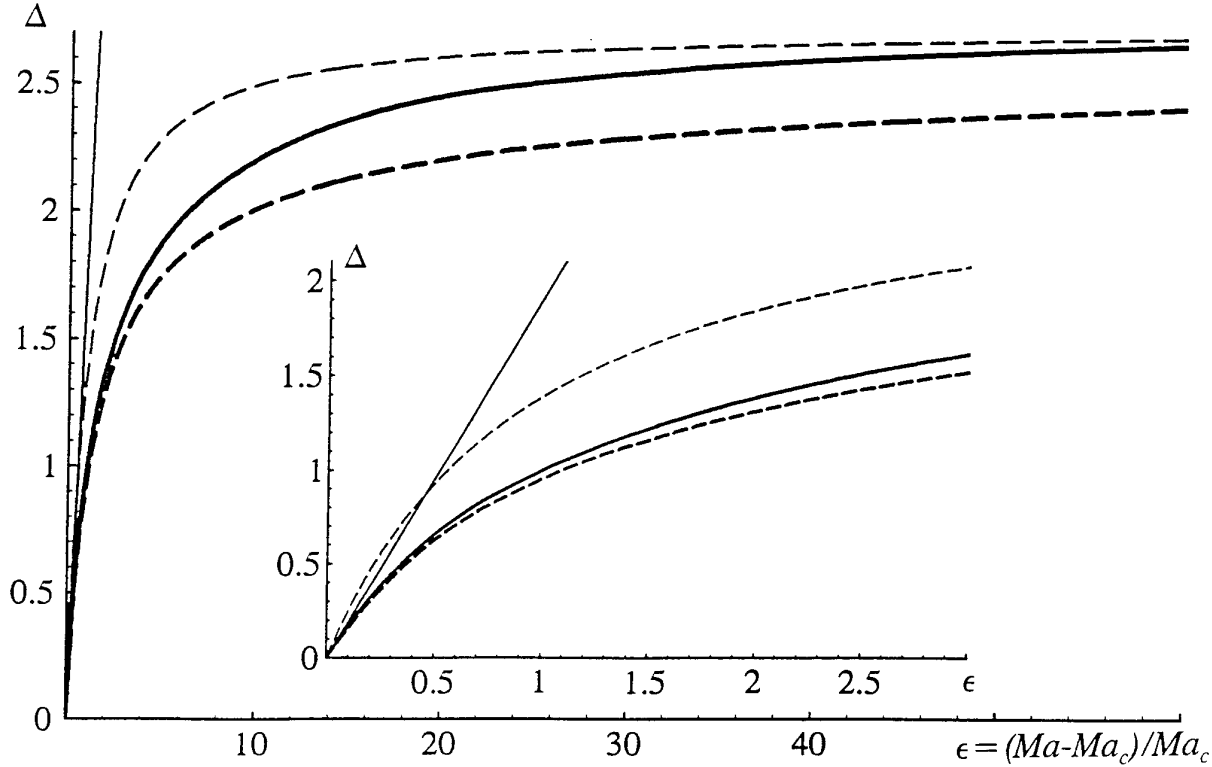


Figure 3.6 : The bulk temperature decrease Δ as a function of the distance to the threshold $\epsilon = (Ma - Ma_c) / Ma_c$ for $Bi=0$. Thick full curve : results of the numerical integration of the full system (25). Thick dotted curve : numerical integration of the "mean-field" system (24). Thin full line : the weakly nonlinear result $\Delta^0 = 672\epsilon/353$. Thin dotted curve : the analytical result for Δ given as eq. 28 of the text. The insert represents a zoom of a region near the origin.

ii) Competition between hexagons and rolls

In view of the good agreement between the analytical result (28) and the results of the numerical integration of (24), we shall reexamine the problem of the competition between three sets of rolls forming angles of 60° with each other.

We thus consider

$$A_{\vec{k}} = a_1(t)\delta(\vec{k}-\vec{k}_1) + a_2(t)\delta(\vec{k}-\vec{k}_2) + a_3(t)\delta(\vec{k}-\vec{k}_3) + \bar{a}_1(t)\delta(\vec{k}+\vec{k}_1) + \bar{a}_2(t)\delta(\vec{k}+\vec{k}_2) + \bar{a}_3(t)\delta(\vec{k}+\vec{k}_3) \quad (3.29)$$

where the ordering of unit vectors \vec{k}_i , $|i| = 1, 2, 3$ is defined by fig.7.

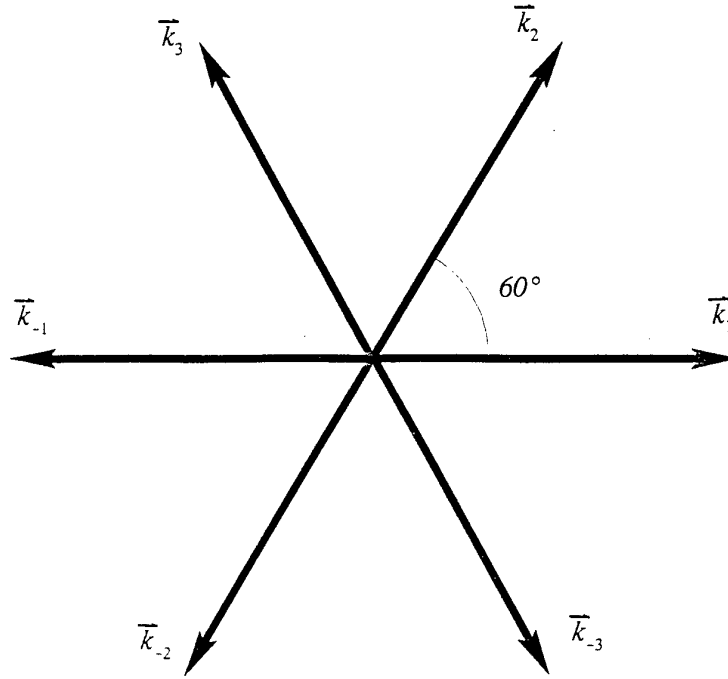


Figure 3.7 : Definition of the basic wavevectors for the study of the competition between rolls and hexagons ($|\vec{k}_i| = 1$).

From eq. (16), the corresponding amplitude equations are

$$\begin{aligned}\frac{\partial a_1}{\partial t} &= \sigma a_1 + \delta a_2 \bar{a}_3 - \left[\alpha_1 |a_1|^2 + \alpha_2 (|a_2|^2 + |a_3|^2) \right] a_1 \\ \frac{\partial a_2}{\partial t} &= \sigma a_2 + \delta a_1 a_3 - \left[\alpha_1 |a_2|^2 + \alpha_2 (|a_1|^2 + |a_3|^2) \right] a_2 \\ \frac{\partial a_3}{\partial t} &= \sigma a_3 + \delta \bar{a}_1 a_2 - \left[\alpha_1 |a_3|^2 + \alpha_2 (|a_1|^2 + |a_2|^2) \right] a_3\end{aligned}\quad (3.30)$$

where

$$\delta = 2 Z_{1,2} \quad (3.31)$$

$$\alpha_1 = -(2 Z_{1,1,1} + Z_{-1,1,1}) \quad (3.32)$$

$$\alpha_2 = -2 (Z_{1,1,1} + Z_{2,1,1} + Z_{-2,1,1}) \quad (3.33)$$

and where $Z_{p,q,r}$ stands for $Z_{\vec{k}_p, \vec{k}_q, \vec{k}_r}$ (symmetry considerations have been used to minimize the number of coefficients to be calculated). The discussion of the gradient system (30) is well-known [23-26,37] : writing $a_n = r_n \exp[i\varphi_n]$, we obtain the equation $\partial\varphi/\partial t = -\delta \sin\varphi (r_1^2 r_3^2 + r_2^2 r_3^2 + r_1^2 r_2^2)/r_1 r_2 r_3$ (with $r_n \neq 0$) for $\varphi = \varphi_2 - \varphi_1 - \varphi_3$, showing that $\varphi=0$ and $\varphi=\pi$ are the only possible stationary values of φ .

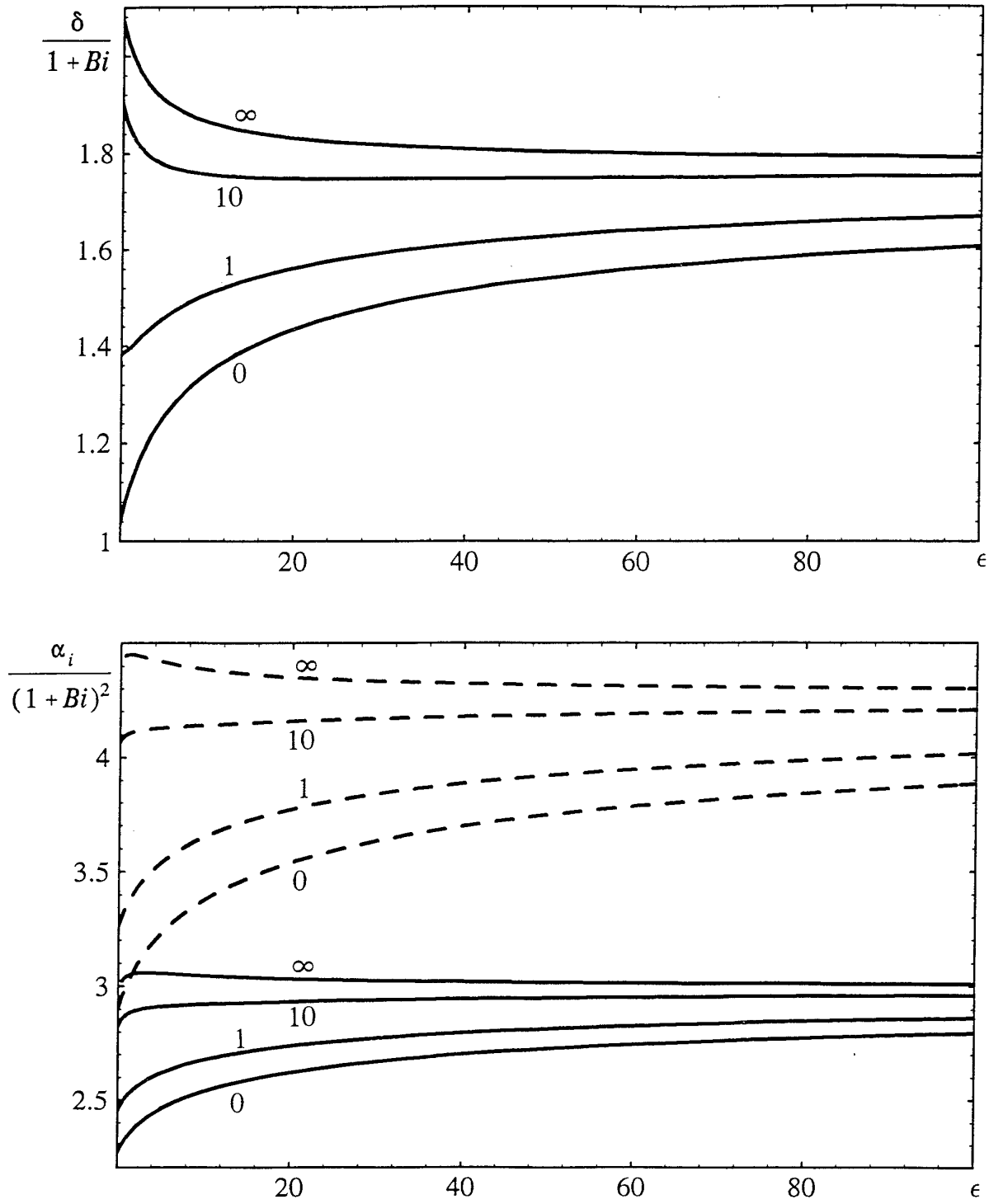


Figure 3.8 : The coefficients $\delta/(1+Bi)$ (upper graph), $\alpha_1/(1+Bi)^2$ (lower graph, solid curves) and $\alpha_2/(1+Bi)^2$ (lower graph, dashed curves) as a function of the distance to the threshold $\epsilon = (Ma - Ma_c(Bi))/Ma_c(Bi)$, for various Biot numbers Bi (indicated on each curve).

Then, it is found that qualitatively different fixed points of eqs 30 are (when $\alpha = \alpha_1 + 2\alpha_2 > 0$):

- rest solution : $r_1 = r_2 = r_3 = 0$ (3.34)

- roll solutions : $r_2 = r_3 = 0, r_1 = (\sigma/\alpha_1)^{1/2}$ (3.35)

- up-hexagons solutions : $\varphi = 0, r_1 = r_2 = r_3 = (\delta \pm (\delta^2 + 4\sigma\alpha)^{1/2})/2\alpha$ (3.36)

- down-hexagons solutions : $\varphi = \pi, r_1 = r_2 = r_3 = (-\delta + (\delta^2 + 4\sigma\alpha)^{1/2})/2\alpha$ (3.37)

The analytical form of the coefficients δ , α_1 , and α_2 (depending on Ma) is not written down for conciseness. Rather, fig. 8 presents their variation with the distance to the threshold ϵ for various Biot numbers. Bifurcation diagrams are represented on figs 9 and 10.

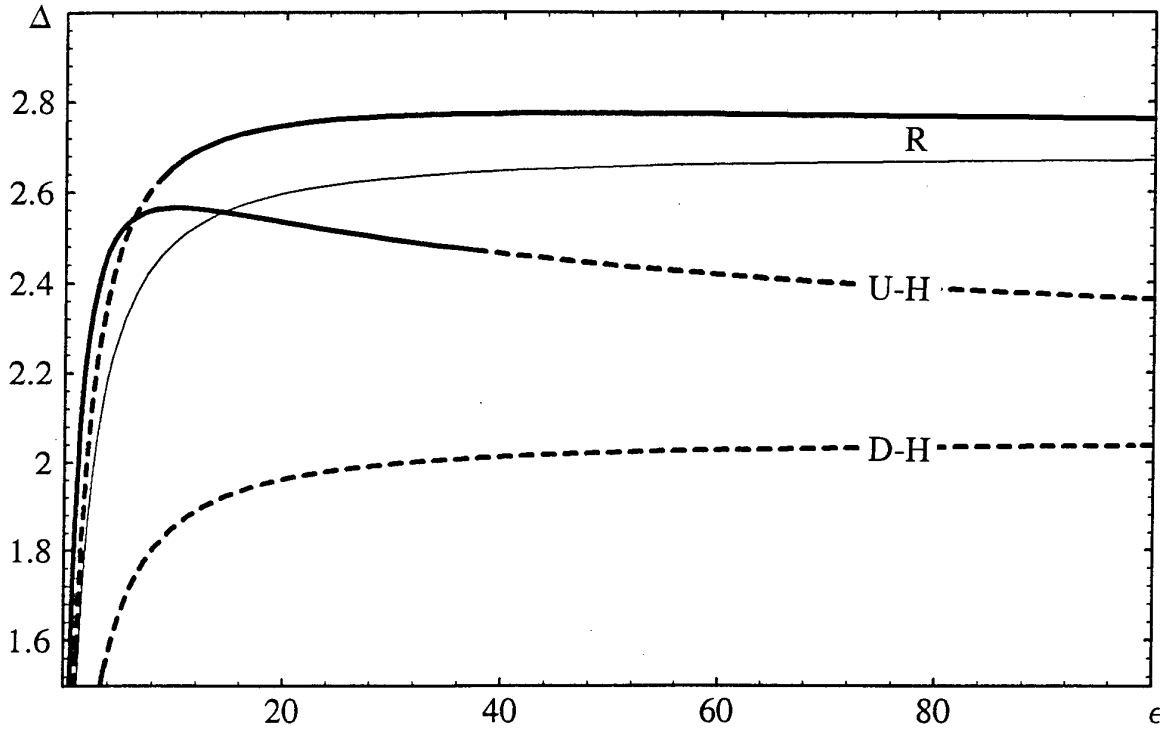


Figure 3.9 : The bulk temperature decrease Δ as a function of the distance to the threshold ϵ for $Bi=0$. R : Rolls, U-H : Up-hexagons, D-H : Down-hexagons. Solid curves represent stable states, while dotted curves represent unstable states. The thin solid line represents the analytical result given by eq. (28) of the text for the bulk temperature decrease of rolls.

Figure 9 represents the bulk temperature decrease Δ as a function of the distance to the threshold ϵ , for solutions (35) to (37). As expected, up-hexagons (upflows at the centre of the hexagons) are the only stable solutions just above the threshold, and rolls become stable only at large ϵ . Down-hexagons (downflow at the centre) are always unstable, because $\delta > 0$ (which is different from the case of very low-Prandtl number fluids [26]). Note that, although not apparent on the figure, the first bifurcation to up-hexagons at $\epsilon=0$ is slightly hysteretic:

the depth of this subcritical region is 3.3% (for $Bi=0$) in our model, slightly larger than the 2.3% value of Scanlon and Segel [14]. This is due to the fact that we have neglected the stabilising action of "secondary" modes, i.e. those generated by quadratic interaction of the "primary" modes. This is done since it is natural to expect that these modes become unimportant for large Ma , as observed in the case of two-dimensional simulations, characterised by a strong domination of the fundamental mode $n=1$ (see section III.3). When the amplitudes of these harmonics are included in eq. (29), and finally eliminated using adiabatic slaving [25-26, 28], the 2.3% value of the hysteresis is recovered. It is also possible to recover the result 0.56% of Bragard and Lebon [24], in the case of a layer of finite depth (the calculation of coefficients is then fully numerical). It is also apparent that the depth of the subcritical region is increasing with the Biot number.

An interesting result of the present analysis is that at large Marangoni numbers, the stability properties are not qualitatively modified with respect to the results of Scanlon and Segel [14]: these authors predict that rolls should become stable above a value $\epsilon_1=64$ (our value is $\epsilon_1=8.6$) of the constraint, while up-hexagons should become unstable above $\epsilon_2=196$ (our value is $\epsilon_2=37$). A bistability region (leading to hysteresis effects between rolls and hexagons) thus exists between ϵ_1 and ϵ_2 . This qualitative concordance reinforces the idea that this hysteresis region could be a physical reality, although the domain of validity of the amplitude equations is not guaranteed for such large values of ϵ . Lastly, we have represented the maximal surface velocity for the bifurcating solutions (35) to (37) in fig.10, showing that this quantity is not strongly dependent on the particular planform selected.

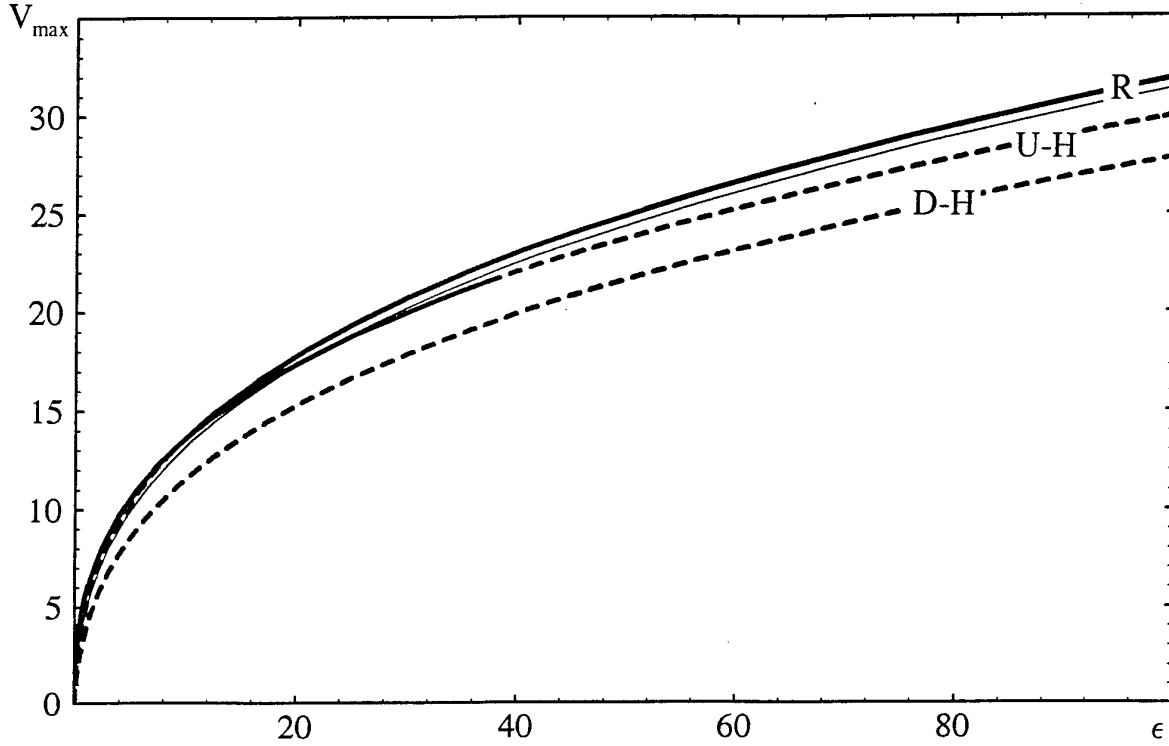


Figure 3.10 : The maximal surface velocity V_{max} as a function of the distance to the threshold ϵ for $Bi=0$. R : Rolls, U-H : Up-hexagons, D-H : Down-hexagons. Solid curves represent stable states, while dotted curves correspond to unstable states. The thin solid line represents the analytical result for the maximal surface velocity of rolls.

iii) Asymptotic behaviours for $Ma \rightarrow \infty$

It results from the examination of the previous figures that the asymptotic behaviour of the relevant convective quantities for $Ma \rightarrow \infty$ obey to different power laws than those generally derived near the threshold by using classical perturbation methods. In particular, a saturation is observed for the bulk temperature decrease Δ (which, as mentioned earlier, can be considered as equivalent to the Nusselt number). The purpose of the following calculations is to derive asymptotic results for Δ , for the maximal surface velocity V_{max} , as well as for the surface temperature deviation ΔT_{surf} , which we define as the difference between maxima and minima of temperature on the free surface.

From the dispersion relation (13), it is straightforward that

$$\sigma_k \rightarrow \left[\frac{kMa}{2} \right]^{\frac{2}{3}} \text{ for } Ma \rightarrow \infty \quad (3.38)$$

The asymptotic value of the amplitude of rolls is derived from eq. (27) :

$$|a_1|^{Rolls} \rightarrow \frac{Ma^{\frac{1}{3}}}{2^{\frac{1}{3}} 3^{\frac{1}{2}} (1+Bi)} \quad (3.39)$$

and it is calculated from eq. (28) that the saturation value of the bulk temperature decrease for a roll structure is

$$\Delta^{Rolls} \rightarrow \frac{8}{3} \approx 2.66 \quad (3.40)$$

independently of the value of the Biot number. This result is confirmed by all the curves of fig. 6.

It is readily computed that the maximal surface velocity is

$$V_{max}^{Rolls} \rightarrow \frac{8 Ma^{\frac{1}{3}}}{2^{\frac{1}{3}} 3^{\frac{1}{2}}} \approx 3.67 Ma^{\frac{1}{3}} \quad (3.41)$$

while the amplitude of the surface temperature variations is given by

$$\Delta T_{surf}^{Rolls} \rightarrow \frac{32 Ma^{-\frac{2}{3}}}{2^{\frac{1}{3}} 3^{\frac{1}{2}}} \approx 14.66 Ma^{-\frac{2}{3}} \quad (3.42)$$

The corresponding expressions for hexagons (although unstable with respect to roll disturbances for $Ma \rightarrow \infty$) can also be derived analytically. We obtain

$$\delta \rightarrow \frac{16}{9} (1+Bi) \quad (3.43)$$

$$\alpha_1 \rightarrow 3 (1+Bi)^2 \quad (3.44)$$

$$\alpha = \alpha_1 + 2\alpha_2 \rightarrow \frac{(104733031 - 60445052\sqrt{3})}{243 (7 + 4\sqrt{3})} (1+Bi)^2 \approx 11.56 (1+Bi)^2 \quad (3.45)$$

It follows that

$$\Delta^{Hexagons} \rightarrow 2.08 \quad (3.46)$$

for the bulk temperature decrease of hexagons (both up and down hexagons lead to the same value for $Ma \rightarrow \infty$, as seen from eqs (36) and (37), and in fig.9). This value is inferior to the value $8/3$ of rolls. However, this should not be taken as a rigorous justification for the instability of hexagons, since it well known that the principle of maximisation of the convective heat transport, originally proposed by Malkus [31], does not lead to stability predictions that are generally valid [32].

Finally, the maximal surface velocity tends to

$$V_{\max}^{\text{Hexagons}} \rightarrow 3.29 Ma^{\frac{1}{3}} \quad (3.47)$$

and the amplitude of the surface temperature deviations is

$$\Delta T_{\text{surf}}^{\text{Hexagons}} \rightarrow 16.81 Ma^{-\frac{2}{3}} \quad (3.48)$$

To check the assumptions used in our analysis, it should be interesting to compare the above results with a full numerical integration of the problem. Preliminary finite differences simulations indicate a slow growth of the bulk temperature decrease, as well as an increase of the velocities (although with an exponent larger than $1/3$) coexistent with a slow decrease of the surface temperature variations. This allows us to place some confidence in our analysis. In particular, the exponents $1/3$ and $-2/3$ may be considered as first approximations, that could be refined by deriving higher order contributions to the amplitude equations. It appears also that the present asymptotic analysis leads to results that are difficult to check by finite differences simulations. Indeed, since convergence of results may only be expected for very high values of the Marangoni number, numerical difficulties are encountered, mainly due to the presence of very steep surface temperature gradients at the cold points, where the fluid moves downwards.

We conclude this section by remarking about an important mathematical aspect of the pure Marangoni-Bénard instability. A particular feature of this problem is that the neutral stability condition provides Ma as a single-valued function of the wavenumber k . This means that above the corresponding critical value, one and only one eigenmode is unstable, whatever large is the value of Ma . This has to be contrasted [33] with Rayleigh-Bénard instabilities, where n eigenmodes are linearly unstable above the value $Ra_n = (k^2 + n^2\pi^2)^3/k^2$ of the Rayleigh number (case of pure Rayleigh-Bénard convection between stress-free boundaries). Clearly, the above analysis would require non-trivial modifications to account for interactions between these unstable vertical modes. Physically, this difference between Marangoni-Bénard and Rayleigh-Bénard problems is certainly related to the different natures of the surface and the bulk forces. This could also explain why neither boundary layer instabilities, nor subsequent transitions to turbulence have been observed in our model, in the range of Marangoni numbers investigated.

III.5. Conclusions of section III

Pure thermocapillary instability in layers with non-deformable interface and infinite Prandtl number has been studied. The model is based on the assumptions that the dynamics is determined by the interactions of the unstable eigenmodes of the linear stability problem, and that the evolution equations describing their interactions can be limited to third order in their amplitudes. Although strictly valid near the threshold, this model has to be considered as an approximation (similar to a truncated modified Galerkin method) far from it. Attention has been restricted to short-wave effects, so that the layer has been assumed infinitely deep.

The first part of the analysis has focused on the two-dimensional wavelength selection problem at moderately large Marangoni numbers, for which the wavelength of the fastest growing disturbance is much smaller than the critical wavelength. The transient numerical integration of third order amplitude equations has shown that, although a structure dominated by the fastest growing disturbance can appear at a given instant, it is progressively replaced by larger wavelength structures. A steady state is always reached, whose wavelength is equal to the size of the (periodic) simulation domain. This is confirmed by a finite difference integration of the problem. Although the fastest growing wavelength is a finite quantity, it appears that the Marangoni-Bénard instability cannot induce stable localised structures with intrinsic wavelengths independent of the experiment dimensions (at least up to $Ma=4000$). The physical mechanism responsible for this convective cells growth process is shown to be related to the nonlinear convective heat transport, which creates a distortion of the temperature field in the region located near the free surface. The distortion of the horizontally averaged temperature profile (the cause of the instability) has a stabilising effect on short wavelength modes, but leaves the growth rate of large wavelength structures relatively unchanged. This produces a growth of the pattern wavelength, which presents some resemblance with experimental results of Linde [5], although we have not studied this point in details, since transient evolution of the diffusive (boundary layer) profile is not taken into account in our analysis.

Properties of the steady states observed in the convective system have been investigated for both rolls and hexagonal structures. Contrary to existing weakly nonlinear theories, our method (differing by the use of eigenfunctions, rather than neutral stability functions) appears to lead to physically realistic results, at least qualitative, for very large Marangoni numbers. This is conjectured from examination of the behaviour of some relevant convective quantities. The decrease of the bulk temperature due to Marangoni convection has been found to present a saturation when the Marangoni number is increased (while the weakly nonlinear result is a linear growth). The velocities are found to grow as $Ma^{1/3}$ as $Ma \rightarrow \infty$, while the surface temperature variations decrease as $Ma^{-2/3}$. However, due to the assumptions underlying our model, these behaviours should be considered as first approximations, that could be refined by including higher order interactions in the amplitude equations. The analysis of the competition between rolls and hexagons confirms earlier results [14, 23-26], quantitatively (near threshold) and qualitatively (far from threshold). At small Marangoni numbers, up-hexagons are the only stable solutions (the first bifurcation is slightly hysteretic), while rolls are the only stable solutions at very large Marangoni numbers. Down-hexagons are always unstable ($Pr \rightarrow \infty$). The transition between up-hexagons and rolls is found to be hysteretic, as in other problems (f.ex. [34]). However, this transition has been found to occur for lower Marangoni numbers than in [14], and with a smaller hysteresis loop.

Appendix 1 : Derivation of amplitude equations

Using eq. (11), we may write eq. (10) as a differential problem for $U_k^D(z, t)$:

$$\begin{aligned} \mathcal{L}_{\bar{k}}(U_{\bar{k}}^D) - Ma M_{\bar{k}}(U_{\bar{k}}^D) = & -A_{\bar{k}}(\mathcal{L}_{\bar{k}}(U_{\bar{k}}^\sigma) - Ma M_{\bar{k}}(U_{\bar{k}}^\sigma)) + \frac{\partial A_{\bar{k}}}{\partial t} \Theta_{\bar{k}}(U_{\bar{k}}^\sigma) \\ & + \int d\bar{k}' A_{\bar{k}'} A_{\bar{k}-\bar{k}'} N_{\bar{k}', \bar{k}-\bar{k}'}^\sigma(U_{\bar{k}'}^\sigma, U_{\bar{k}-\bar{k}'}^\sigma) + \int d\bar{k}' N_{\bar{k}', \bar{k}-\bar{k}'}^\sigma(U_{\bar{k}'}^D, U_{\bar{k}-\bar{k}'}^D) \\ & + \int d\bar{k}' A_{\bar{k}'} (N_{\bar{k}', \bar{k}-\bar{k}'}^\sigma(U_{\bar{k}'}^\sigma, U_{\bar{k}-\bar{k}'}^D) + N_{\bar{k}-\bar{k}', \bar{k}'}^\sigma(U_{\bar{k}-\bar{k}'}^D, U_{\bar{k}'}^\sigma)) \end{aligned} \quad (\text{A.1})$$

where the time-derivative of $U_{\bar{k}}^D$ has been cancelled, as a result of our assumption to neglect the own dynamics of the damped modes (slaving principle). Note that because of eq. (11), the boundary conditions can only be satisfied if $U_{\bar{k}}^D$ belongs to E . A very rough (and insufficient) model could be obtained at this stage by projection of eq. (A.1) on some functions (generally the adjoint functions [35]), and assuming $U_{\bar{k}}^D = 0$. We would then obtain an equation of the form (16), but without stabilising cubic terms. Rather, we will try to solve (A.1) for $U_{\bar{k}}^D$. This can be done only if (A.1) is compatible, which is not the case at $Ma = Ma_k$ (the kernel of the left hand side operator is then not empty), except if the second member is orthogonal to the solution of the adjoint neutral stability problem (Fredholm's condition). This leads to the amplitude equations

$$\begin{aligned} \frac{\partial A_{\bar{k}}}{\partial t} = & \sigma_k A_{\bar{k}} + \int d\bar{k}' Z_{\bar{k}', \bar{k}} A_{\bar{k}'} A_{\bar{k}-\bar{k}'} \\ & - \int d\bar{k}' A_{\bar{k}'} \frac{\langle V_{\bar{k}}^*, N_{\bar{k}', \bar{k}-\bar{k}'}^\sigma(U_{\bar{k}'}^\sigma, U_{\bar{k}-\bar{k}'}^D) \rangle}{\tau_k} \end{aligned} \quad (\text{A.2})$$

where eq. (12) has been used, and it has been anticipated that the velocity (and pressure) components of $U_{\bar{k}}^D$ are zero. This will become apparent later, and is a consequence of the linearity of the equations of motion. In (A.2), $\langle V_{\bar{k}}^*, \cdot \rangle$ denotes the projection on the adjoint neutral stability solution (derived in appendix 2), $\tau_k = \langle V_{\bar{k}}^*, \Theta_{\bar{k}}(U_{\bar{k}}^\sigma) \rangle$ is the normalisation factor, and the quadratic coefficients are given by

$$Z_{\bar{k}', \bar{k}} = - \frac{\langle V_{\bar{k}}^*, N_{\bar{k}', \bar{k}-\bar{k}'}^\sigma(U_{\bar{k}'}^\sigma, U_{\bar{k}-\bar{k}'}^\sigma) \rangle}{\tau_k} \quad (\text{A.3})$$

Now, by inserting the projected part (A.2) into the complete equation (A.1), we obtain

$$\begin{aligned} \mathcal{L}_{\bar{k}}(U_{\bar{k}}^D) - Ma M_{\bar{k}}(U_{\bar{k}}^D) = & \int d\bar{k}' A_{\bar{k}'} A_{\bar{k}-\bar{k}'} N_{\bar{k}', \bar{k}-\bar{k}'}^{NR}(U_{\bar{k}'}^\sigma, U_{\bar{k}-\bar{k}'}^\sigma) \\ & + \int d\bar{k}' A_{\bar{k}'} N_{\bar{k}', \bar{k}-\bar{k}'}^{NR}(U_{\bar{k}'}^\sigma, U_{\bar{k}-\bar{k}'}^D) \end{aligned} \quad (\text{A.4})$$

where the "Non-Resonant" part of a term X is defined by $X^{NR} = X - \tau_k^{-1} \langle V_{\bar{k}}^*, X \rangle \Theta_{\bar{k}}(U_{\bar{k}}^\sigma)$, such that $\langle V_{\bar{k}}^*, X^{NR} \rangle = 0$ for every X . This ensures that (A.4) is compatible for every Ma .

Now, the form of equation (A.4) suggests an iterative series solution, starting with

$$U_{\bar{k}}^D = \int d\bar{k}' A_{\bar{k}'} A_{\bar{k}-\bar{k}'} U_{\bar{k}\bar{k}'}^D \quad (\text{A.5})$$

in which $U_{\bar{k}\bar{k}'}^D$ is obtained from

$$(\mathcal{L}_{\bar{k}} - Ma M_{\bar{k}}) U_{\bar{k}\bar{k}'}^D = N_{\bar{k}', \bar{k}-\bar{k}'}^{NR} (U_{\bar{k}'}^\sigma, U_{\bar{k}-\bar{k}'}^\sigma) \quad (\text{A.6})$$

Substituting this result in the r-h-s of (A.4) leads to higher order corrections (cubic terms for $U_{\bar{k}}^D$, generating quartic and higher order terms in (A.2), which are not considered in our model). We limit the calculation of $U_{\bar{k}}^D$ to (A.5) and (A.6), such that the compatibility equations (A.2) reduce to the amplitude equations (16), with quadratic coefficients given by (A.3) and cubic coefficients given by

$$Z_{\bar{k}' \bar{k}'' \bar{k}} = - \frac{\langle V_{\bar{k}}^*, N_{\bar{k}', \bar{k}-\bar{k}'} (U_{\bar{k}'}^\sigma, U_{\bar{k}-\bar{k}'}^D, \bar{k}'') \rangle}{\tau_k} \quad (\text{A.7})$$

Appendix 2 : Solution of the linear problem

Starting from eq. (12), the neutral stability problem ($\sigma_k=0$) can be written as

$$S_{\bar{k}}(U_{\bar{k}}^0) = \mathcal{L}_{\bar{k}}(U_{\bar{k}}^0) - Ma_k M_{\bar{k}}(U_{\bar{k}}^0) = \begin{bmatrix} (D^2 - k^2) \bar{V}_{r\bar{k}}^0 - i \bar{k} p_k^0 \\ (D^2 - k^2) W_k^0 - D p_k^0 \\ D W_k^0 + i \bar{k} \cdot \bar{V}_{r\bar{k}}^0 \\ (D^2 - k^2) T_k^0 + W_k^0 \\ [D \bar{V}_{r\bar{k}}^0 + i \bar{k} Ma_k T_k^0]_{z=0} \end{bmatrix} = 0 \quad (\text{A.8})$$

The solution of this problem which belongs to E (i.e. which satisfies boundary conditions (2) and (3)) reads

$$U_{\bar{k}}^0 = \begin{bmatrix} \bar{V}_{r\bar{k}}^0 \\ W_k^0 \\ p_k^0 \\ T_k^0 \end{bmatrix} = e^{kz} \begin{bmatrix} -4 i \bar{k} (k+Bi) (1+kz) \\ -4 k^2 (k+Bi) z \\ -8 k^2 (k+Bi) \\ 1 - (k+Bi) z + k (k+Bi) z^2 \end{bmatrix} \quad (\text{A.9})$$

where $k = |\bar{k}|$, and the normalisation condition has been chosen such that $T_k^0(z=0) = 1$. The compatibility condition leads to the neutral stability relation $Ma_k = 8 k (k+Bi)$.

We can now define adjoint vectors

$$V^* = \begin{bmatrix} \bar{V}_r^* \\ W^* \\ p^* \\ T^* \\ \bar{X}^* \end{bmatrix} \quad (\text{A.10})$$

belonging to a set E^* of adjoint boundary conditions to be defined later on.

A scalar product is introduced in the usual way (f.ex. [14,24]) by

$$\langle V^*, S_{\bar{k}}(U) \rangle = \int_{-\infty}^0 [\bar{V}_r^* \cdot \bar{S}_1 + \bar{W}^* S_2 + \bar{p}^* S_3 + \bar{T}^* S_4] dz + [\bar{X}^* \cdot \bar{S}_5]_{z=0} \quad (\text{A.11})$$

where S_i $i=1, \dots, 5$ are the components of (A.8), and the overbar denotes the complex conjugate. We also define the adjoint operator $S_{\bar{k}}^*$ of $S_{\bar{k}}$ by

$$\langle V^*, S_{\bar{k}}(U) \rangle = \langle S_{\bar{k}}^*(V^*), U \rangle \quad (\text{A.12})$$

for all U belonging to E and V^* to E^* . Integration by parts leads to

$$S_{\bar{k}}^*(V^*) = \begin{bmatrix} (D^2 - k^2) \bar{V}_r^* - i \bar{k} p^* \\ (D^2 - k^2) W^* - D p^* + T^* \\ D W^* + i \bar{k} \cdot \bar{V}_r^* \\ (D^2 - k^2) T^* \end{bmatrix} \quad (\text{A.13})$$

and the cancellation of the boundary term gives E^* as the set of sufficiently derivable functions satisfying

$$\bar{V}_r^*, W^*, D T^*, p^* \rightarrow 0 \quad \text{for } z \rightarrow -\infty \quad (\text{A.14})$$

$$W^* = D \bar{V}_r^* = \bar{X}^* + \bar{V}_r^* = D T^* + B i T^* + i M a_k \bar{k} \cdot \bar{X}^* = 0 \quad \text{for } z = 0 \quad (\text{A.15})$$

The resolution of the adjoint problem $S_{\bar{k}}^*(V_{\bar{k}}^*) = 0$ (with $V_{\bar{k}}^* \in E^*$) gives

$$V_{\bar{k}}^* = \frac{-k e^{kz}}{4(2k + B i)} \begin{bmatrix} i \bar{k} k^{-2} (1 - kz - k^2 z^2) \\ z(1 - kz) \\ -4(1 + kz) \\ -8k \\ -i \bar{k} k^{-2} \end{bmatrix} \quad (\text{A.16})$$

where the normalisation $\langle \bar{V}_{\bar{k}}^*, \Theta_{\bar{k}}(U_{\bar{k}}^0) \rangle = 1$ has been adopted.

Finally, the eigenfunctions of the spectral problem (12) read

$$U_{\vec{k}}^{\sigma} = \begin{bmatrix} \bar{V}_{r\vec{k}}^{\sigma} \\ W_{\vec{k}}^{\sigma} \\ p_{\vec{k}}^{\sigma} \\ T_{\vec{k}}^{\sigma} \end{bmatrix} = -4k^2(k+Bi) \begin{bmatrix} i\bar{k}k^{-2}e^{kz}(1+kz) \\ ze^{kz} \\ 2e^{kz} \\ e^{kz}(2\frac{k}{\sigma^2} + \frac{z}{\sigma}) - 2ke^{(\sigma+k^2)^{1/2}z}(\frac{1}{k^2Ma} + \frac{1}{\sigma^2}) \end{bmatrix} \quad (\text{A.17})$$

where the corresponding eigenvalue σ is solution of the dispersion relation (13). Note that the derivation of (A.17) assumes $\sigma+k^2 > 0$ (which is verified provided that $k < Ma/2 Bi$, as seen from eq. (13)). Otherwise, when $\sigma+k^2 < 0$, imaginary roots are obtained from the characteristic relation, and lead to a continuum of solutions bounded at $z \rightarrow -\infty$, but which do not satisfy boundary conditions (2).

Appendix 3 : Calculation of the mean temperature profile

For the roll mode $A_{\vec{k}} = a_1(t)\delta(\vec{k} - \vec{k}_0) + \bar{a}_1(t)\delta(\vec{k} + \vec{k}_0)$ (see end of section III.3), the $k=0$ Fourier component of the perturbation vector is found from (A.5) as

$$U_{k=0}^D = 2|a_1|^2 U_{01}^D(z) \quad (\text{A.18})$$

where, according to (A.6), $U_{01}^D(z)$ is the solution of the inhomogeneous problem

$$\mathcal{L}_0(U_{01}^D) = N_{1,-1}(U_1^0, U_{-1}^0) \quad (\text{A.19})$$

since $M_{k=0}=0$, and the resonant part of $N_{1,-1}$ is zero, as $Z_{10}=0$ from (A.3). Here again, the subscripts refer to the mode number (1 for \vec{k}_0 , -1 for $-\vec{k}_0$). It is computed that the only non-zero component of $U_{01}^D(z)$ is $T_{01}^D(z)$, solution of

$$D^2 T_{01}^D = W_1^0 D T_{-1}^0 + \bar{V}_{r1}^0 \cdot -i\bar{k}_0 T_{-1}^0 = D(W_1^0 T_1^0) \quad (\text{A.19})$$

where the neutral stability functions are given by (A.9). Then, the solution belonging to E is

$$T_{01}^D = (5Bi^2 + 12k_0 Bi + 7k_0^2)(e^{2k_0 z}(\frac{1}{2k_0} - z) - \frac{1}{2k_0}) + (Bi+k_0)^2 k_0 e^{2k_0 z} z^2 (5 - 2k_0 z) \quad (\text{A.20})$$

The cubic coefficient Z_{111}^0 can then be computed from (A.7) as

$$Z_{111}^0 = -\langle V_1^*, N_{1,0}(U_1^0, U_{01}^D) \rangle = -\int_{-\infty}^0 T_1^* (W_1^0)^2 T_1^0 dz = -\frac{k_0^2 (Bi+k_0)^2 (3Bi+5k_0)}{2(Bi+2k_0)} \quad (\text{A.21})$$

A slightly longer but similar computation leads to the expression of the second cubic coefficient Z_{-111}^0 , and then finally to eq. (20). Equation (27) is also obtained in this way, but by using eigenfunctions (A.17) instead of the neutral stability functions (A.9).

III.6. References of section III

1. F. Preisser, D. Schwabe and A. Scharmann, "Steady and oscillatory thermocapillary convection in liquid columns with free cylindrical surface", *J. Fluid Mech.* 126, 1983, pp. 545-567.
2. Y. Kamotani, J. H. Lee, S. Ostrach and A. Pline, "An experimental study of oscillatory thermocapillary convection in cylindrical containers", *Phys. Fluids A* 4 (5), May 1992, pp. 955-962.
3. H. Bénard, "Les tourbillons cellulaires dans une nappe liquide", *Rev. Gen. des Sci. Pures et Appl.*, 11, 1900.
4. M. J. Block, "Surface tension as the cause of Bénard cells and surface deformation in a liquid film", *Nature* 178, 1956, pp. 650-651.
5. H. Linde, P. Schwartz and H. Wilke, "Dissipative structures and nonlinear kinetics of the Marangoni instability", in *Dynamics and Instability of Fluid Interfaces*, Ed. T.S. Sorensen, Springer Verlag 1979, pp. 75-119.
6. P. D. Weidman, H. Linde, and M. G. Velarde, "Evidence for solitary wave behaviour in Marangoni-Bénard convection", *Phys. Fluids A* 4 (5), May 1992, pp. 921-926.
7. C. V. Sternling and L. E. Scriven, "Interfacial turbulence : hydrodynamic instability and the Marangoni effect", *A.I.Ch.E. J.* Dec. 1959, pp. 514-523.
8. E. L. Koschmieder and M. I. Biggerstaff, "Onset of surface-tension-driven Bénard convection", *J. Fluid Mech.* 167, 1986, pp. 49-64.
9. P. Cerisier, C. Jamond, J. Pantaloni and C. Perez-Garcia, "Stability of roll and hexagonal patterns in Bénard-Marangoni convection", *Phys. Fluids* 30, 4, April 1987, pp. 954-959.
10. J. K. Platten and J. C. Legros, "Convection in liquids", Springer-Verlag, 1984.
11. Ch. Normand, Y. Pomeau and M. G. Velarde, "Convective instability : a physicist's approach", *Rev. Mod. Phys.* 49, 3, 1977, pp. 581-624.
12. J. Pantaloni, R. Bailleux, J. Salan, M. G. Velarde, "Rayleigh-Bénard-Marangoni instability : new experimental results", *J. Non-Equilib. Thermodyn.* 4, 1979, pp. 201-218.
13. J. R. A. Pearson, "On convection cells induced by surface tension", *J. Fluid Mech.* 4, 1958, pp. 489-500.
14. J.W. Scanlon and L.A. Segel, "Finite amplitude cellular convection induced by surface tension", *J. Fluid Mech.* 30, 1967, pp. 149-162.
15. M. Bestehorn, "Phase and amplitude instabilities for Bénard-Marangoni convection in fluid layers with large aspect ratio", *Phys. Rev. E*, 48, 5, 1993, pp. 3622-3634.
16. M.C. Cross and P.C. Hohenberg, "Pattern formation outside of equilibrium", *Rev. Mod. Phys.*, 65, n°3, 1993, pp. 851-1112.
17. G. Dewel, P. Borckmans, A. De Wit, B. Rudovics, J.-J. Perraud, E. Dulos, J. Boissonade, P. De Kepper, "Pattern selection and localised structures in reaction-diffusion systems", *Physica A* 213, 1995, pp. 181-198.
18. S. Chandrasekhar, "Hydrodynamic and hydromagnetic stability", Clarendon, Oxford, 1961.
19. M. Fermigier, P. Jenffer, L. Limat and J.E. Wesfreid, "Fluid-fluid interfacial instabilities induced by gravity", *ESA SP-333, Proc. VIIIth European Symposium on Materials and Fluid Sciences in Microgravity*, Brussels, Belgium, 1992.
20. F. H. Busse, "Non-linear properties of thermal convection", *Rep. Prog. Phys.* 41,

- 1978, pp. 1929-1967.
21. D.A. Goussis and R. E. Kelly, "On the thermocapillary instabilities in a liquid layer heated from below", *Int. J. Heat Mass Transfer*, 33, 10, 1990, pp. 2237-2245.
22. A.A. Golovin, A.A. Nepomnyashchy and L. M. Pismen, "Interaction between short-scale Marangoni convection and long-scale deformational instability", *Phys. Fluids* 6, 1, Jan. 1994, pp. 34-48.
23. A. Clout and G. Lebon, "A nonlinear stability analysis of the Bénard-Marangoni problem", *J. Fluid Mech.* 145, 1984, pp. 447-469.
24. J. Bragard and G. Lebon, "Nonlinear Marangoni convection in a layer of finite depth", *Europhys. Lett.* 21, 8, pp. 831-836, 1993.
25. S. Rosenblat, G. M. Homsy and S. H. Davis, "Nonlinear Marangoni convection in bounded layers. Part 1. Circular cylindrical containers. Part 2. Rectangular cylindrical containers", *J. Fluid Mech.* 120, 1982, pp. 91-122 & 123-138.
26. P. C. Dauby, G. Lebon, P. Colinet and J. C. Legros, "Hexagonal Marangoni convection in a rectangular box with slippery sidewalls", *Q. J. Mech. Appl. Math.* 46, 1993, pp. 683-707.
27. A. Vidal and A. Acrivos, "Nature of the neutral state in surface-tension driven convection", *Phys. Fluids* 9, 3, 1966, pp. 615-616.
28. P. Manneville, "Structures dissipatives, chaos et turbulence", Aléa-Saclay, 1991.
29. C.A. Jones and M.R.E. Proctor, "Strong spatial resonance and travelling waves in Bénard convection", *Phys. Lett. A* 121, 5, 1987, pp. 224-228.
30. M.R.E. Proctor and C.A. Jones, "The interaction of two spatially resonant patterns in thermal convection. Part 1. Exact 1:2 resonance", *J. Fluid Mech.* 188, 301, 1988.
31. W.V.R. Malkus, "The heat transport and spectrum of thermal turbulence", *Proc. Roy. Soc. , London*, A225, 196-212, 1954.
32. F.H. Busse, "Fundamentals of thermal convection", in "Mantle convection, Plate Tectonics and Global Dynamics", W.R. Peltier ed., Gordon and Breach, 1989.
33. S. Rosenblat, G.M. Homsy and S. H. Davis, "Eigenvalues of the Rayleigh-Bénard and Marangoni problems", *Phys. Fluids* 24 (11), nov. 1981.
34. Ch. Karcher and U. Müller, "Convection in a porous medium with solidification", in press in *Fluid Dynamics Research*.
35. W. Eckhaus, "Studies in non-linear stability theory", New-York, Springer, 1965.
36. R. Lefever and D. Carati, "Intrinsic patterns in anisotropic multicomponent diffusive systems at equilibrium", *Physica A* 213, 1995, pp. 90-104.
37. L. M. Pismen and A. A. Nepomnyashchy, "Structure of dislocations in the hexagonal pattern", *Europhys. Lett.* 24, 6, 1993, pp. 461-465.

IV. NUMERICAL RESULTS

IV.1. Description of the method

In this section, a full numerical simulation of the nonlinear equations is presented. Details on the method are reported in [1], such that we only present here the principles of the numerical scheme. The two-dimensional geometry used for calculations is represented on figure 1. We will assume insulating and "slippery" lateral walls at $x=0$ and $x=L$ (where L is the aspect ratio of the container), which have already been used to model real rigid walls [2]. This is equivalent to the periodic boundary conditions used in section III. Here, we will consider a bottom plate at $z=0$, which is rigid and heat conducting. The free surface at $z=1$ is assumed undeformable and insulating ($Bi=0$).

The liquid layer is submitted to a linear temperature profile, and the evolution of perturbations of this reference state is studied. The dimensionless equations we consider are

$$\bar{\nabla} \cdot \bar{V} = 0 \quad (4.1)$$

$$\frac{D\bar{V}}{Dt} = Pr(\Delta \bar{V} - \bar{\nabla} p + Ra T \mathbf{1}_z) \quad (4.2)$$

$$\frac{DT}{Dt} = \Delta T + \bar{V} \cdot \mathbf{1}_z \quad (4.3)$$

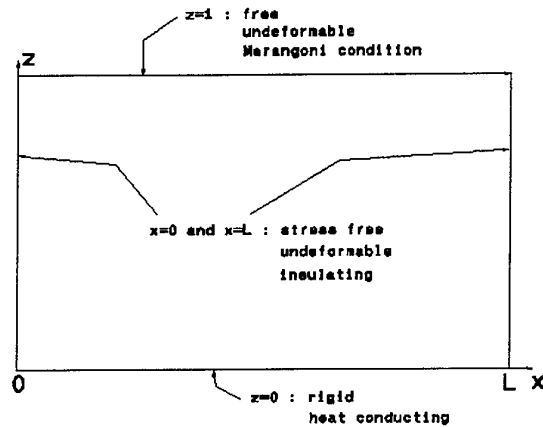


Figure 4.1 : Geometry of the studied system.

where D/Dt is the convective derivative $D/Dt = \partial/\partial t + (\bar{V} \cdot \bar{\nabla})$ and $\bar{V} = (U, W)$, T and p are respectively the deviations of velocity, temperature and hydrodynamic pressure around the mechanical equilibrium state (see section II). A thermal time scale h^2/κ is used as in the previous sections (h is the depth of the liquid layer).

Note that the Rayleigh effect, i.e. the buoyancy forces induced by density variations with temperature, have been included as the last term of eq. (4.2). The dimensionless number quantifying the importance of these forces on the stability of the diffusive state is the Rayleigh number $Ra = g\alpha\beta h^4/\nu\kappa$ (g is the gravity acceleration, α the thermal expansion coefficient, β the imposed thermal gradient, ν the kinematic viscosity and κ the thermal diffusivity).

The boundary conditions are derived from figure 1 :

$$W = \partial W/\partial z = T = 0 \quad \text{at } z=0 \quad (4.4)$$

$$W = \partial T/\partial z = 0 \quad (4.5)$$

$$\partial^2 W/\partial z^2 - Ma \partial^2 T/\partial x^2 = 0 \quad \text{at } z=1$$

$$U = \partial T/\partial x = 0 \quad \text{at } x=0, L \quad (4.6)$$

where the usual notations are used.

The Galerkin method consists in first expanding the unknown quantities in series of functions of x and z with time-dependent coefficients :

$$\begin{aligned} W(x,z,t) &= \sum_{m,n} A_{mn}(t) w_{mn}(x,z) \\ T(x,z,t) &= \sum_{m,n} B_{mn}(t) \theta_{mn}(x,z) \end{aligned} \quad (4.7)$$

We choose the basis functions w_{mn} and θ_{mn} in order to satisfy the boundary conditions (4-6). Then the developments are introduced in equations 2 and 3, which are then projected on the basis functions. The discretisation of the problem is accomplished by truncating the expansions (7) to a finite number of terms. The obtained system is of the following form

$$\begin{aligned} \frac{dA_{mn}}{dt} &= F_{1mn}(A_{ij}, B_{ij}) \\ \frac{dB_{mn}}{dt} &= F_{2mn}(A_{ij}, B_{ij}) \end{aligned} \quad (4.8)$$

and is well suited for computer resolution. The choice of w_{mn} and θ_{mn} is detailed in [1]. We just mention here that trigonometrical functions are used for the horizontal dependency : i.e. $w_{mn} = \cos(mk_0 x) W_n(z)$, $\theta_{mn} = \cos(mk_0 x) T_n(z)$, which satisfies lateral (periodic) boundary conditions at $x=0$ and $x=L=\pi/k_0$. The choice of vertical functions is more delicate, due to the complexity of boundary conditions at $z=0$ and $z=1$. The computer simulation uses a Runge-Kutta method of order 4, with adaptative stepsize control for numerical integration given some initial conditions $A_{mn}(0)$, $B_{mn}(0)$. We always chosen infinitesimal "white noise" $A_{mn}(0) = B_{mn}(0) = 10^{-6}$.

IV.2. Finite-amplitude regimes of convection - behaviour at large Ma

The following figures represent convective states obtained for various values of the Marangoni number Ma, the Rayleigh number Ra being in all cases equal to zero. We have considered four different values of the aspect ratio L of the box : 1.57, 0.785, 0.628 and 0.524. As the lateral walls can be considered as periodic boundary conditions, these aspect ratios correspond respectively to values 2, 4, 5 and 6 of the wavenumber k_0 of the convective field (since one convective cell corresponds to one half of the period, the aspect ratio L and the wavenumber k_0 are related by $k_0 = \pi/L$).

For large values of the wavenumber k_0 (small values of L), the convection cells are more concentrated near the interface, and consequently do not feel the presence of the lower rigid plate. Thus, for $k_0 \rightarrow \infty$, the results obtained here should tend to the results obtained in the last section III, where the liquid layer was assumed infinitely deep (short wave effects). This provides a way to test the assumptions used in section III, which allowed to obtain analytical results. This will be done in section IV.3.

For each simulation, the following data (steady state) are presented :

- the streamline pattern (top left figure, the direction of circulation is clockwise)
- the isotherms (top right figure, on which the dark zones indicate cold regions, while the

white zones indicate hot regions)

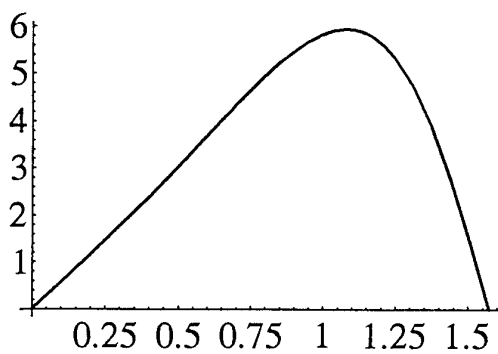
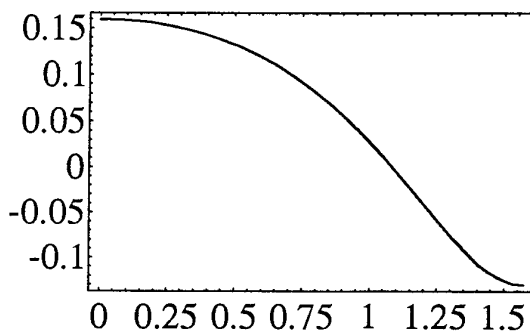
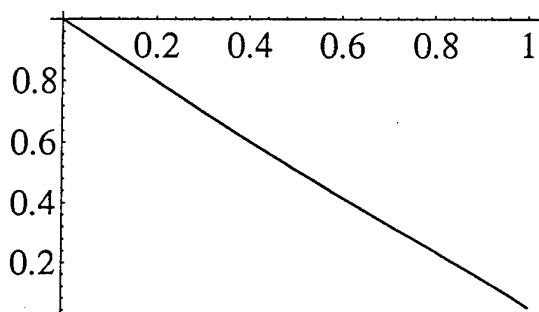
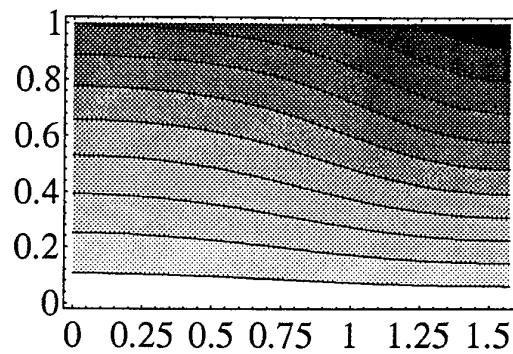
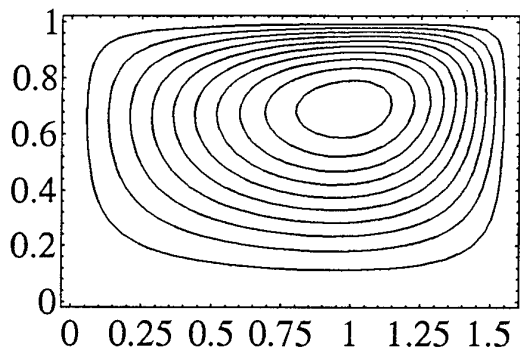
- the mean temperature profile, i.e. the temperature field averaged over one horizontal period (middle left figure, where the abscissa is the vertical coordinate z , and the ordinate is the mean temperature)
- the free surface temperature as a function of the horizontal coordinate x (middle right)
- the free surface horizontal velocity as a function of the horizontal coordinate x (bottom left)

For each figure, numerical values of typical convective quantities are also presented : these are

- the increase of the mean surface temperature (averaged in the horizontal direction) due to convection. This convective quantity, denoted as **delta**, is a measure of the increase of the heat transport created by convection, as remarked in section III. For $k_0 \rightarrow \infty$, it should correspond to the value of the bulk temperature decrease Δ of section III (see IV.3).
- the amplitude of the surface temperature variations (denoted by **delta T**), defined as the difference between temperature maxima and minima on the free surface. For $k_0 \rightarrow \infty$, it should correspond to the value of ΔT_{surf} of the section III.
- the value of the maximal surface velocity **Vmax**, together with the horizontal position x of this maximum. Again, for $k_0 \rightarrow \infty$, it should correspond with values of V_{max} computed in section III.

Also given on each figure are the Marangoni number Ma , the value of the wavenumber k_0 , the number N_{max} of vertical functions, and the number I_{max} of horizontal trigonometric functions in the Galerkin expansions (4.7).

For each value of k_0 , the Marangoni number is increased step by step until the point where numerical divergences occur. These divergences, due to the insufficient number of trial functions in the Galerkin expansion, manifest first in the curve of the free surface velocity (bottom left). This will also be apparent on the curves of the free surface maximal velocity presented in the section IV.3. However, some of these slightly diverged simulations are presented here, and it will be seen in the next section that the values obtained for other convective quantities may still be considered as satisfactory.



Ma=100

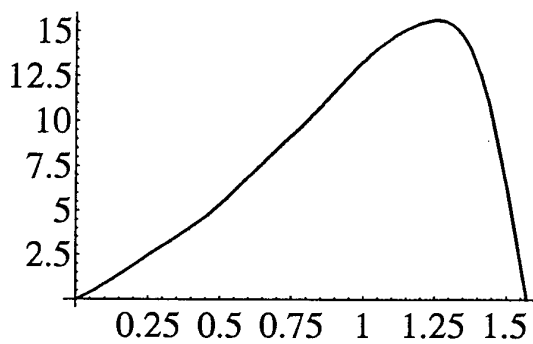
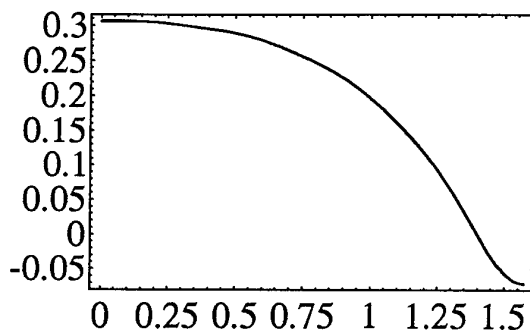
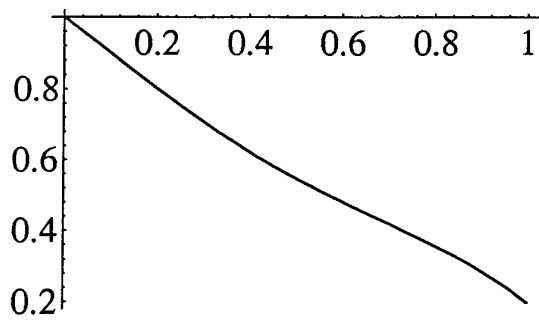
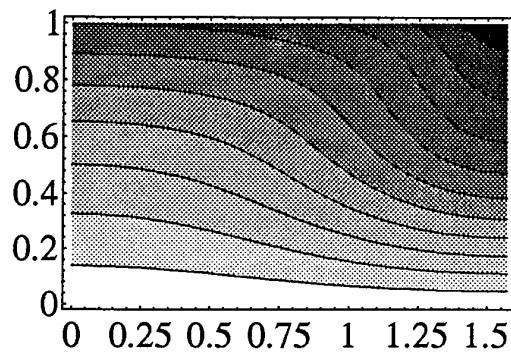
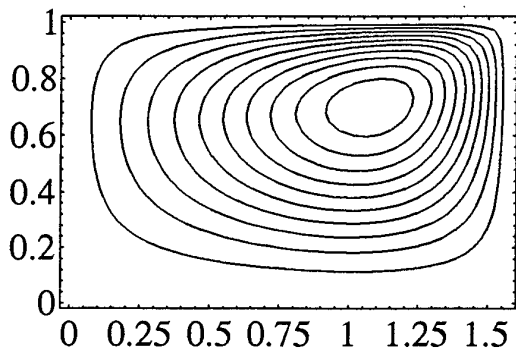
k0=2

Nmax=8 Imax=8

delta=0.0521143

delta T=0.289756

Vmax=5.9312 at x=1.07932



$Ma=200$

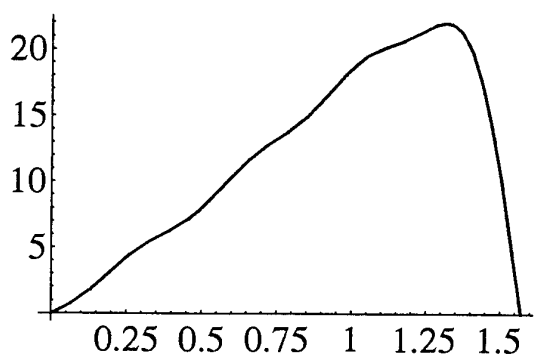
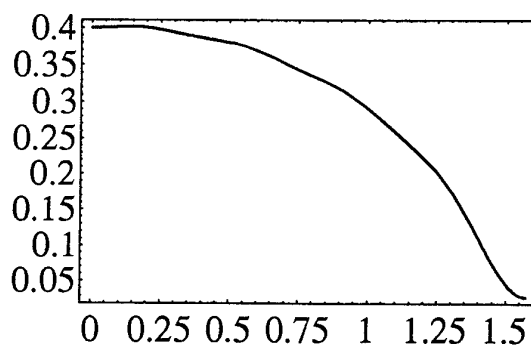
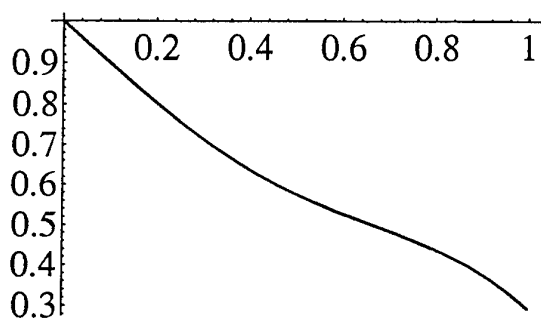
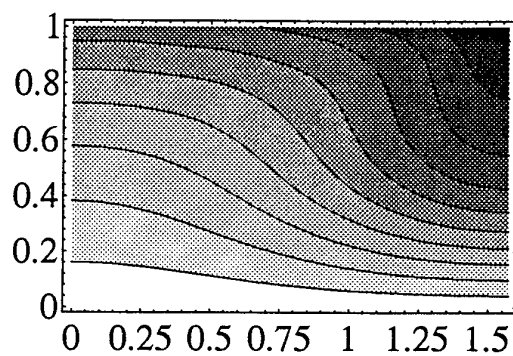
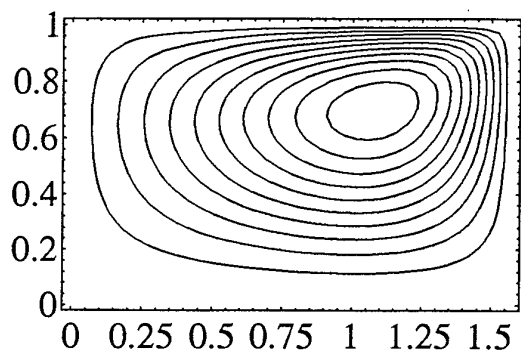
$k_0=2$

$N_{max}=8$ $I_{max}=8$

$\delta=0.198972$

$\delta T=0.376869$

$V_{max}=15.5833$ at $x=1.25705$



$Ma=300$

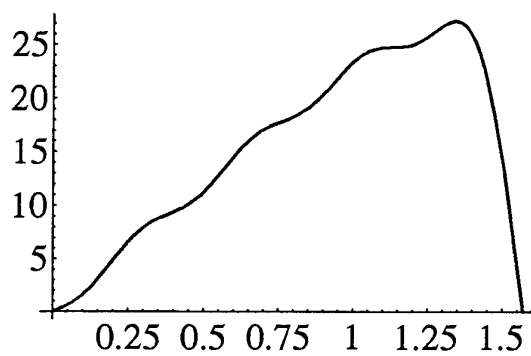
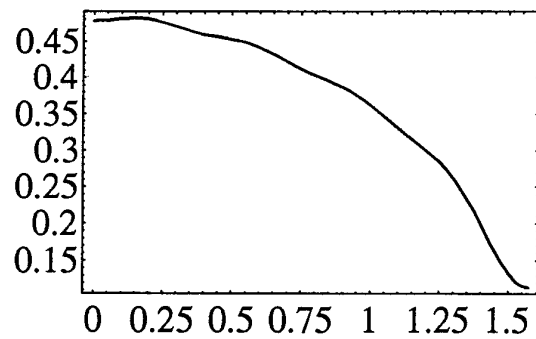
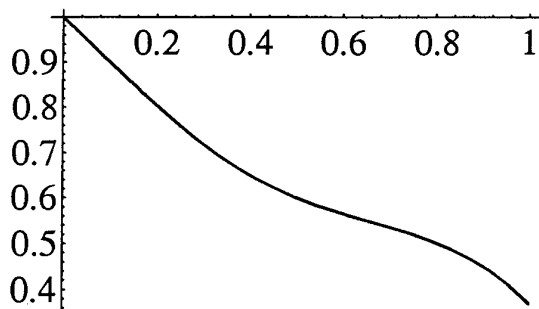
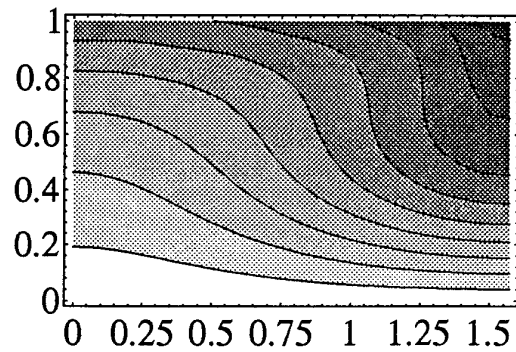
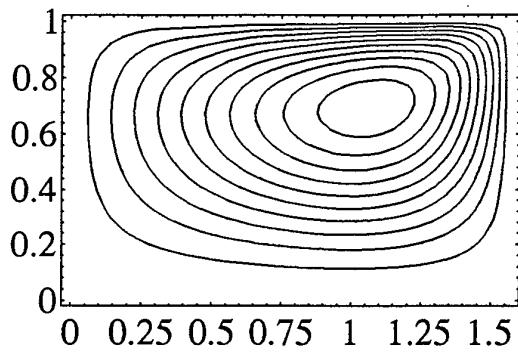
$k_0=2$

$N_{max}=8 \quad I_{max}=8$

$\delta=0.295515$

$\delta T=0.371919$

$V_{max}=21.9183$ at $x=1.31551$



Ma=400

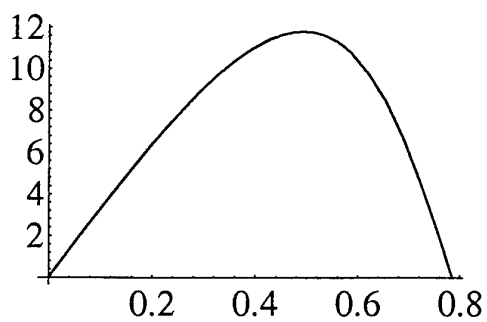
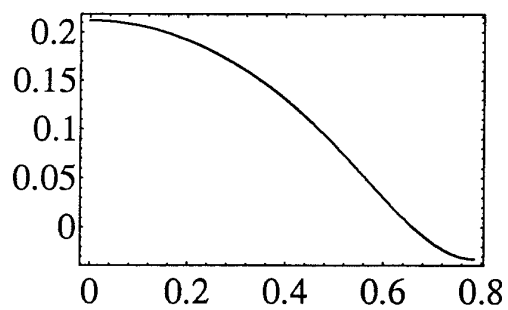
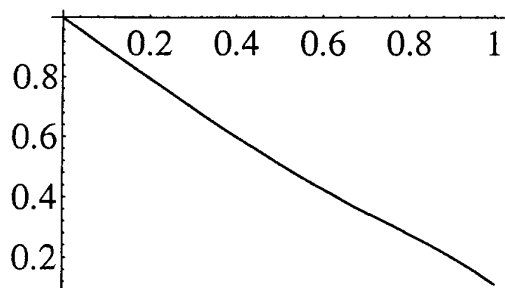
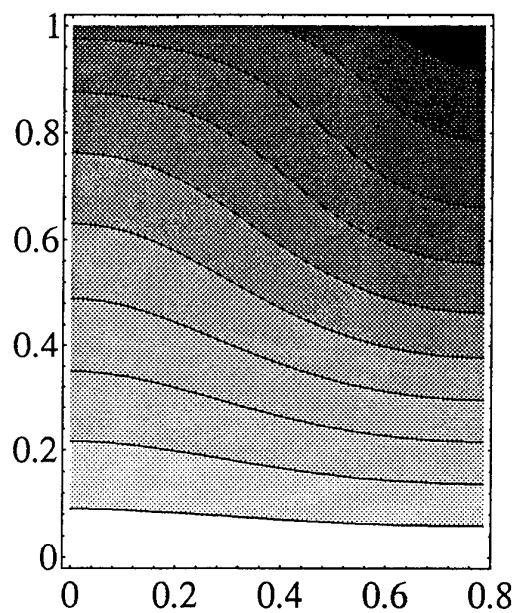
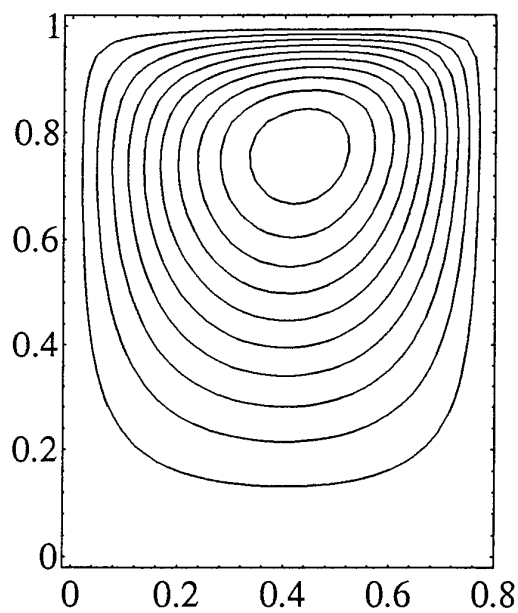
k0=2

Nmax=8 Imax=8

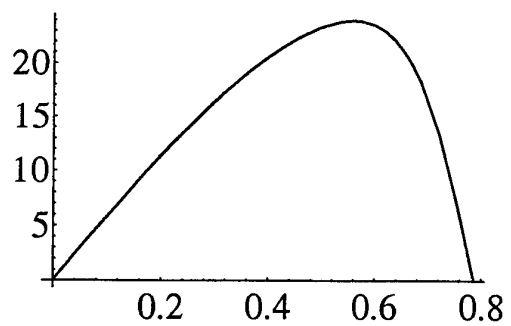
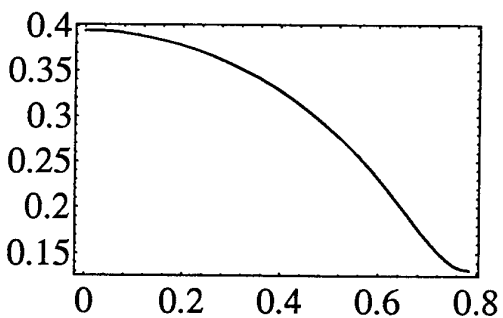
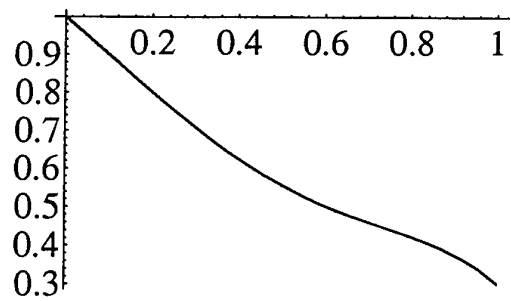
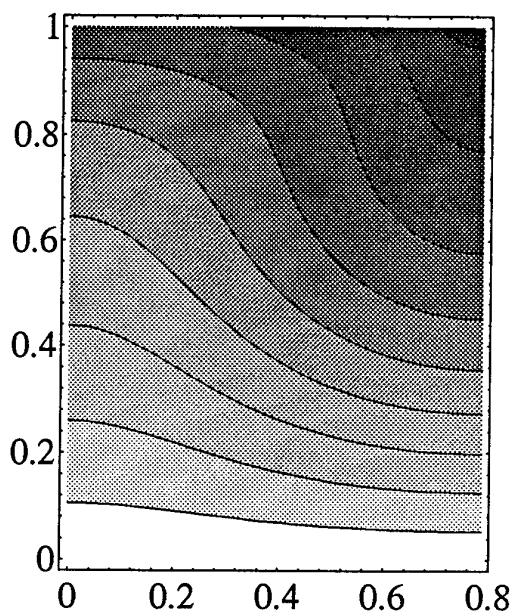
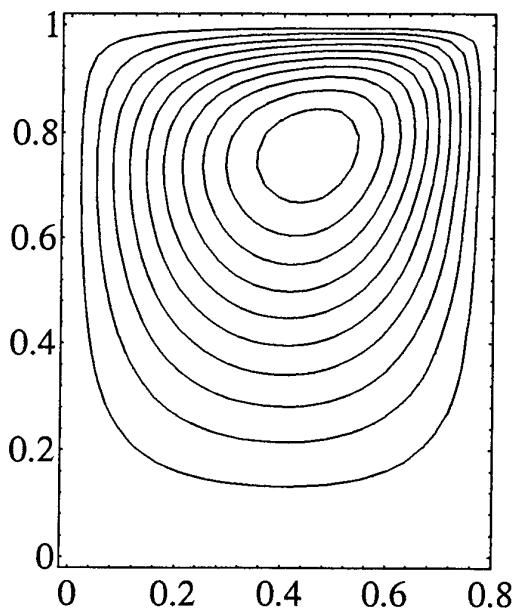
delta=0.371874

delta T=0.363511

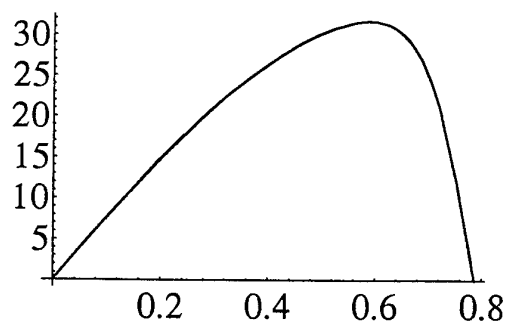
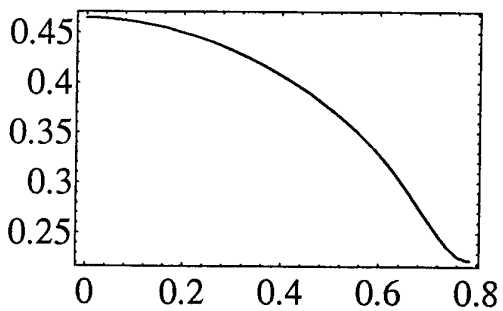
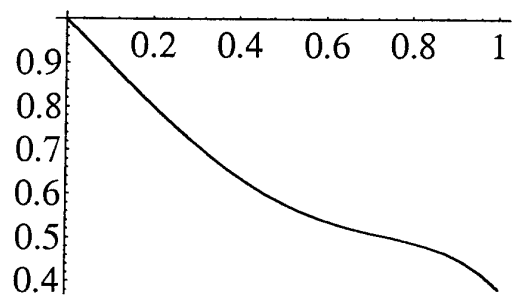
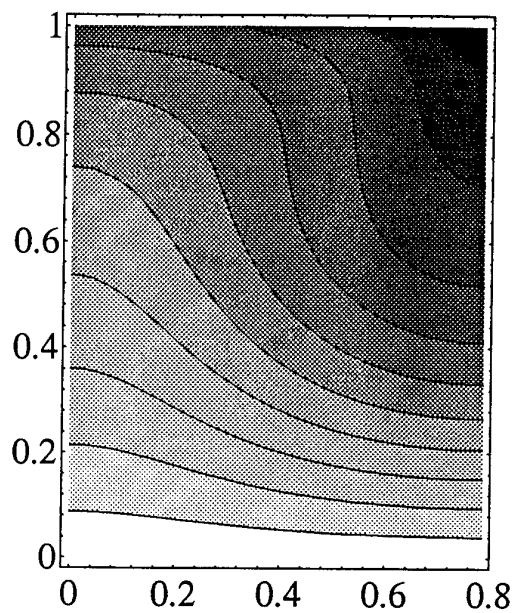
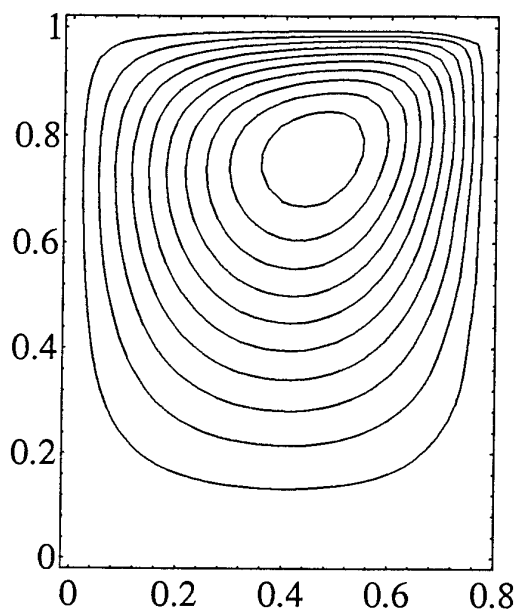
Vmax=27.1333 at x=1.34182



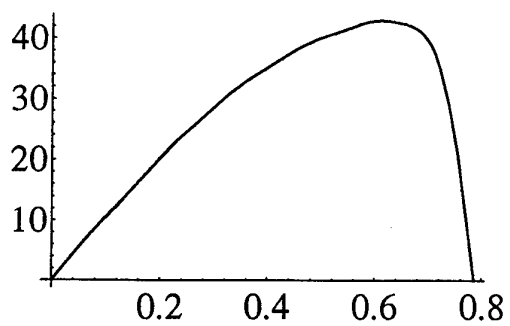
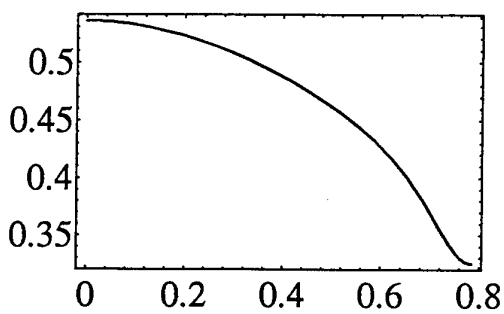
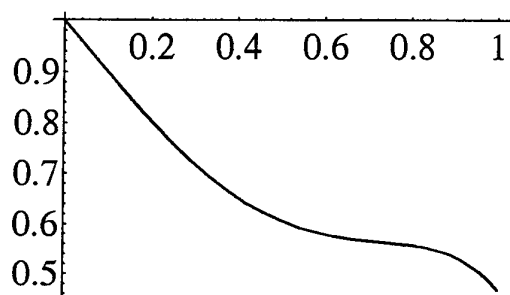
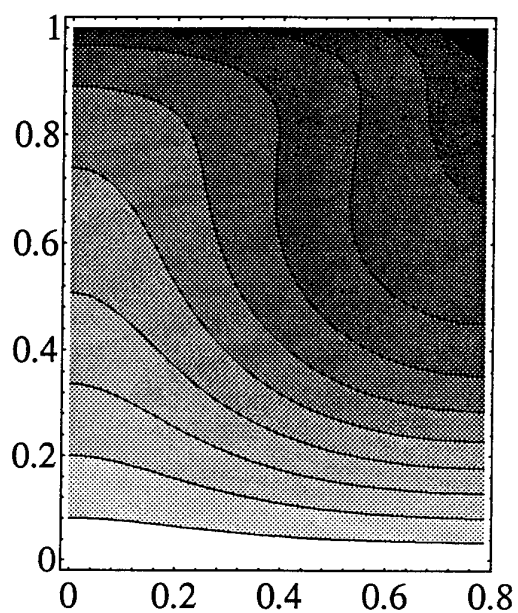
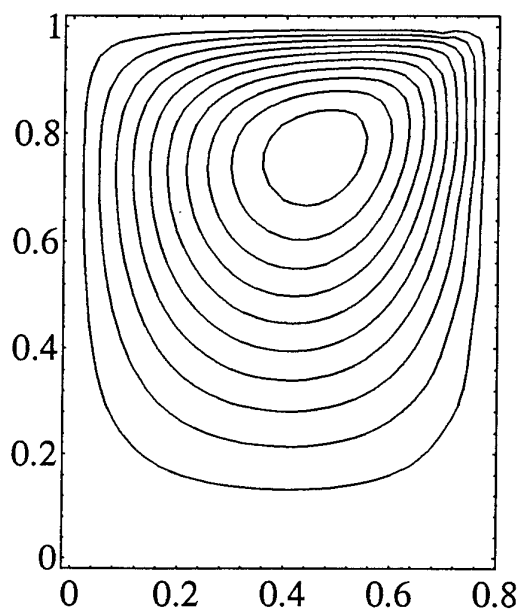
$Ma=200$
 $k0=4$
 $Nmax=8 \quad I_{max}=12$
 $\delta t=0.11291$
 $\delta T=0.244512$
 $V_{max}=11.7877 \text{ at } x=0.492159$



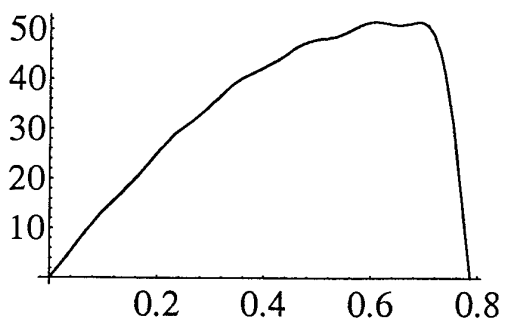
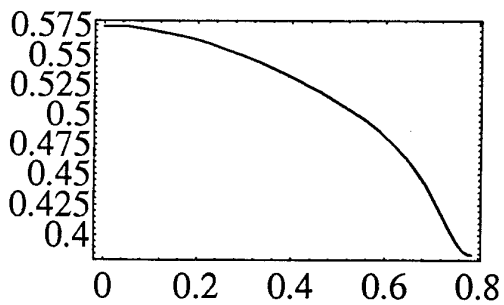
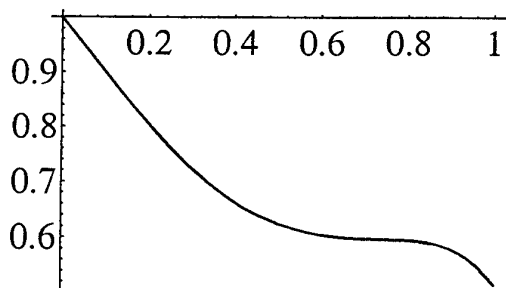
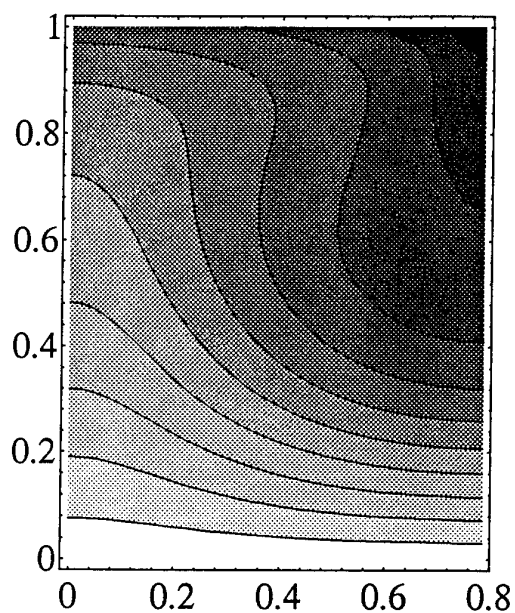
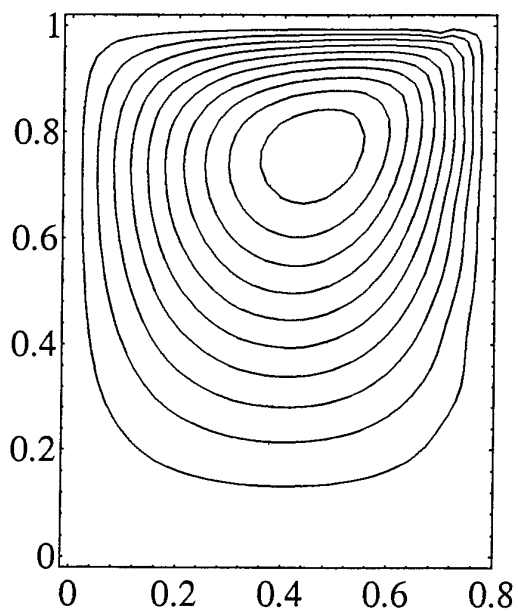
$Ma=400$
 $k0=4$
 $Nmax=8$ $I_{max}=12$
 $\delta=0.30269$
 $\delta T=0.262575$
 $V_{max}=23.9505$ at $x=0.558334$



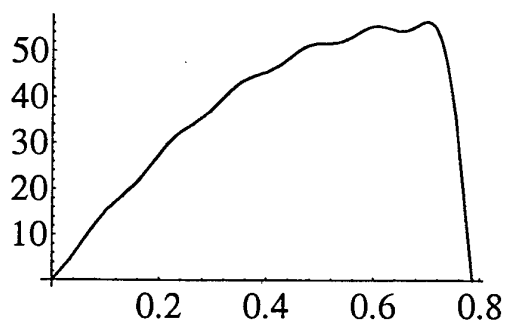
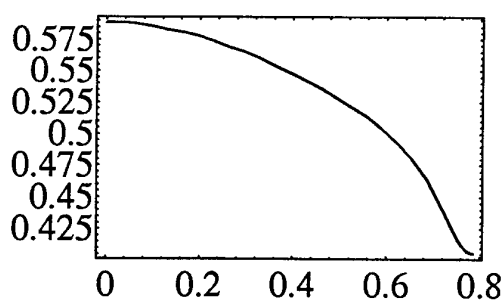
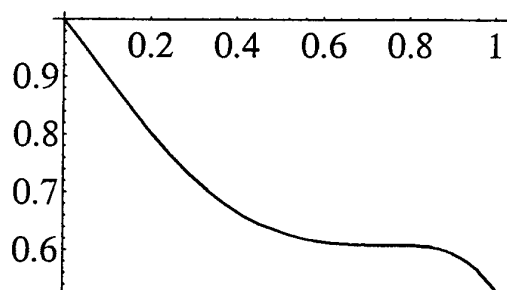
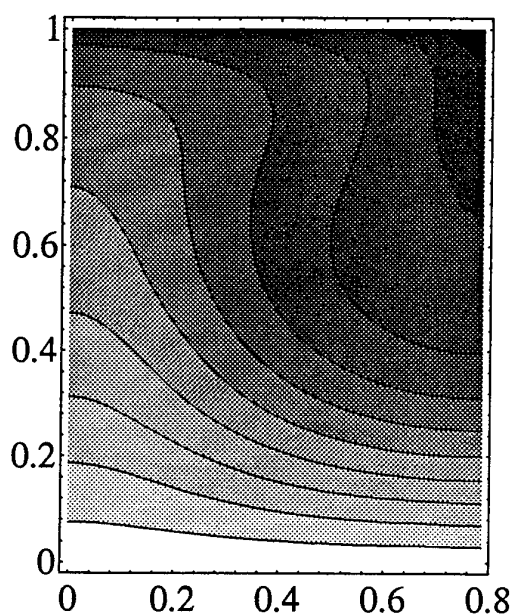
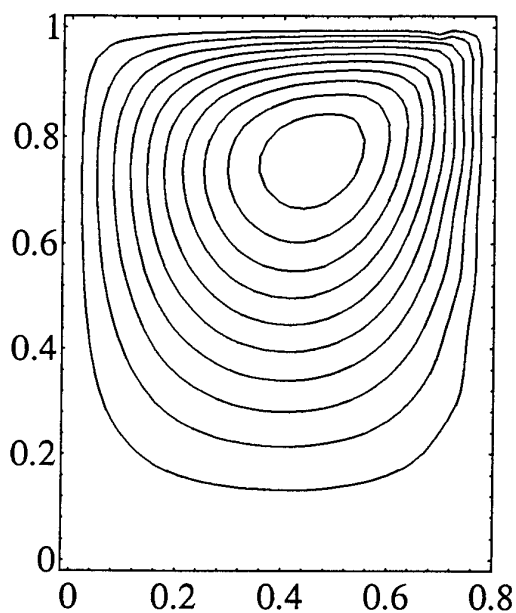
$Ma=600$
 $k0=4$
 $Nmax=8$ $I_{max}=12$
 $\delta t=0.384733$
 $\delta T=0.241677$
 $V_{max}=31.6616$ at $x=0.586935$



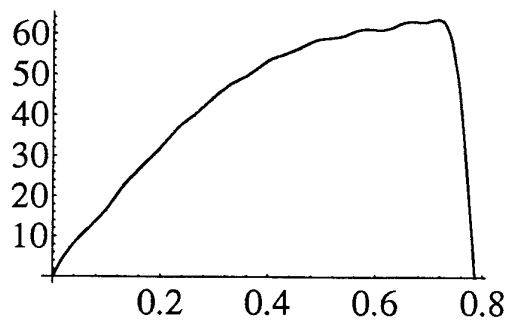
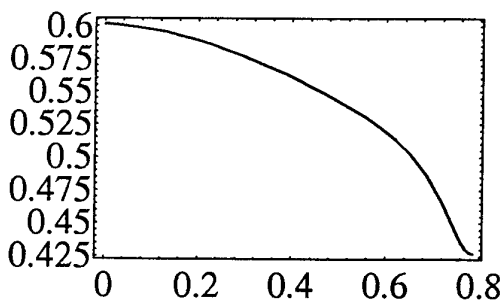
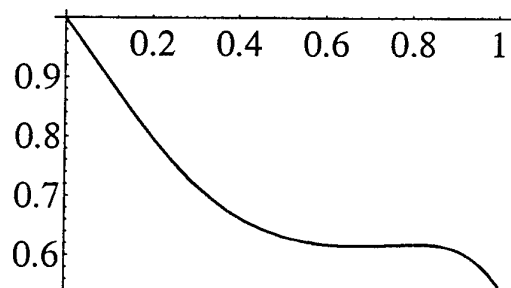
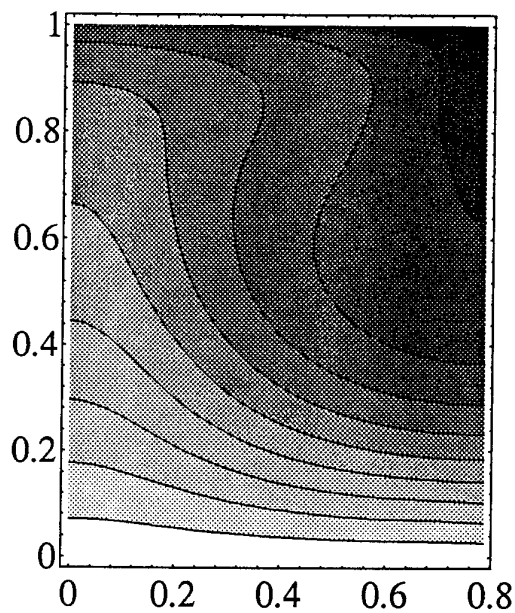
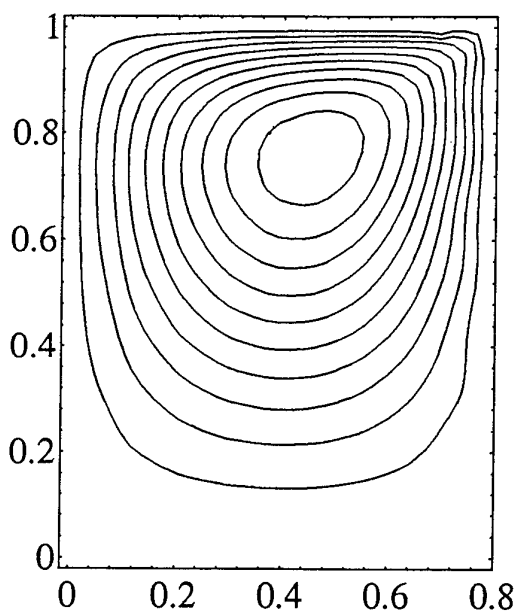
$Ma=1000$
 $k0=4$
 $Nmax=8$ $I_{max}=12$
 $\delta=0.469709$
 $\delta T=0.21006$
 $V_{max}=42.9016$ at $x=0.60969$



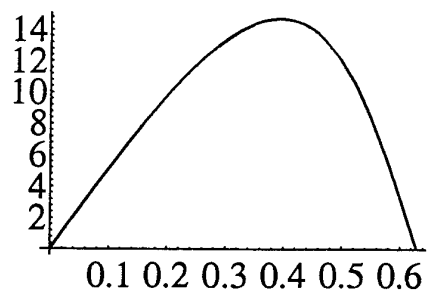
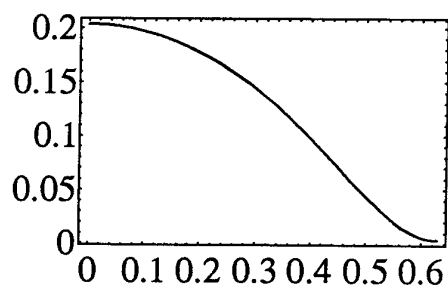
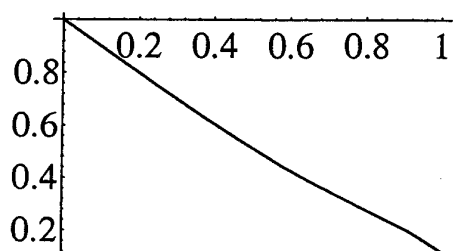
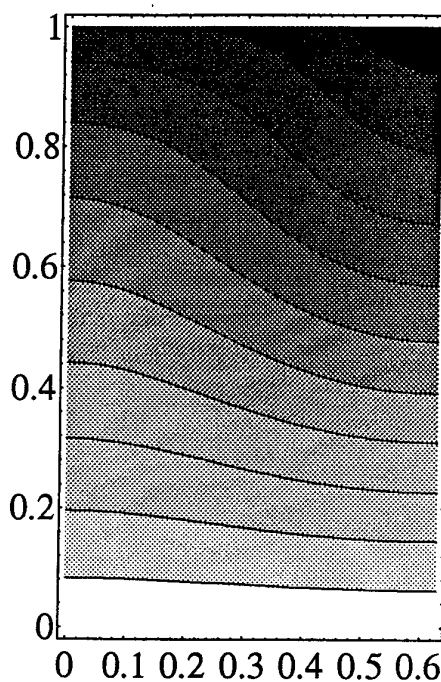
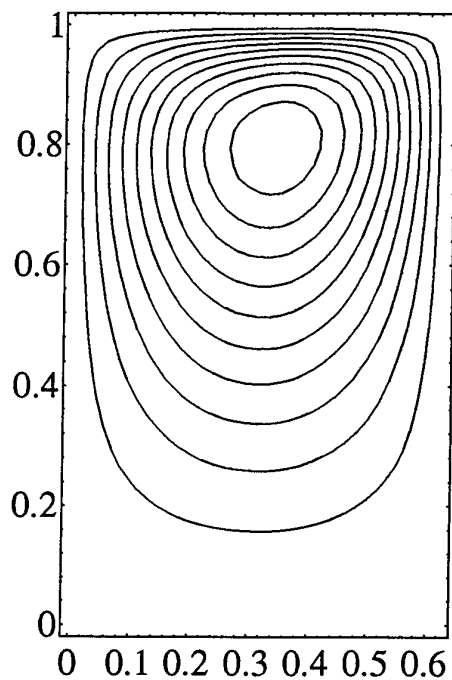
$Ma=1400$
 $k0=4$
 $Nmax=8$ $I_{max}=12$
 $\delta t=0.516742$
 $\delta T=0.190055$
 $V_{max}=51.4809$ at $x=0.688224$



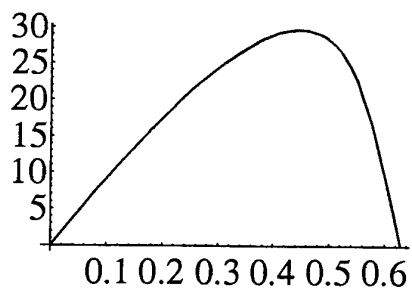
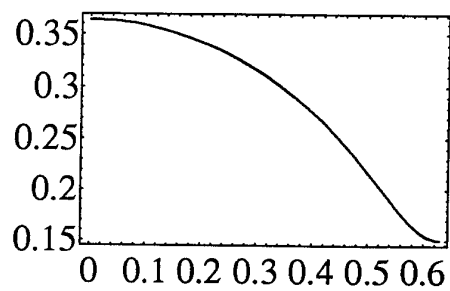
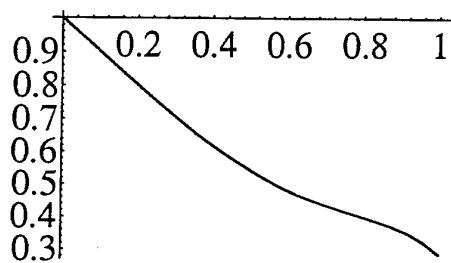
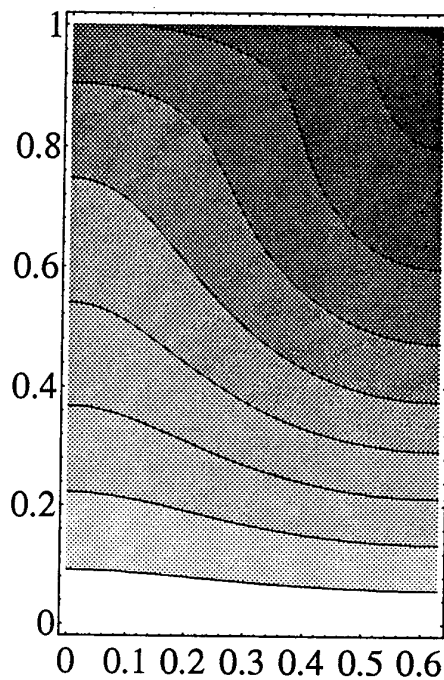
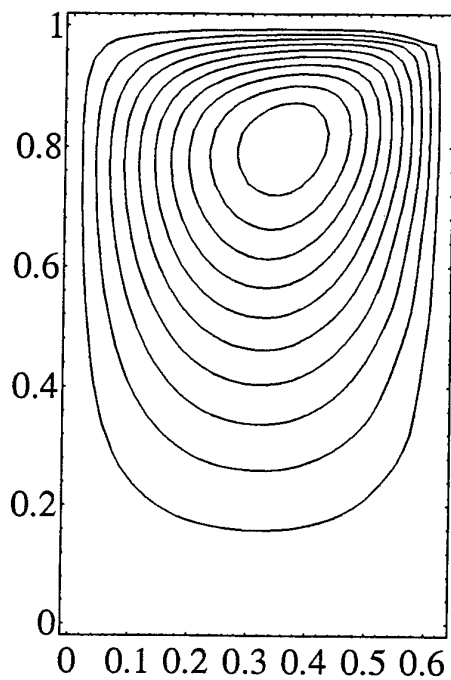
$Ma=1600$
 $k0=4$
 $Nmax=8$ $I_{max}=12$
 $\delta=0.533837$
 $\delta T=0.182567$
 $V_{max}=56.3796$ at $x=0.699488$



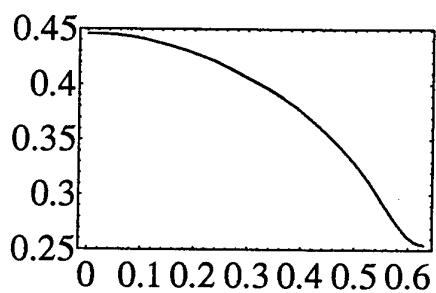
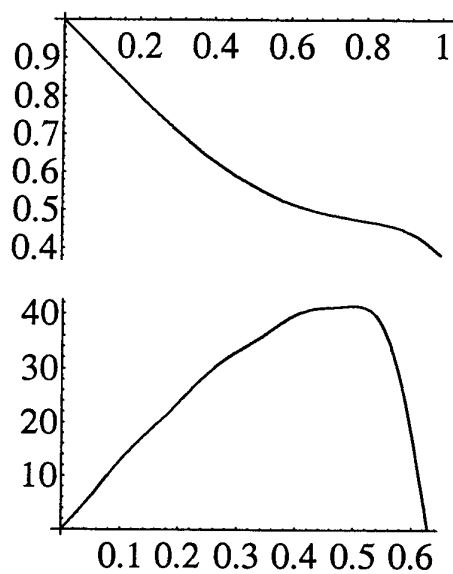
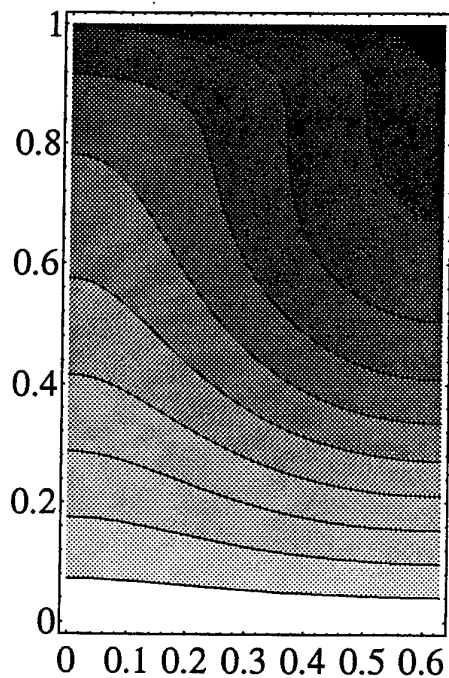
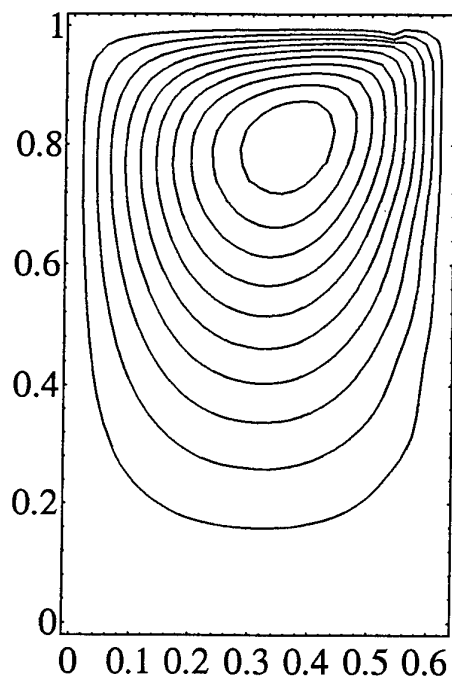
$Ma=2000$
 $k_0=4$
 $N_{max}=8 \quad I_{max}=18$
 $\delta t=0.549353$
 $\delta T=0.174188$
 $V_{max}=63.6036 \text{ at } x=0.715171$



$Ma=300$
 $k0=5$
 $Nmax=8$ $I_{max}=8$
 $\delta=0.122114$
 $\delta T=0.200213$
 $V_{max}=14.7025$ at $x=0.392792$



$Ma=600$
 $k0=5$
 $Nmax=8$ $I_{max}=8$
 $\delta=0.289018$
 $\delta T=0.213556$
 $V_{max}=29.6275$ at $x=0.44446$



$Ma=1000$

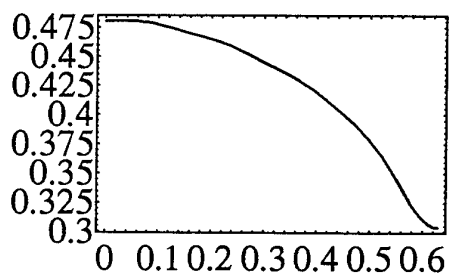
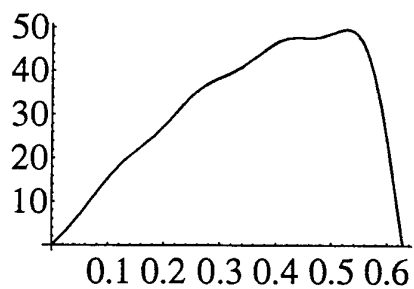
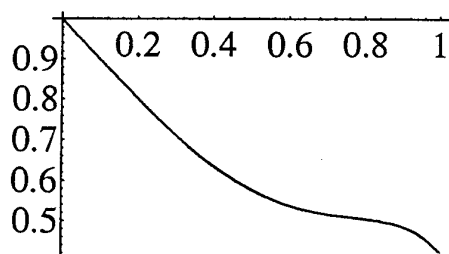
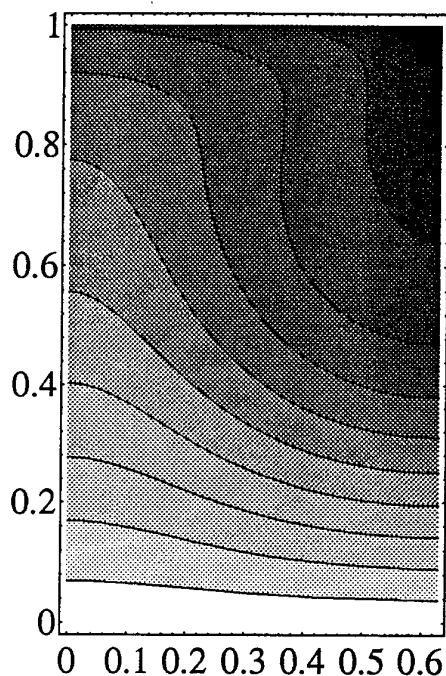
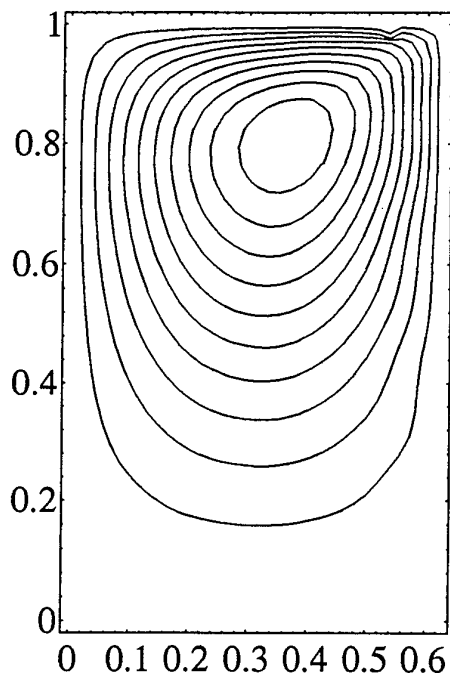
$k_0=5$

$N_{max}=8 \quad I_{max}=8$

$\delta=0.383426$

$\delta T=0.190609$

$V_{max}=41.508$ at $x=0.498396$



Ma=1300

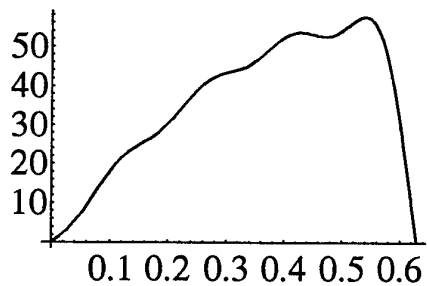
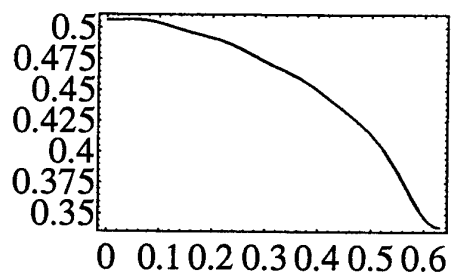
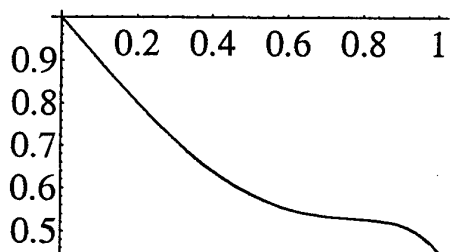
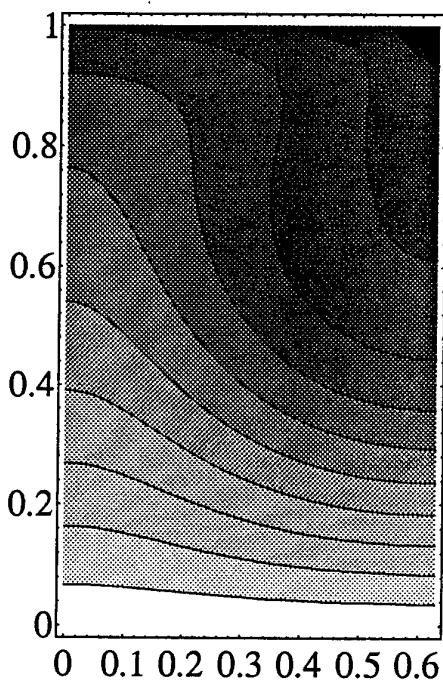
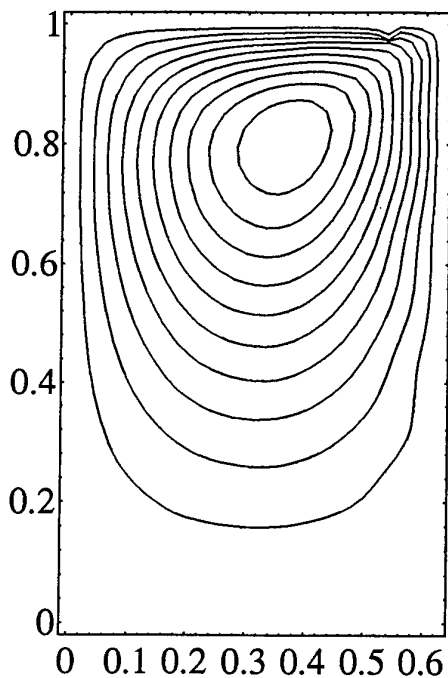
k0=5

Nmax=8 Imax=8

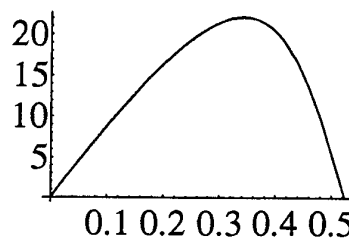
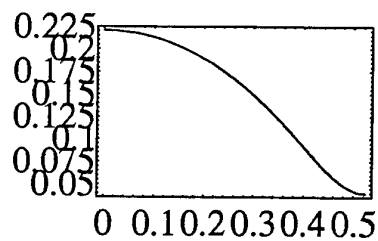
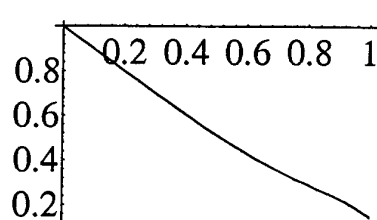
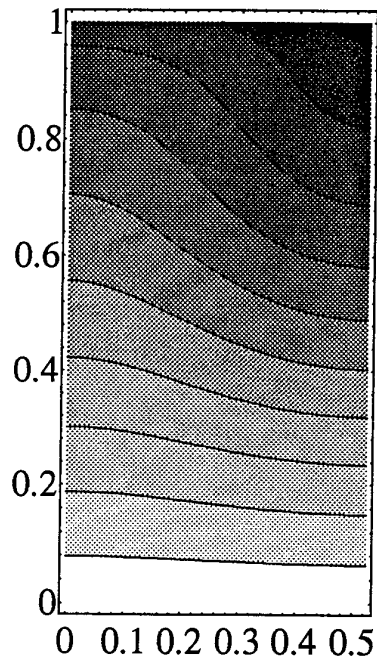
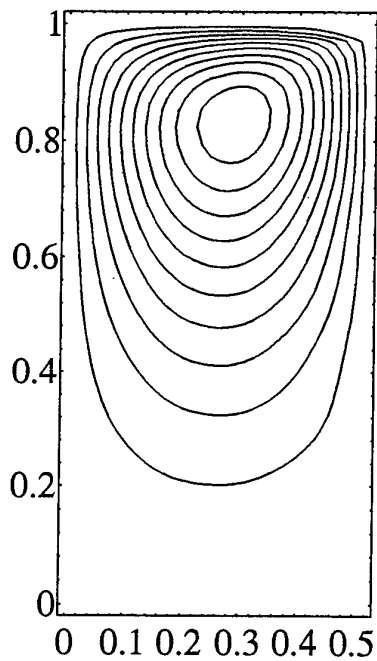
delta=0.425158

delta T=0.176928

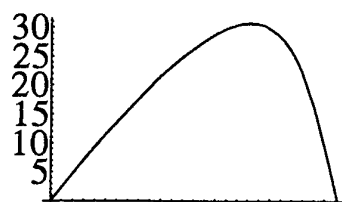
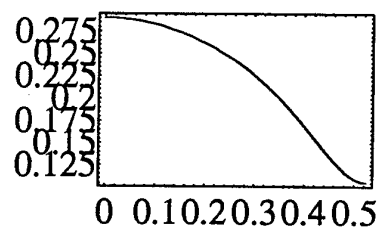
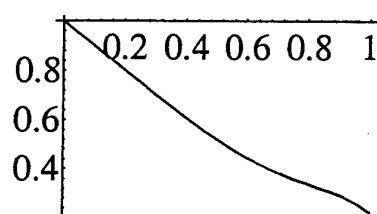
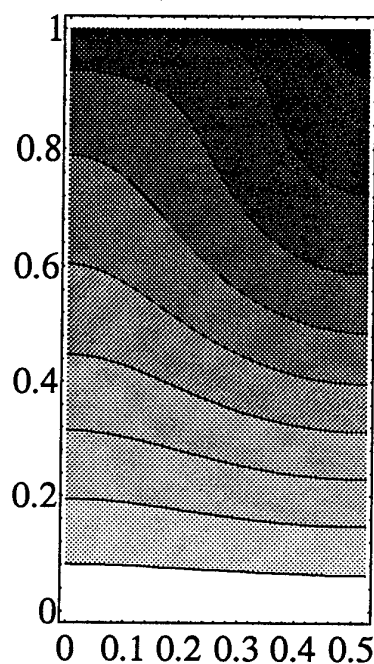
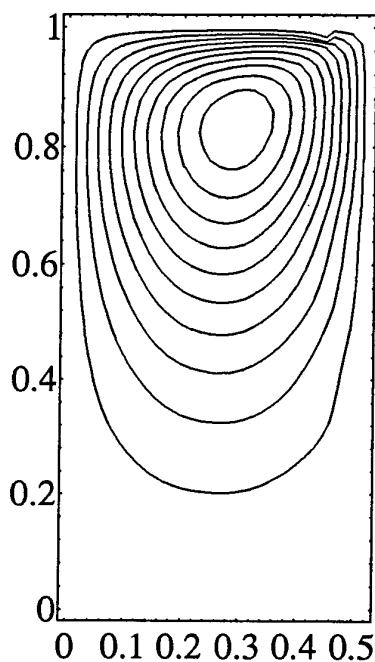
Vmax=49.4889 at x=0.526121



$Ma=1600$
 $k0=5$
 $Nmax=8$ $I_{max}=8$
 $\delta=0.455473$
 $\delta T=0.165987$
 $V_{max}=57.4826$ at $x=0.538621$



$Ma=500$
 $k0=6$
 $Nmax=8$ $I_{max}=8$
 $\delta=0.14992$
 $\delta T=0.18086$
 $V_{max}=22.0411$ at $x=0.3410$



$V_{\max}=30.659$ at $x=0.36314$

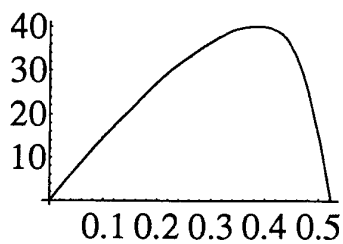
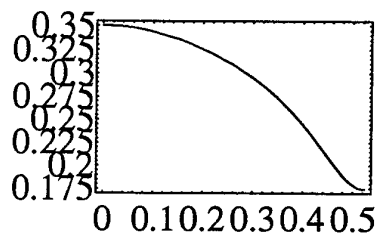
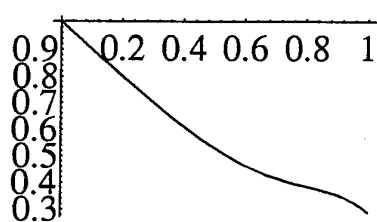
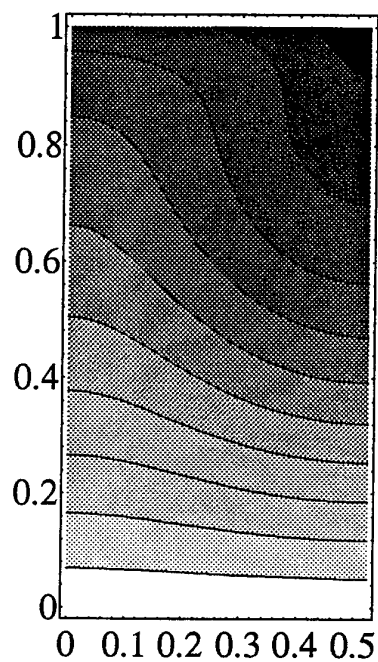
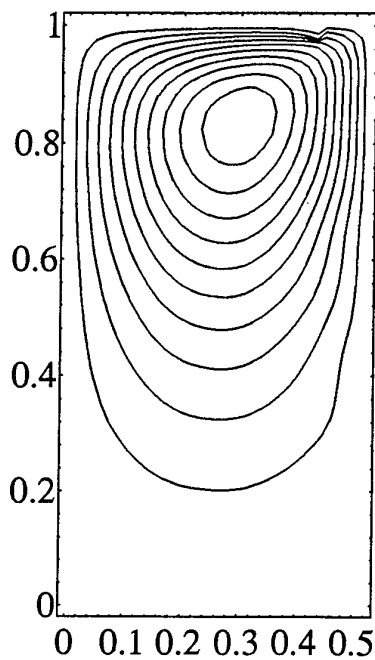
$Ma=700$

$k_0=6$

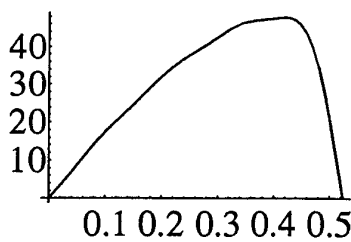
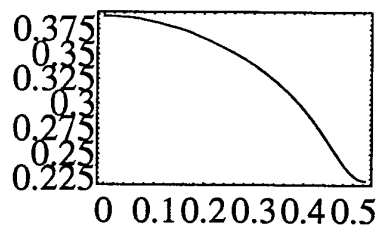
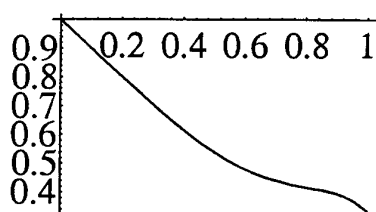
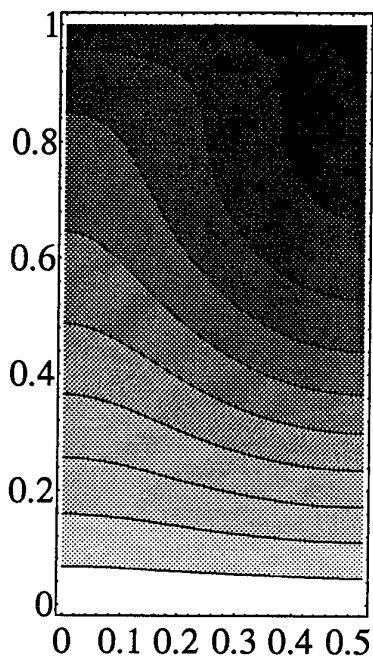
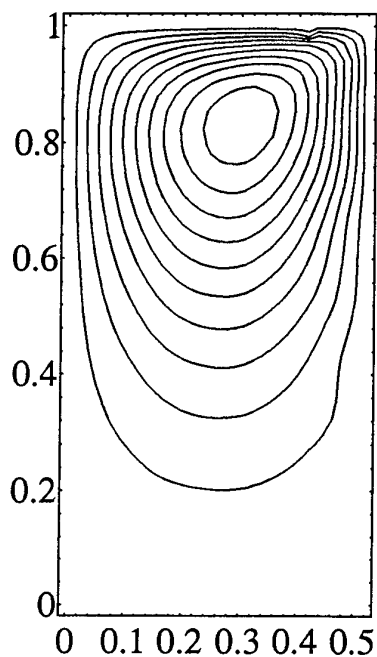
$N_{\max}=8$ $I_{\max}=8$

$\delta=0.222856$

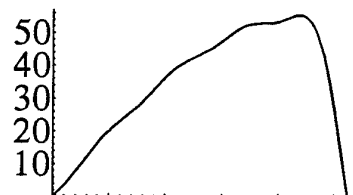
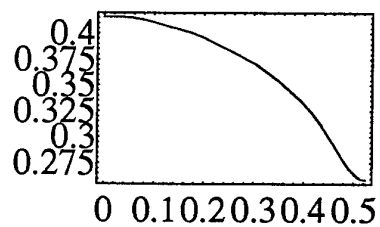
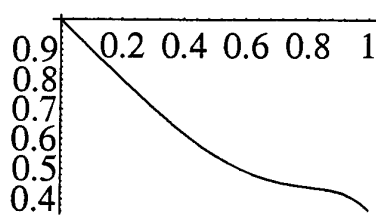
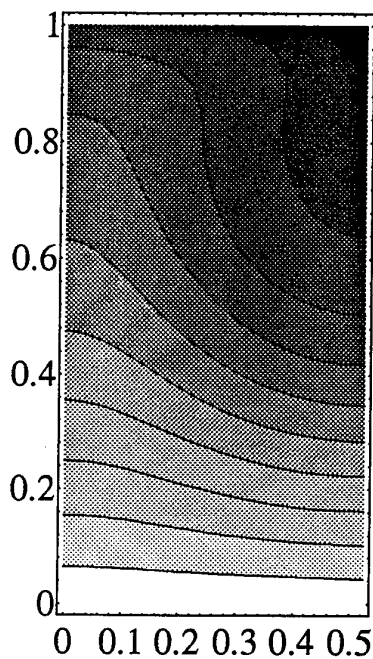
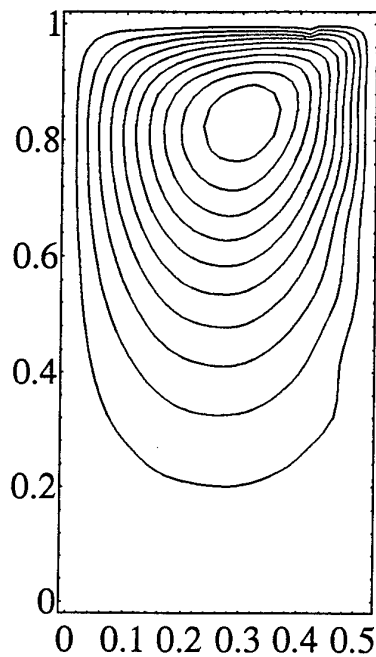
$\delta T=0.184623$



$Ma=1000$
 $k_0=6$
 $N_{max}=8 \quad I_{max}=8$
 $\delta=0.289832$
 $\delta T=0.175484$
 $V_{max}=40.105 \text{ at } x=0.3854$

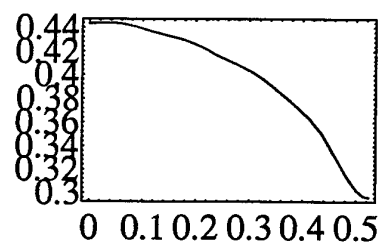
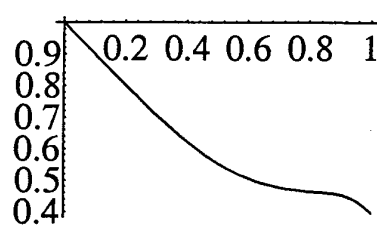
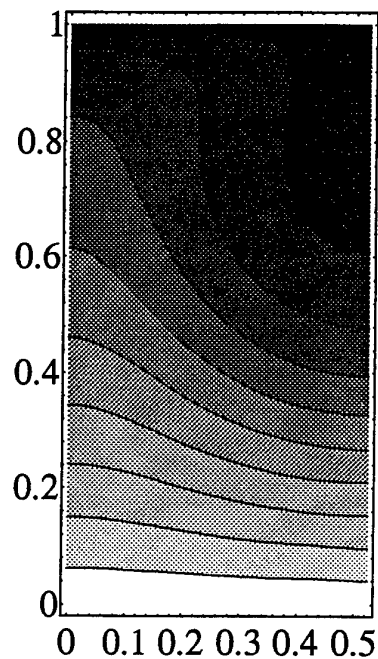
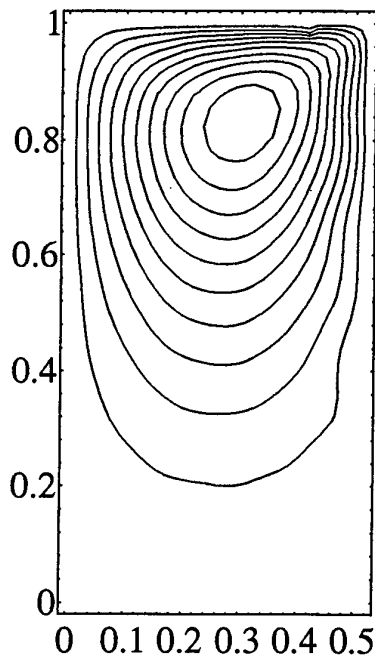


$Ma=1300$
 $k0=6$
 $Nmax=8$ $I_{max}=8$
 $\delta=0.33378$
 $\delta T=0.165461$
 $V_{max}=47.786$ at $x=0.4189$



$V_{\max}=55.4238$ at $x=0.4376$

$Ma=1600$
 $k_0=6$
 $N_{\max}=8$ $I_{\max}=8$
 $\delta=0.365941$
 $\delta T=0.1568$



Ma=2000

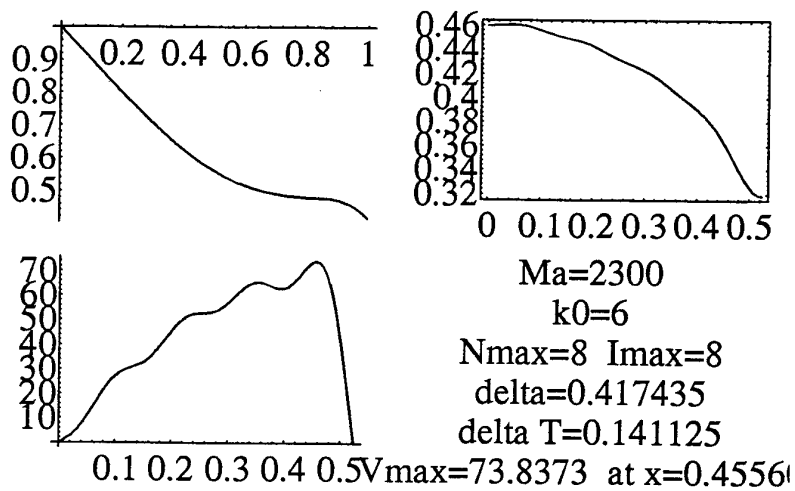
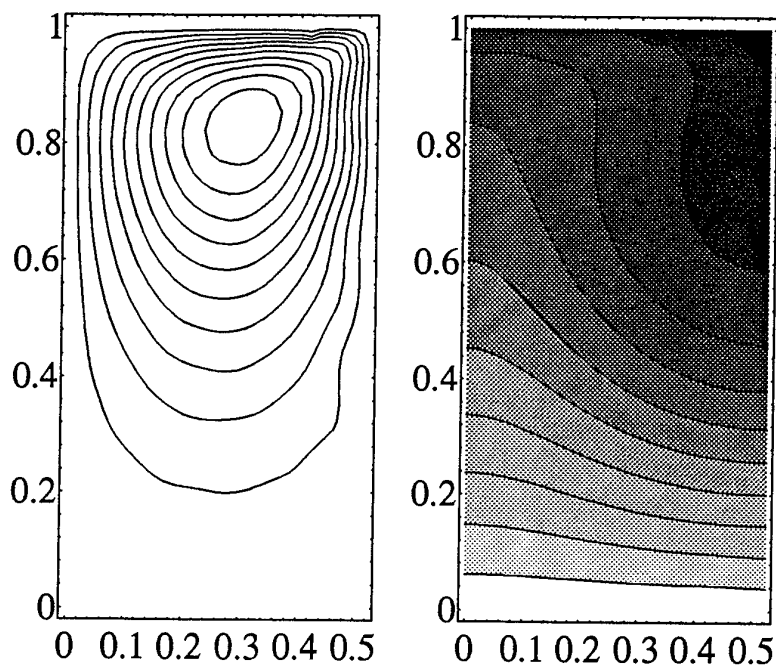
k0=6

Nmax=8 Imax=8

delta=0.398273

delta T=0.147229

0.1 0.2 0.3 0.4 0.5 Vmax=65.8661 at x=0.4499



IV.3. Comparison of numerical with analytical results

In order to compare results of sections III and IV, we first have to remark that the length scales used to put the problem under dimensionless form are different. In section III, we chose an arbitrary length d to scale the problem, while in section IV, the depth h of the layer was chosen for this purpose. As the analytical results of section III were obtained for a value $k=1$ of the dimensionless wavenumber (which means the dimensional value of this wavenumber is $k^*=1/d$), the corresponding value of the dimensionless wavenumber in section IV is $k^*.h=h/d=k_0$ (value given for each numerical simulation).

The velocities were scaled by κ/h in section IV, and by κ/d in section III. The dimensional value V^* of the velocity being independent of the choice of units, we must have $V^*=V^d.\kappa/d=V^h.\kappa/h$ (where V^d and V^h stand for dimensionless values of the velocity obtained respectively in section III and IV). Thus, the transformation rule between dimensionless velocities is $V^d=V^h/k_0$. Similarly, as the Marangoni number Ma is proportional to the square of the unit of length, we have the equivalence $Ma^d=Ma^h/k_0^2$. Finally, the unit of temperature being βd (section III) or βh (section IV), the temperature equivalence is $T^d=T^h.k_0$.

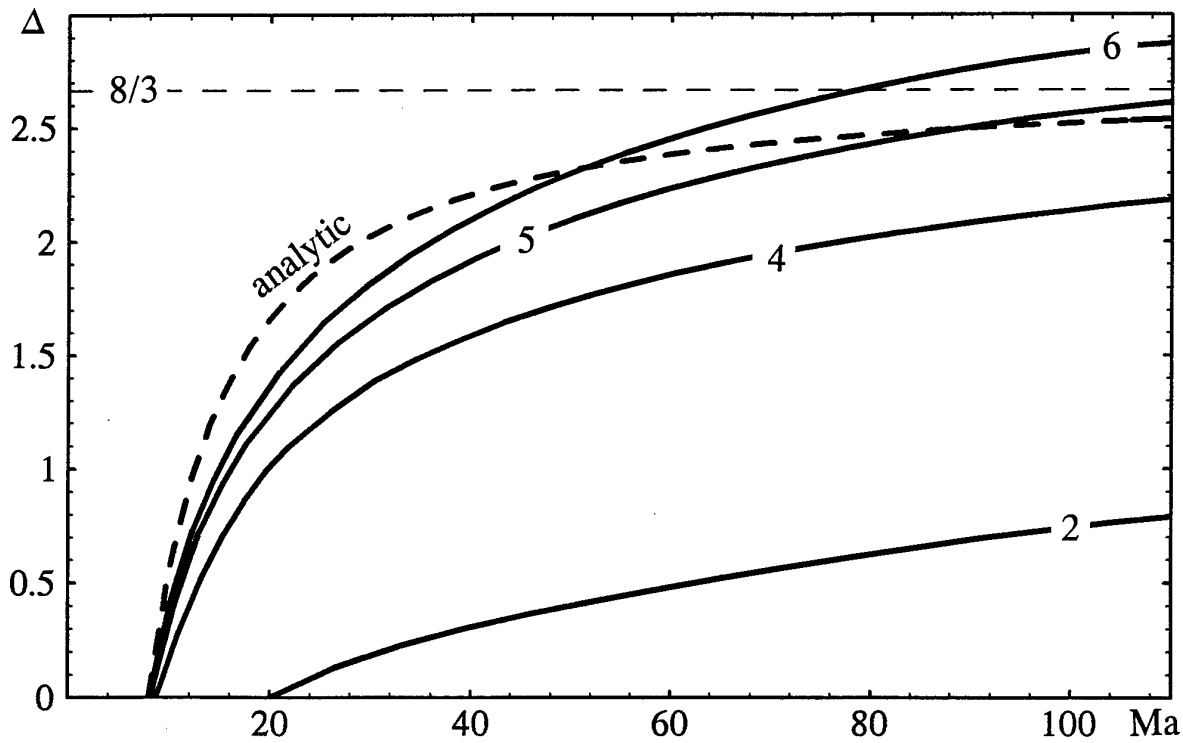


Figure 4.2 : The increase of the mean surface temperature due to convection (in units of $\beta d = \beta/k^*$), i.e. the bulk temperature decrease as a function of the Marangoni number. Plain curves : numerical results (the value of k_0 is indicated on each curve). Thick dashed curve: eq. 3.28, thin dashed curve : the limit of eq. 3.28 for $Ma \rightarrow \infty$, i.e. $8/3 \approx 2.66$. A good agreement is obtained for $k_0 \rightarrow \infty$, as in this limit, the convection cells are localised near the interface (see previous figures), and the layer can effectively be assumed infinitely deep.

Figure 4.2 presents the values of the increase of the mean surface temperature due to convection, expressed in units of section III (thus, values obtained in section III are unchanged, while numerical results of section IV have to be multiplied by k_0 : this gives $\Delta T \cdot k_0$), as a function of the Marangoni number $Ma = -\sigma_T \beta d^2 / \mu \kappa = -\sigma_T \beta / \mu \kappa k^*{}^2$. The thick full curves correspond to numerical results of section IV, corresponding to the values 2, 4, 5, and 6 of the wavenumber. The thick dashed line corresponds to the analytical formula (3.28) of section III for the bulk temperature decrease (which is equivalent to the free surface temperature increase), and the thin dashed horizontal line to the limit of this expression for $Ma \rightarrow \infty$, i.e. $8/3 \approx 2.66$ (as given by eq. 3.40). It is seen that all the numerical curves seem to present a saturation of the surface temperature increase when $Ma \rightarrow \infty$, although calculations would be necessary at higher Marangoni numbers, but would require a much larger computational effort. Furthermore, the numerical curves approach the analytical ones when k_0 is increased, as expected from the discussion at the beginning of section IV.2. In fact, the analytical results obtained in section III appear to be quite reliable for computing this convective quantity in the limit $k_0 \rightarrow \infty$, which is a very satisfactory result taking into account the drastic assumptions underlying their derivation (mean-field approximation, limitation of amplitude equations to cubic terms and negligence of harmonics of the fundamental wavenumber).

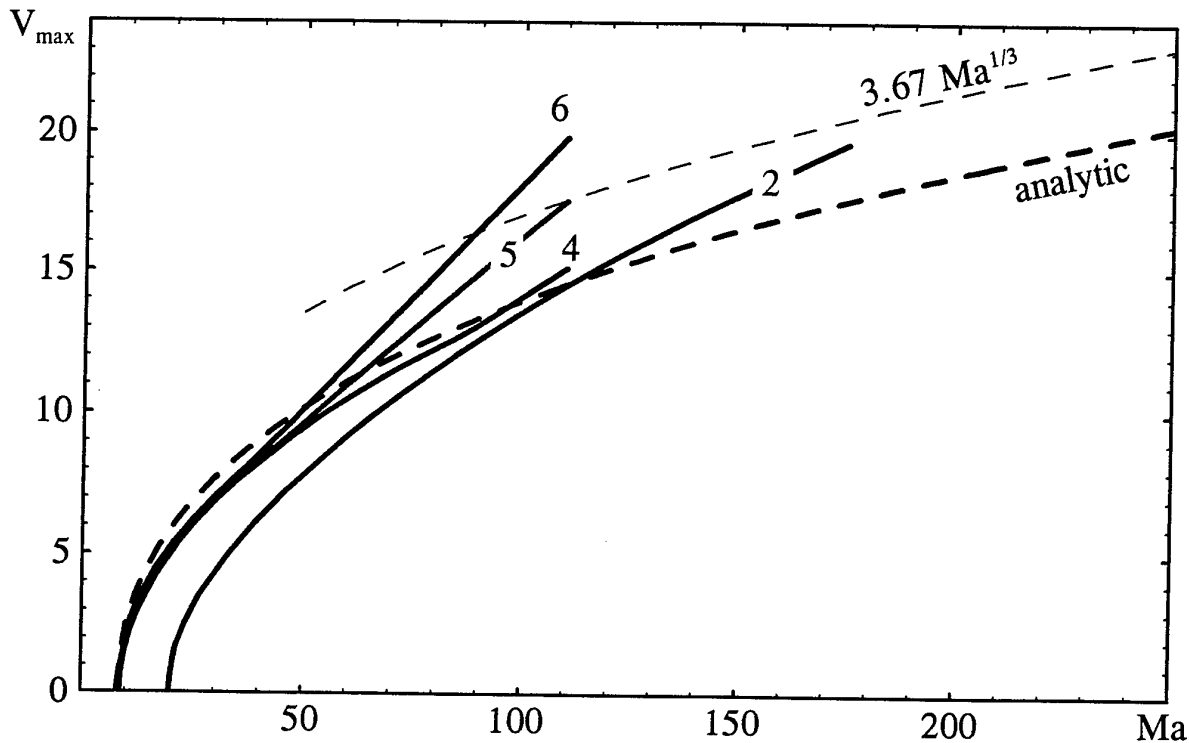


Figure 4.3 : The maximal surface velocity (in units $\kappa/d = \kappa k^*$) as a function of the Marangoni number $Ma = -\sigma_T \beta / \mu \kappa k^*{}^2$. Plain curves : numerical results (the value of k_0 is indicated on each curve). Thick dashed curve : analytical (using 3.27), thin dashed curve : asymptotic behaviour for $Ma \rightarrow \infty$, i.e. $3.67 Ma^{1/3}$ (eq. 3.41). Again, a good agreement is obtained for $k_0 \rightarrow \infty$, apart from numerical inaccuracies causing a divergence of the curves above $Ma = 40$.

The behaviour of other convective quantities with Ma is represented on figs 4.3 (maximal surface velocity) and 4.4 (amplitude of surface temperature variations). It is seen that the agreement is also quite satisfactory, already for values of $k_0=4$ and 5.

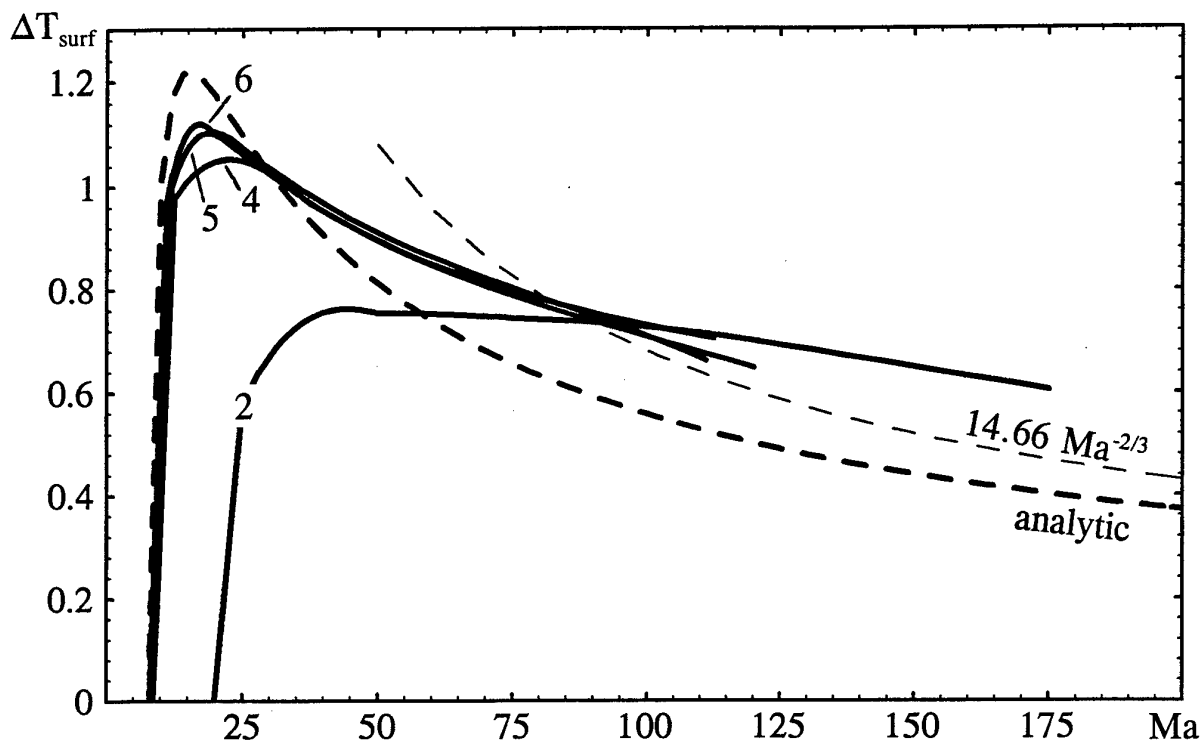


Figure 4.4 : The amplitude of the surface temperature variations (in units $\beta d = \beta/k^*$) as a function of the Marangoni number $Ma = -\sigma_T \beta / \mu k k^{*2}$. Plain curves : numerical results (the value of k_0 is indicated on each curve). Thick dashed curve : analytical result (using eq. 3.27), thin dashed curve : asymptotic behaviour for $Ma \rightarrow \infty$, i.e. $14.66 Ma^{-2/3}$ (eq. 3.42). Again, a good agreement is obtained for $k_0 \rightarrow \infty$, already for values of $k_0=4$ and 5.

IV.4. Conclusions of section IV

In this section, a full numerical integration of the equations governing Marangoni-Bénard convection in finite idealised boxes has been presented. Although the Galerkin formulation includes the effect of buoyancy, the value of the Rayleigh number has been considered as zero (microgravity, or layers with small depth). In this first analysis of the problem, the free surface Biot number has been set to zero. Extension to non-zero Biot number (e.g. due to evaporation) could be achieved in the future.

The lateral walls of the layer have been assumed slippery (which means that the velocity tangential to the wall is not zero, as would be the case for real rigid walls), and insulating. This kind of walls, which have often been used in previous studies of the effect of lateral walls on nonlinear convection, are known to simplify the mathematical analysis of the problem. In particular, they are equivalent to periodic boundary conditions, thus allowing straightforward comparison with analytical results of section III.

Numerical simulations have been presented for values of the wavenumber k_0 equal to 2, 4, 5, and 6 (corresponding respectively to values $L=1.57$, 0.785, 0.628 and 0.524 of the aspect ratio $L=l/h$ of the box, where l and h are respectively the dimensional width and height of the box). For each value of k_0 , the Marangoni number is increased step by step. For each step, the following results are presented for the steady convective state reached after transient have been damped out : the streamline pattern, the isotherms, the mean temperature profile, the free surface temperature, and the free surface horizontal velocity. Numerical values of typical convective quantities are also presented : these are the increase of the mean surface temperature due to convection (which is equivalent to the bulk temperature decrease Δ of section III, and measures the enhancement of heat transfer due to convection), the amplitude of the surface temperature variations, the value of the maximal surface velocity, together with the horizontal position of this maximum.

The results show that the enhancement of heat transfer due to Marangoni convection presents a saturation behaviour when the Marangoni number is increased. The free surface velocities grow continuously with Ma , and the amplitude of the surface temperature variations (difference between hot and cold spots on the free surface) first grows and then decreases when Ma is increased. For $k_0 \rightarrow \infty$, it is seen that numerical results compare very well with analytical results obtained via the amplitude equations analysis of section III, despite the drastic assumptions making its realisation possible. This is a proof of the validity of these approximations for studying Marangoni-Bénard convection far from the instability threshold.

IV.5. References of section IV

1. O. Dupont, P. Colinet, Ph. G  oris and J.C. Legros, *Microgravity Q.* **2**, 4, pp. 233-238 (1992).
2. S. Rosenblat, G.M. Homsy and S.H. Davis, *J. Fluid Mech.* **120**, 91 (1982); **120**, 123 (1983).

V. GENERAL CONCLUSIONS

In the first part of this work, we first computed the rate of evaporation of a liquid layer lying on a heated rigid plate at constant temperature T_b , the free surface of which being in contact with a gas phase at constant pressure p_g . Evaporation is modelled taking into account deviations from equilibrium (existence of a chemical potential difference on both sides of the free surface, revealing a deviation of the state of the interface from the Clausius-Clapeyron coexistence curve), which may occur for example in the presence of small quantities of impurities, imperfect gases, ... resulting in low values of the accommodation coefficient appearing in the Hertz-Knudsen law (equivalently, low values of the phenomenological coefficient K appearing in our formulation of the problem). This first analysis resulted in the determination of a particular solution (the basic state) of the full system of conservation equations (mass, momentum and energy) describing the problem. A graphical determination of the evaporative mass flux J was proposed, together with an analytical formula, valid provided the energy flux (proportional to the mass flux) is not too large (of the order of some Watts/cm² for a 1mm depth of water).

In a second stage, we determined the conditions under which such a basic state is stable against hydrodynamic fluctuations, allowing the surface tension of the liquid to depend on temperature. Indeed, evaporation at the free surface creates a temperature gradient inside the liquid layer near the interface, such that this situation can become unstable above a certain value of this gradient. In the limit of small liquid Peclet numbers (relatively small evaporative mass fluxes), the temperature profile is linear in the liquid phase. If furthermore the Crispation number is small (and the Galileo number is large), the surface deformation can be neglected, and the stability problem is shown to reduce to the classical Pearson's problem. The critical value of the Marangoni number Ma (proportional to the value of the mass flux and to the surface tension variation with temperature) is determined as a function of the Biot number, characterising the effective heat transfer through the free surface, and function of the evaporation parameters. In particular, it can be computed that this number can be as large as 10^3 for typical liquids as water. However, this value can be reduced by one or two order of magnitudes by the presence of unavoidable impurities on the free surface, reducing the values of the accommodation coefficient (in the Hertz-Knudsen relation), and accentuating the deviation from the equilibrium limit. The critical Marangoni number is found to increase with the Biot number, thus revealing a stabilising influence of evaporation.

A nonlinear analysis of the convection problem was then undertaken in section III, in order to determine the enhancement of heat transfer created by convection, when the threshold of stability is exceeded. This analysis is based on the assumptions that the dynamics of convection can be described by the interactions of the unstable eigenmodes of the problem, that the layer can be assumed infinitely deep (this is not contradictory with the assumption of a small Peclet number, provided that attention is restricted to short wave effects, localised near the free surface), and that the Prandtl number of the liquid can be assumed infinite. It was found that thermocapillary convection results in a decrease of the bulk temperature (or equivalently in an increase of the free surface temperature), such that the injected thermal energy is transported under a smaller temperature difference, due to the additional heat transport created by convection. The value of this bulk temperature decrease was found to increase with the Marangoni number, and shown to present a saturation behaviour when the

Marangoni number tends to infinity. Analytical formulas were obtained, as a function of the Biot number. Other convective quantities have also been computed (the maximal surface velocity, behaving as $Ma^{1/3}$ for $Ma \rightarrow \infty$, and the amplitude of surface temperature variations, decreasing as $Ma^{-2/3}$ in the same limit). Results were also obtained concerning the nonlinear competition between unstable modes : in particular, the wavelength selection problem has been investigated on the basis of a numerical transient integration of the system of amplitude equations. It was shown that in a first stage, convection always develops from infinitesimal perturbations under the form of convective structures having horizontal wavelengths determined by the fastest growing perturbations (wavenumbers proportional to $Ma^{1/2}$ for large Ma). When these perturbations become sufficiently large, convective cells begin to coalesce, and to form larger and larger wavelength structures. This process becomes slower and slower, due to the increasing inertia of the fluid to set in motion, and finally stabilises when the size of convection cells becomes comparable to the size of the vessel containing the experiment. The bulk temperature decrease is found to increase continuously during this process, thus indicating the general tendency of natural convection to increase the heat transfer. Other results were obtained about the competition between roll and hexagonal structures. It was shown that the hexagonal structures are generally preferred for moderate Marangoni numbers, while rolls stabilise for very large Marangoni numbers. This confirms earlier results qualitatively, even if the method (and the quantitative results) are significantly different.

Finally, a full two-dimensional numerical simulation of the problem was performed, by the use of a Galerkin method. This allowed to incorporate the effect of a finite depth of liquid (lower rigid plate). Results were obtained for various aspect ratios of the convective cells by varying the aspect ratio of the simulation domain. In particular, a very satisfactory (quantitative) agreement has been obtained with analytical results obtained via the amplitude equations analysis, when the aspect ratio (width/depth) tends to zero, in which case the convective perturbations are effectively located near the interface, and do not perceive the presence of an horizontal rigid bottom plate. This rather good concordance is a proof of the legitimacy of the above-mentioned assumptions, which should thus be helpful for further studies of Marangoni-Bénard convection heat transfer characteristics.